Circulation and Deep Water Renewal in Douglas Channel, British Columbia, Canada

by

Di Wan
B.Sc., University of Calgary, 2007
M.Sc., University of Victoria, 2014

A Dissertation Submitted in Partial Fulfillment of the
Requirements for the Degree of

DOCTOR OF PHILOSOPHY

in the School of Earth and Ocean Sciences

Circulation and Deep Water Renewal in Douglas Channel, British Columbia, Canada

by

Di Wan
B.Sc., University of Calgary, 2007
M.Sc., University of Victoria, 2014

Supervisory Committee

Dr. Michael G. G. Foreman, Co-Supervisor
(School of Earth and Ocean Sciences)

Dr. Stan E. Dosso, Co-Supervisor
(School of Earth and Ocean Sciences)

Dr. Patrick F. Cummins, Departmental Member
(School of Earth and Ocean Sciences)

Dr. Charles G. Hannah, Outside Member
(Department of Mechanical Engineering)

Dr. Stephen F. Cross, Outside Member
(Department of Geography)

ABSTRACT

Douglas Channel is the main waterway in the fjord system on the west coast of British Columbia (BC), Canada, connecting the town of Kitimat to Queen Charlotte Sound and Hecate Strait. A 200 m depth sill divides Douglas Channel into an outer and an inner basin. This thesis examines the sub-tidal circulation and deep water renewals in Douglas Channel using mooring data collected between 2013 and 2015. It was found that the overall circulation in Douglas Channel has a three-layer structure in winter and a four-layer structure in summer when deep water renewal occurs. The circulation is a mixture of estuarine flow, wind-driven flow, and the barotropic and baroclinic responses to changes to the surface pressure gradients. The surface current velocity fluctuation is dominated by the along-channel wind-driven currents, whereas a counter-wind velocity response is detected at 100–120 m depth. Further investigation of the wind-driven circulation shows that the physically narrow Douglas Channel is dynamically wide and the cross-channel geostrophic balance determines the along-channel velocity layer thicknesses and directions as found in wide channels. This result can be generalized to other flows, such as the surface outflow in the estuarine circulation, and provides a possible explanation to the disagreement between the thicknesses of the surface velocity layer and the stratification layer. At depth, the renewal events are connected to the availability of dense water on the shelf. The examination of the dense water variation leads to evidence that a long-range connection exists between the BC shelf water density and remote influences, expanding the studies of the processes and frequencies that influence upwelling on the BC coast to the quasi-biweekly and intraseasonal bands and the equatorial Pacific and northern California and Oregon regions. These findings will be able to direct future studies in this region, as well as the entire BC shelf upwelling dynamics.

Table of Contents

Supervisory Committee **ii**

Abstract **iii**

Table of Contents **iv**

List of Tables **vii**

List of Figures **x**

Acknowledgments **xviii**

Chapter 1 Introduction **1**

1.1 Thesis structure 3

Chapter 2 Sub-tidal circulation in a deep-silled fjord: Douglas Channel, British Columbia **4**

2.1 Introduction 5

2.2 Data Description 7

2.2.1 Data Inventory 7

2.2.2 Data Processing 8

2.3 Seasonal Circulation 9

2.3.1 Data Overview 9

2.3.2 Velocity Profile 15

2.3.3 Deep water renewal 17

2.4 Wind-Driven Response 21

2.4.1 Wind-driven Currents 21

2.4.2 Surface Slope Response 23

2.4.3 Barotropic and Baroclinic Response 24

2.5 Volume Budget and the Surface Outflowing Layer 27

2.5.1 Volume Budget 27
2.5.2 Surface Outflowing Layer Thickness 29
2.6 Discussion and Summary 32
2.6.1 Seasonal Circulation 32
2.6.2 Wind-driven Circulation 35

Chapter 3 Wind-driven currents in a 'wide' narrow channel, with application to Douglas Channel, BC 39
3.1 Introduction 39
3.2 Numerical model setup 41
3.3 Results 46
3.3.1 Barotropic runs 46
3.3.2 Base run 48
3.3.3 Baroclinic runs 51
3.4 Discussion 54
3.4.1 Along-channel Surface Slope and Stratification 54
3.4.2 Surface Layer Thickness and Geostrophic Balance 56
3.4.3 Vertical Modes 59
3.4.4 Scaling of the Surface Layer Thickness 60
3.5 Summary and Conclusions 63

Chapter 4 Remote coastal trapped waves drive seasonal and intraseasonal variations in upwelling off the coast of British Columbia 66
4.1 Introduction 66
4.2 Data 69
4.3 Results 71
4.3.1 Linear regression of E01 density and upwelling indices 71
4.3.2 Analysis of E01 density and upwelling indices in frequency-time space 77
4.3.3 Sea surface height variability 82
4.4 Discussion 84
4.4.1 The weather band dynamics 86
4.4.2 Quasi-biweekly band 87
4.4.3 Intraseasonal (50–130 day) band 89

4.4.4 Generation of CTWs 90
4.4.5 Implications for regional numerical models 91
4.5 Summary 92

Chapter 5 Conclusion **94**

Appendix A Supplementary Information for Chapter 2 **97**

Appendix B Supplementary Information for Chapter 3 **105**

Bibliography **109**

List of Tables

Table 2.1 CTD depths at three moorings. *The CTD at 132 m at HEC1 failed on Nov 28, 2014. 8

Table 2.2 Volume budget at FOC1 and KSK1. Negative numbers represent seaward flow, and positive numbers represent landward flow. The cross-channel widths (w_f for FOC1 and w_k for KSK1) at these two stations are parameterized as a function of depth (d): $w_f(d) = -7.7 \cdot d + 3770$ m, $w_k(d) = -10.2 \cdot d + 5286$ m, with d going from 0 to 360 m (results are from linear fits). The volume transport of each layer is then calculated by integrating the velocity profile (obtained from the cubic spline fits, Figure 2.5) over the cross-sectional area of the corresponding layer, assuming no cross-channel variation. The cross-sectional areas for FOC1 and KSK1 are $860,000$ m^2 and $1,242,000$ m^2, respectively. 38

Table 3.1 Model Setups. r$_1$s are the barotropic runs. The salinity at $z[-15, 0]$ (from -15 m to surface) is $-\frac{c_0 \cdot (z+15)}{15} + 30.7$, and the salinity at $z[\text{bot}, -15]$ (from the bottom to -15 m) is $33 - 3 \cdot \exp(z/50)$. c_0 is shown in the table. 47

Table 3.2 Surface Slope Results 51

Table 3.3 Decomposition results. 61

Table 4.1 Linear regression results (summary of Figure 4.5). The 'rmse' is the root-mean-square errors of the prediction. 76

Table A.1 Wind and current velocity correlations. u_F denotes the current velocity at FOC1, and u_K denotes the current velocity at KSK1. Both the wind velocities and the current velocities are Godin low-passed, and the effective degrees of freedom (N_e) is calculated by $N/67$, where the energy amplitude drops to half at T = 67 h for the Godin filter. The peak correlations occur when the surface current velocity term lags the wind velocity term by the hours listed in the 'lag' column. Using the wind velocity (x) as the predictor variable, a linear regression model can be set up as $y \sim mx + b$, where y is the surface current velocity. The root-mean-square deviation (rmsd) is used to measure the difference between the estimated and the observed current velocities. All uncertainties are calculated at the 95% significance level. 101

Table A.2 Regression results between the wind stress and the barotropic pressure gradients derived from $\tilde{\tau}_w = h_1\rho_1 g\frac{\partial\tilde{\eta}_1}{\partial x}$ and $h_1\rho_1 g\frac{\partial\overline{\eta}_1}{\partial x} - \overline{\tau}_w + \overline{\tau}_{h_1} = 0$. So $\overline{\tau}_{h_1}$ can be estimated from the intercept (b) of the regression fit: $\overline{\tau}_{h_1} = \overline{\tau}_w - h_1\rho_1 g\frac{\partial\overline{\eta}_1}{\partial x}$. r is the correlation coefficient between the wind stress anomaly $\tilde{\tau}_w$ and the barotropic pressure gradient anomaly $\rho_1 g\frac{\partial\tilde{\eta}_1}{\partial x}$. The peak correlations occur when the surface elevation gradient anomaly term lags the wind stress term by the hours listed in the 'lag' column. All uncertainties are calculated at the 95% significance level. 102

Table A.3 Correlations between the wind velocity and the surface potential density anomalies. The potential density anomalies are calculated from the surface observations obtained at FOC1 and KSK1 (Table 1). In all periods listed here, the density anomalies lag the wind velocity. The peak correlations occur when the density anomaly term lags the wind velocity term by the hours listed in the 'lag' column. All uncertainties are calculated at the 95% significance level. 103

Table A.4 Regression results between the barotropic and baroclinic pressure gradients. The barotropic pressure gradient is the surface pressure gradient anomalies ($\frac{\partial \tilde{\eta}_1}{\partial x}$) between Stations Kitimat and Hartley Bay (Figure 1). The baroclinic pressure gradient is calculated from the surface potential density anomalies ($-\frac{g}{\rho_0}\frac{\partial \tilde{\sigma}_\theta}{\partial x}$) between FOC1 and KSK1 (Figure 1). As explained in Section 4.3, the slope estimation h_1 is the averaged balancing depth where barotropic and baroclinic pressure gradients balance each other. The peak correlations occur when the baroclinic term lags the barotropic term by the hours listed in the 'lag' column. All uncertainties are calculated at the 95% significance level. 104

List of Figures

Figure 2.1 (a) Bathymetry of the west coast Canada. The Kitimat system is the region marked with the red square that is zoomed in (b) Kitimat system bathymetry and locations of observation stations. Mooring stations (round circles), river gauges (triangles), Environment Canada Buoys (diamonds), and tide gauge locations (squares) are marked on the map. The bathymetry along the red along-channel route is shown in (c), along with the two mooring locations and the current velocity data availability during two deployments (ADCP denotes Acoustic Doppler Current Profiler; CM denotes single point current meter). 6

Figure 2.2 Time series (positive velocity points to up-fjord) of (a) the hourly Kitimat and Kemano River discharge, (b) the low-passed wind velocity measured at EC46181, (c and d) the low-passed surface, mid-depth, and the bottom current velocities at KSK1 and FOC1, respectively, and (e) the bottom Absolute Salinity at three mooring stations. Figure A.2 and Figure A.3 show the zoomed in version during the renewal seasons in 2014 and 2015 respectively. 10

Figure 2.3 Low-passed ADCP velocity time series for the period July 3, 2014 to Jul 22, 2015 from mooring FOC1: (top) the upward looking ADCP at 38 m depth, and (bottom) the downward looking ADCP at 260 m depth. The red colour (positive) represents the in-fjord direction velocity, and the blue colour (negative) represents the down-fjord direction velocity. 13

Figure 2.4 Low-passed ADCP velocity time series for the period July 2, 2014 to Jul 22, 2015 from mooring KSK1: (top) the upward looking ADCP at 39 m depth, and (bottom) the upward looking ADCP at 360 m depth. The red colour (positive) represents the in-fjord direction velocity, and the blue colour (negative) represents the down-fjord direction velocity. 14

Figure 2.5 Seasonal mean along-channel velocity at Station FOC1 (53.736° N, 129.030° W) and KSK1 (53.480° N, 129.209° W) in Douglas Channel. The observed mean velocities are averaged after applying the low-pass filters, the solid lines are the cubic splines fitted to the observed mean velocities, and the dashed lines (μ values) are the vertically averaged velocity from the surface (0 m) to the bottom (360 m) computed from the spline fits. μ(wind) is the averaged along-channel wind velocity during each time period in the channel. 16

Figure 2.6 (a) Absolute Salinity at the bottom of the three stations during the renewal in 2014. (b) Bottom along-channel velocities (raw and low-passed) at FOC1 during the renewal in 2014. The bottom current meter at KSK1 failed on May 10, 2014, so there are no bottom current observations in the outer basin that captured this summer renewal process. The salinity timeseries during renewal periods are also included in Figure A.2 and A.3 in the Supporting Material. 18

Figure 2.7 Left panel: correlation coefficients r (blue stars) between the along-channel wind velocity and the along-channel current velocities measured at KSK1. Right panel: The time lags for the along-channel wind velocity and the along-channel current velocity to reach the maximum correlation (the green circles in the left panel are the maximum correlation coefficients given the corresponding time lags). The 95% confidence limit for r is labeled in the red line (i.e. when the absolute value of the red line is larger than 0, it is considered as statistically significant but not necessarily practically significant). The regions where r is within $[-0.4, 0.4]$ (i.e. $r^2 < 0.16$) are considered practically not significant for this study and shaded in gray. The time period chosen for this analysis is from Jan 13 to Jul 25, 2015, where we have continuous concurrent current velocity and wind observations. 21

Figure 2.8 Time series of the barotropic ($g\frac{\partial \eta_1}{\partial x}$, blue) and baroclinic ($-h_1\frac{g}{\rho_0}\frac{\partial \tilde{\sigma}_\theta}{\partial x}$, red) forcing terms. These two time series are correlated ($r = 0.73 \pm 0.07$), and the fitted coefficient of the linear fit is 34 ± 6 m corresponds to the depth at which these two forcing terms balance each other. The peak correlation occurs when the elevation difference lags the density difference by 10 ± 18 hours (95%). . 26

Figure 2.9 Absolute Salinity at the head (solid lines), FOC1 (dashed lines) and at the mouth (dash-dotted lines) of Douglas Channel. The summer data is the average of the July 2013 and July 2014 cruise CTDs, and the winter data is the average of April 2014 and October 2014 cruise CTDs. The vertically averaged Absolute Salinities (in g kg^{-1}) for layers 1 and 2 at the head are: S_1(summer)= 28.41, S_2 (summer)= 31.94; S_1(winter)= 27.75, S_2 (winter)= 32.02; at FOC1: S_1(summer)= 29.00, S_2(summer)= 32.09; S_1(winter)= 28.80, S_2 (winter)= 32.05; at the mouth: S_1(summer)= 30.02, S_2(summer)= 32.00; S_1(winter)= 29.02, S_2 (winter)= 32.03. 29

Figure 3.1 Map of Kitimat system. For the purpose of the paper here, we consider Douglas Channel, the main waterway of the system, as the channel from the northern end close to DOUG4 to the shelf. The 200 m deep sill is located between FOC1 and DOUG40. The observed wind data are taken from the Nanakwa Shoal buoy. FOC1, DOUG4, DOUG40 are the locations of CTD stations. . 42

Figure 3.2 Top view of the setup of ROMS model. Wind stress is applied uniformly in the entire domain with linear damping within the sponge layer. The bottom friction in the sponge layer increase linearly from east to west. 44

Figure 3.3 Observed and the base run initial Absolute Salinity. The inner basin location is at FOC1 and the outer basin location is at KSK1. The summer profile is averaged from the July 2013 and July 2014 cruise CTD data, and the winter profile is averaged from the April 2014 and October 2014 cruise CTD data. 45

Figure 3.4 Plan view of the surface elevation η, and surface velocity in case r_{3_3}. Top: Sea surface elevation contour plot; second: surface velocity quiver plot; third: eastward (along-channel) velocity (u); bottom: northward (cross-channel) velocity. 49

Figure 3.5 Contours of the along-channel velocity in experiment r_{3_3}. Looking into the channel denotes looking from the west to the east direction. Red is in the up-fjord direction. The inner basin cross-section is taken at about 40 km from the head of the closed east end representing FOC1, and the outer basin cross-section is taken at about 80 km from the head of the closed end of the channel representing KSK1. 50

Figure 3.6 Surface elevation slopes in 4 different initial stratifications averaged between Day 15 and Day 20. $N = \sqrt{\frac{g}{\rho_0}\frac{\rho(40)-\rho(0)}{40\mathrm{m}}}$, where $\rho_0 = 1025$ kg m^{-3}. 50

Figure 3.7 Surface velocity layer thickness in the low wind and the high wind cases and the surface stratification. The thicknesses are calculated in the inner basin. 52

Figure 3.8 Along-channel surface velocity at 5 m depth in cases with different initial stratifications and for the barotropic runs. The velocities were taken from the top layer. Left: averaged surface velocity and N between Day 2 and Day 5; right: averaged between Day 15 and 20. The surface velocity and N are averaged in the cross-channel direction at 40 km from the eastern boundary. 52

Figure 3.9 Surface velocity layer transport in the low wind and the high wind cases and the surface stratification. The transports are calculated in the inner basin. 53

Figure 3.10Surface elevation slope ($\Delta\eta/\Delta x$) and the density slope ($\Delta\rho/\Delta x$ at 12 m depth) between the inner and the outer basins. 54

Figure 3.11Top: Low-passed surface elevation slope from observations and the wind stress in Douglas Channel from July to Nov 2015. Bottom: wind stress divided by $\rho_0 g\frac{\partial\eta}{\partial x}$, and the results are h_s, where h_s is the measure of stratification explained in Equation 3.3. The surface slope is calculated from the elevations in Kitimat and Hartley Bay. The wind data and the elevation data are resampled every hour and the Godin filter is used to remove high frequency signals. In the lower panel, $\frac{\partial\eta}{\partial x}$ values in the range [-0.1, 0.1] $\cdot 10^{-6}$ were deleted avoid near 0 values. 57

Figure 3.12Integrated acceleration diagnostic terms from Day 0 to Day 2 in case r_{4_3}. The x axes are truncated in order to show the structure of the other terms. The x-dir is in the along-channel direction, and the y-dir is in the cross-channel direction. 58

Figure 3.13Vertical modes (r_{2_3} as an example) from the inner (left) and the outer (right) basins. The black lines represent the velocity profiles. The vertical modes are calculated numerically using the density profile in the middle of the channel. 60

Figure 3.14The surface velocity thickness averaged cross-channel and the scaling factors in 4 different cases. 62

Figure 4.1 Map showing the locations of meteorological and oceanographic observation sites mentioned in this study. 70

Figure 4.2 a) Time series of salinity and temperature at E01 at 75 m depth. b) Density time series of E01 at 75 m and the Bakun indices at 39°N and 48°N. c) Density time series of E01 at 35 m and 75 m. 72
Figure 4.3 Lagged correlations between the low-passed density at E01 at 75 m and upwelling indices at three latitudes. Positive lag is for Bakun index leading. 73
Figure 4.4 Power spectral density of E01 density with 95% confidence intervals. Note that the M2 and K1 tidal components are at the right end of the curve where it drops from f^{-1} trend. 74
Figure 4.5 Linear regression results between the 10-day averaged density at E01 (75 m) and the 10-day averaged upwelling indices. 75
Figure 4.6 Wavelet coherence amplitude-squared between the E01 (75 m) water density and Bakun upwelling indices from 21°N to 36°N. The values encompassed by the black lines are the squared coherence values exceed the 95% confidence interval. The arrows in the figure shows the phase angle: pointing right indicates 0° lag, and pointing upward (downward) indicates density lagging (leading) wind by 90°. The arrows are only plotted where the coherence squared values exceed 0.5 (roughly at the 95% level). 78
Figure 4.7 Wavelet coherence amplitude squared between the E01 (75 m) density and Bakun upwelling indices from 39°N to 54°N. The values encompassed by the black lines are where the confidence interval exceed the 95% confidence interval. The arrows in the figure shows the phase angle: pointing right indicates 0° lag, and pointing upward (downward) indicates density lagging (leading) wind by 90°. The arrows are only showing where the coherence squared values exceed 0.5 (roughly at at 95% level). 79
Figure 4.8 Temporally averaged wavelet coherence squared for Figures 4.6 and 4.7. The squared coherences are averaged over the entire time period of 2010 to 2013. Note that E01 is at 49.3°N 80

Figure 4.9 Wavelet coherence amplitude squared between 48°N and other latitudes. The values in the black lines are where the confidence interval exceed 95%. The arrows in the figure shows the phase angle: pointing right indicates 0° lag, and pointing upward (downward) indicates Bakun index at 48°N lagging (leading) the other index by 90°. The arrows are only showing where the coherence squared values exceed 0.5 (roughly at 95% level). . . . 81

Figure 4.10 Wavelet coherence amplitude squared between SSHs at Tofino (49.15°N, 125.92°W) and Bella Bella (52.17° N, 128.13°W). The values encompassed by the black lines exceed the 95% confidence interval. The arrows in the figure shows the phase angle: pointing right indicates 0° lag, and pointing upward (downward) indicates Bella Bella SSH lagging (leading) Tofino by 90°. The arrows are only showing where the coherence squared values exceed 0.5 (roughly at the 95% level). The bottom panel shows the phase lag where the coherence squared exceeds the 95% confidence level. The phases are converted to time values, i.e. Bella Bella lagging Tofino by 90° at a 12-day period indicates a time lag of 3 days. Negative phases mean Bella Bella leads. 83

Figure 4.11 Wavelet coherence amplitude squared between SSHs at Tofino (49.15°N, 125.92°W) and Bella Bella (52.17°N, 128.13°W) and Bakun upwelling indices (top four) and E01 density (bottom two). The values encompassed by the black lines exceed the 95% confidence interval. The arrows in the figure shows the phase angle: pointing right indicates 0° lag, and pointing upward (downward) indicates SSH lagging (leading) wind (top four) or E01 density (bottom two) by 90°. The arrows are only showing where the coherence squared values exceed 0.5 (roughly at 95% level). 85

Figure A.1 Top 35 m Potential Density at the head (solid lines), FOC1 (dashed lines) and at the mouth (dash-dotted lines) of Douglas Channel. The summer data is the average of the July 2013 and July 2014 cruise CTDs, and the winter data is the average of April 2014 and October 2014 cruise CTDs. 98

Figure A.2 Absolute Salinity (raw) at the bottom of the three stations during the renewal in 2014. 98
Figure A.3 Absolute Salinity (raw) at the bottom of the three stations during the renewal in 2015. Note that there is an interannual variability between 2014 and 2015 renewal events. 99
Figure A.4 ADCP profiles at FOC1 2013–2014. 99
Figure A.5 ADCP profiles at KSK1 2013–2014. 100

Figure B.1 Upper: The lowpassed along-channel surface slope anomalies and the wind stress between Oct 15 to Nov 15, 2015. The vertical blue lines represent the time when the CTD profiles were taken. Lower: Daily Kitimat River discharge. 106
Figure B.2 Potential density profiles at Station Doug4 and Doug40 during 2015-54 in the top 50 m. The solid profiles are from Doug 40, where it is close to Hartley Bay. The dashed lines are from Doug 4, which is close to the head of the channel. 107
Figure B.3 Initial salinity in four stratified runs. 107
Figure B.4 Mixed layer depth versus the first layer thickness. The mixed layer depth is defined as the depth where the density is 0.125 kg/m^3 larger than the surface density. 108

ACKNOWLEDGMENTS

I would like to thank my supervisors and committee members Charles, Mike, Patrick, Stan, and Steve for their mentoring, guidance, encouragement, support and endless patience. Thanks also goes to Dr. Jody Klymak for supervising me during the early part of this thesis.

I would also like to thank my colleagues at the Institute of Ocean Sciences for their support, discussion and encouragement. In particular, I would like to thank Rick Thomson, Angelica Peña, Germaine Gatien, Hauke Blanken, Maxim Krassovski, Roy Hourston, Stephen Page, Lucius Perreault, and David Spear. I would like to thank my funding programs: Canada World-Class Tanker Safety System and the Oceans Protection Plan by Fisheries and Oceans Canada, and the crew members on CCG Vector and CCG Tully.

Special thanks to my husband Pramod for valuable discussions throughout this thesis and for his continuous support along the way. I would also like to thank my parents for inspiring me to finish, and my son Arjun Qi for being cute.

Chapter 1

Introduction

Increased marine activities in Kitimat, British Columbia (BC), Canada, require an improved understanding of the physical oceanography of the region to support oil response planning, provide enhanced information for navigation, and support the management of marine resources. Previous work in the Kitimat region in the 1950s (Pickard, 1961) and 1970s (Webster, 1980a,b; Macdonald, 1983) was not able to provide a full description of the water column circulation due to the instrument limitations at the time. More recent observations (from 2013 to 2016) of current velocities and water properties in the main channel (Douglas Channel) in the Kitimat fjord system allow us to examine the full water column circulation structure and the deep water renewal processes.

The exchange of the deep-basin water is important for biological productivity. The classic deep-water renewal theory will be able to explain the summer renewal events that we observed in Douglas Channel: when dense water becomes available in the early June, it renews the basins, and the deep-basin residence water gets lifted by the intrusion. Deep water renewals in deep-silled fjords in Norway and Alaska are usually linked with the seasonal wind field. However, with no strong correlation between the local Hecate Strait wind and the deep-water renewal events, dense water still becomes available in summer at the mouth of Douglas Channel. The search for possible mechanisms that drive dense water to the shelf naturally becomes the next question for this study.

The primary objective of this thesis is to gain an improved understanding of the circulation and the deep water renewal process in Douglas Channel. Three main questions are posed to address this:

1. What are the oceanographic processes that control the sub-tidal circulation in the deep-silled Douglas Channel?

2. What is the wind-driven circulation in Douglas Channel?

3. What are the local and remote influences of upwelling on the BC shelf?

Regarding these questions, I make and support three claims in my thesis and each claim corresponds to one paper chapter:

1. Douglas Channel is well connected to the adjacent shelf region through the surface estuarine circulation and the deep water renewals;

2. Physically narrow channels can be dynamically wide in the case of strong surface stratification;

3. The water properties at the bottom of the BC shelf are influenced by the northern California coast and the equatorial regions.

Claim 1 is validated by examining the sub-tidal vertical current velocity profiles. It implies that:

- Wind stress in Douglas Channel influences the circulation through both barotropic and baroclinic responses.

- The deep water renewal is controlled by the availability of dense water on the continental shelf of BC.

Claim 2 is concluded after analysing idealized numerical model results. It implies that:

- For inlets with strong surface stratification, pronounced cross-channel variability could occur even if the channel is physically narrow.

- The wind-driven surface layer can be much thicker than the highly stratified surface layer.

Claim 3 is supported by evidence that coastal trapped waves generated from the northern California and Oregon coasts are propagating to the BC coast. The consequence of claim 3 is that:

- Studies of upwelling on the BC coast need to consider influences from the equatorial and mid-latitude regions.

1.1 Thesis structure

The following three chapters correspond to three sand-alone papers to address the three questions posed. The first two of these chapters have been published; the third is to be submitted shortly.

Chapter 2 [published as Wan et al. (2017)] studies the sub-tidal current velocity profiles in Douglas Channel and finds that the sub-tidal circulation is a combination of estuarine flow, wind-driven flow, and the barotropic and baroclinic responses driven by wind stress, and that the deep water renewals connect the basin water with the continental shelf of BC.

Chapter 3 [published as Wan et al. (2022)] examines wind-driven flow in an idealized stratified channel that represents Douglas Channel. It is found that the wind forcing can produce cross-channel variability even in narrow channels given strong surface stratification, and the surface wind-driven layer can be thicker than the highly stratified surface layer.

Chapter 4 (to be submitted) connects Douglas Channel to remote influences. The deep water renewals in Douglas Channel are determined by the availability of the dense water on the BC shelf. By presenting evidence of coastal trapped waves propagating from the northern California and Oregon coasts to BC, the driving force for the upwelling on the BC coast is now expanded to the northern California and Oregon coasts and even the equatorial region.

Finally **Chapter 5** brings individual chapters together and provides advice for future studies.

Chapter 2

Sub-tidal circulation in a deep-silled fjord: Douglas Channel, British Columbia

Abstract

Douglas Channel, a deep fjord on the west coast of British Columbia, Canada, is the main waterway in the fjord system that connects the town of Kitimat to Queen Charlotte Sound and Hecate Strait. A 200 m depth sill divides Douglas Channel into an outer and an inner basin. This study examines the low-frequency (from seasonal to meteorological bands) circulation in Douglas Channel from data collected at three moorings deployed during 2013–2015. The deep flows are dominated by a yearly renewal that takes place from May/June to early September. A dense bottom layer with a thickness of 100 m that cascades through the system at the speed of 0.1–0.2 m s^{-1}, which is consistent with gravity currents. Estuarine flow dominates the circulation above the sill-depth, and the observed landward net volume flux suggests that it is necessary to include the entire complex channel network to fully understand the estuarine circulation in the system. The influence of the wind forcing on the sub-tidal circulation is not only at the surface, but also at mid-depth. The along-channel wind dominates the surface current velocity fluctuations and the sealevel response to the wind produces a velocity signal at 100–120 m in the counter-wind direction. Overall, the circulation in the seasonal and the meteorological bands is a mix of estuarine flow, direct wind driven flow, and the barotropic and baroclinic responses to changes to the surface pressure gradient caused by the wind stress.

2.1 Introduction

The north coast of British Columbia is a complex network of islands, waterways, mountains and deep fjords (Figure 2.1). This area is at the core of the region called the Great Bear Rainforest (Young et al., 1997), which has been the subject of extensive planning to reduce land use conflicts (Saarikoski et al., 2013; Government of British Columbia, 2016). Increased marine activity, including proposals for the transport of diluted bitumen and liquefied natural gas (LNG) from terminals in Kitimat BC, requires an improved understanding of the physical oceanography of the region to support oil response planning and to provide enhanced information for navigation. In addition, there is an increasing need for oceanographic information to support both conservation goals and the management of the marine resources.

The oceanography of the adjacent continental shelf was studied extensively from 1982 to 1995. (Crawford, 2001, contains an extensive bibliography and much of the data) but there has been much less work done in the inlets and fjords. The first systematic observational program was George Pickard's pioneering fjord work in the 1950s (Pickard, 1961). During 1977 and 1978 extensive measurements were made in Douglas Channel in relation to a large hydropower project (Webster, 1980a,b; Macdonald, 1983). These studies provide basic descriptions of the water properties, the estuarine nature of the surface flows, and the importance of the wind forcing on the surface currents. Douglas Channel can be classified as a partially mixed estuary by the classification given by Hansen and Rattray (1966), having a smooth density transition between the freshwater layer and the bottom. There was also the indication of a summertime renewal of the deep water. Webster (1980b) and Macdonald et al. (1983) concluded a complete replenish of the basin water based on the changes in T/S graphs between July and September. However, due to instrument limitations at the time, these early studies were unable to describe the circulation structure of the entire water column or to provide a definitive description of the deep basin water exchange, but they motivate us to quantitatively describe the circulation, including the renewal event in the deep basin.

The focus of this paper is Douglas Channel, the component of the main navigation channel which extends from Kitimat to Gil Basin (just beyond Hartley Bay), a distance of about 90 km (Figure 2.1). A comprehensive description of the region is provided by Macdonald (1983); here we summarize some relevant details. Douglas Channel is one component of the fjord system that connects the inland waters with

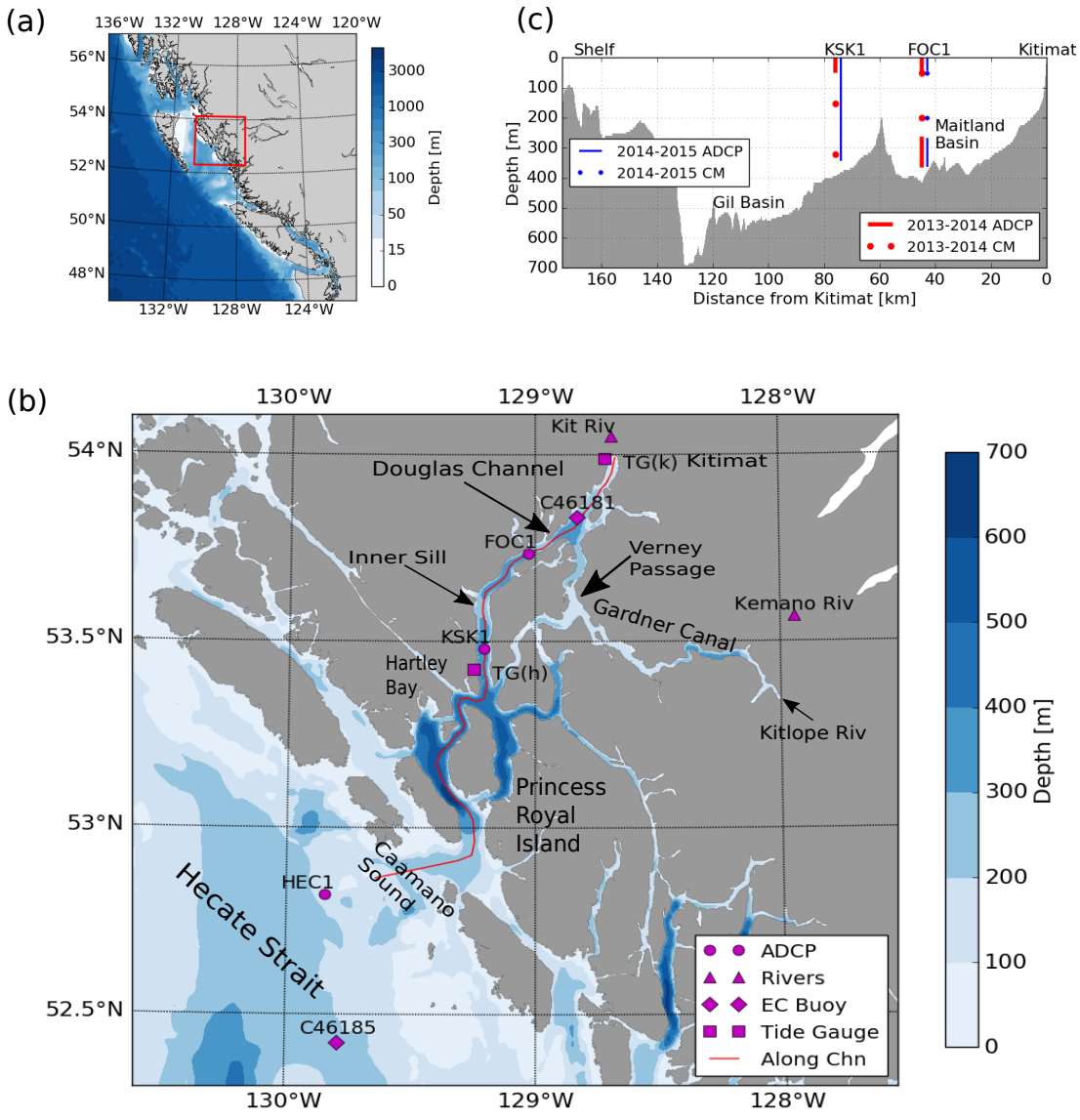

Figure 2.1: (a) Bathymetry of the west coast Canada. The Kitimat system is the region marked with the red square that is zoomed in (b) Kitimat system bathymetry and locations of observation stations. Mooring stations (round circles), river gauges (triangles), Environment Canada Buoys (diamonds), and tide gauge locations (squares) are marked on the map. The bathymetry along the red along-channel route is shown in (c), along with the two mooring locations and the current velocity data availability during two deployments (ADCP denotes Acoustic Doppler Current Profiler; CM denotes single point current meter).

Hecate Strait via long, narrow and deep channels. The distance from the mouth of the Kitimat River to Hecate Strait is about 140 km. An important feature of the system is that the fjord sills are relatively deep. The extended sill where the fjord system connects with Hecate Strait is about 140 m deep, and the inner sill is about 200 m deep. With the focus on Douglas Channel, the inner sill between the mooring locations at FOC1 and KSK1 is of particular interest here; it is about 200 m deep in the middle of the channel and 220 m deep on the sides (Figure 2.1b). This sill separates the basins into an inner basin (Maitland Basin, landward) and an outer basin (Gil Basin, seaward). Shallow silled fjords such as Knight Inlet (60 m sills), an extensively studied fjord at the southern end of the Great Bear Rainforest (Farmer and Smith, 1980; Baker and Pond, 1995), are useful but imperfect analogues for Douglas Channel. For the sub-tidal circulation in Douglas Channel, we expect estuarine flows in the upper layers, relatively quiet deep basin water, and wind driven circulation at the surface; however, different renewal processes are expected in the deep water because of the relatively deep sill.

2.2 Data Description

2.2.1 Data Inventory

Three moorings (FOC1, KSK1, and HEC1 in Figure 2.1c) were deployed from July 2013 to July 2014 and again from July 2014 to July 2015. FOC1 is located inside of the inner sill of Douglas Channel and KSK1 is located outside of the inner sill (Figure 2.1b). The most complete observations were obtained during the second deployment (2014-2015); therefore, we focus the velocity analyses on this second deployment. At FOC1, there is an upward looking ADCP at 39 m (300 kHz, 4 m bin size), single point current meters at 53 m and 200 m, a downward looking ADCP at 100 m above the bottom (300 kHz, 4 m bin size). At KSK1, there is an upward looking ADCP at 40 m (300 kHz, 2 m bin size) and at 11 m from the bottom (75 kHz, 16 m bin size), and a single point current meters at 150 m. The detailed mooring configuration can be found in Wright et al. (2016).

Continuous CTD (Conductivity, Temperature and Depth) data were collected at various depths at these three moorings (Table 2.1). Ship-based CTD profiles (Jul 2013, Apr 2014, Jul 2014 and Sep 2014) were also collected throughout the fjord system (Wright et al., 2015, 2016). The moored CTDs were calibrated before and

Table 2.1: CTD depths at three moorings. *The CTD at 132 m at HEC1 failed on Nov 28, 2014.

Station	Deployment	CTD Depth [m]
FOC1	2013-2014	16, 53, 150, 317, 353
	2014-2015	12, 36, 50, 146, 298, 354
KSK1	2013-2014	19, 154, 323
	2014-2015	15, 40,150, 362
HEC1	2013-2014	61, 133
	2014-2015	18, 42, 55, 132*

after each deployment against the ship-based CTD, and the ship-based CTD was calibrated regularly by the manufacturer, and against the water samples collected on multiple stations during each cruise. All salinity values in this paper are given on the Absolute Salinity scale.

Concurrent data that were also analyzed include sea surface elevation data [obtained from Canadian Hydrographic Service websites: `http://www.meds-sdmm.dfo-mpo.gc.ca/isdm-gdsi/twl-mne/index-eng.htm` at Kitimat (Station 9140) and Hartley Bay (Station 9130), labeled as TG(k) and TG(h), respectively, in Figure 2.1b]; wind data (taken from Environment Canada Buoys (C46181 and C46185 in Figure 2.1c); and river discharge and the precipitation records (Environment Canada Wateroffice `https://wateroffice.ec.gc.ca/google_map/google_map_e.html?searchBy=p&province=BC`). The sea surface elevation observations were corrected to an equipotential gravitational surface using the Canadian Geodetic Vertical Datum (CGVD2013) with an uncertainty as large as 5 cm (pers. comm. Bodo de Lange Boom), and averaged over 5-minute intervals to reduce high frequency noise before applying any further processing.

2.2.2 Data Processing

The sampling frequency of the observational data varied from 1 minute (e.g. sea surface elevation data) to 1 hour, except for the bottom CTD at FOC1, where sampling interval was 3 hours during both deployments. The occasional missing data were filled by linear interpolation. All data were then low-pass filtered to remove the high frequency signal as described below, and re-sampled at hourly intervals to maintain consistency with the original data.

To remove tidal currents, the Godin (1972) filter was applied as a low-pass filter, with the hourly data smoothed twice using a 24 h running average and once using a 25 h running average. This filter effectively removes all the diurnal and semi-diurnal signals, but with slight leakage in the O_1 band. While the relatively slow transition at the stop-band also leads to attenuation in the range of 2–3 days (Thomson and Emery, 2014), this simple low-pass filter is sufficient for the purpose of this paper. Unless otherwise specified, for the purpose of consistency, all data (including winds) described hereafter were low-passed with the Godin filter.

The width of Douglas Channel does not exceed 5 km and the first internal Rossby radius is about 8 km, thus we expect the cross-channel currents to be small. In addition, Douglas Channel has steep sides typical of fjords, so the wind direction is mostly confined along the channel (the cross-channel wind velocity is one order of magnitude smaller than the along-channel velocity). In this paper, we resolve the ocean currents and the wind velocities into the along- and cross-channel components, and focus on the along-channel component.

2.3 Seasonal Circulation

2.3.1 Data Overview

First we present an overview of the observational data (Figure 2.2) analysis before further analyses and discussions. As discussed above, we generally focus on the data collected during the second deployment (2014–2015), which provide better velocity coverage at KSK1. For the along-channel velocities, the up-fjord direction as defined as positive.

The freshwater input into the system comes from two sources: snow melt and rain. The time series of Kitimat River discharge (Figure 2.2a) shows that discharge due to snow melting tends to start in spring (May) and end in late summer (August), whereas discharge due to rain tends to be sporadic, and cause large and sudden discharges during winter seasons (October to March). The annual average rainfall at Kitimat (Station 08FF001) is 2.5 m per year and 4.5 m at Hartley Bay (Station 08FE003) (Environment Canada websites: `https://wateroffice.ec.gc.ca/report/`). On a cruise to the area one of the authors commented that the water seems to leap off the mountains into ocean when it rains. The very substantial local rainfall means that local run off is an important source of freshwater for the channel.

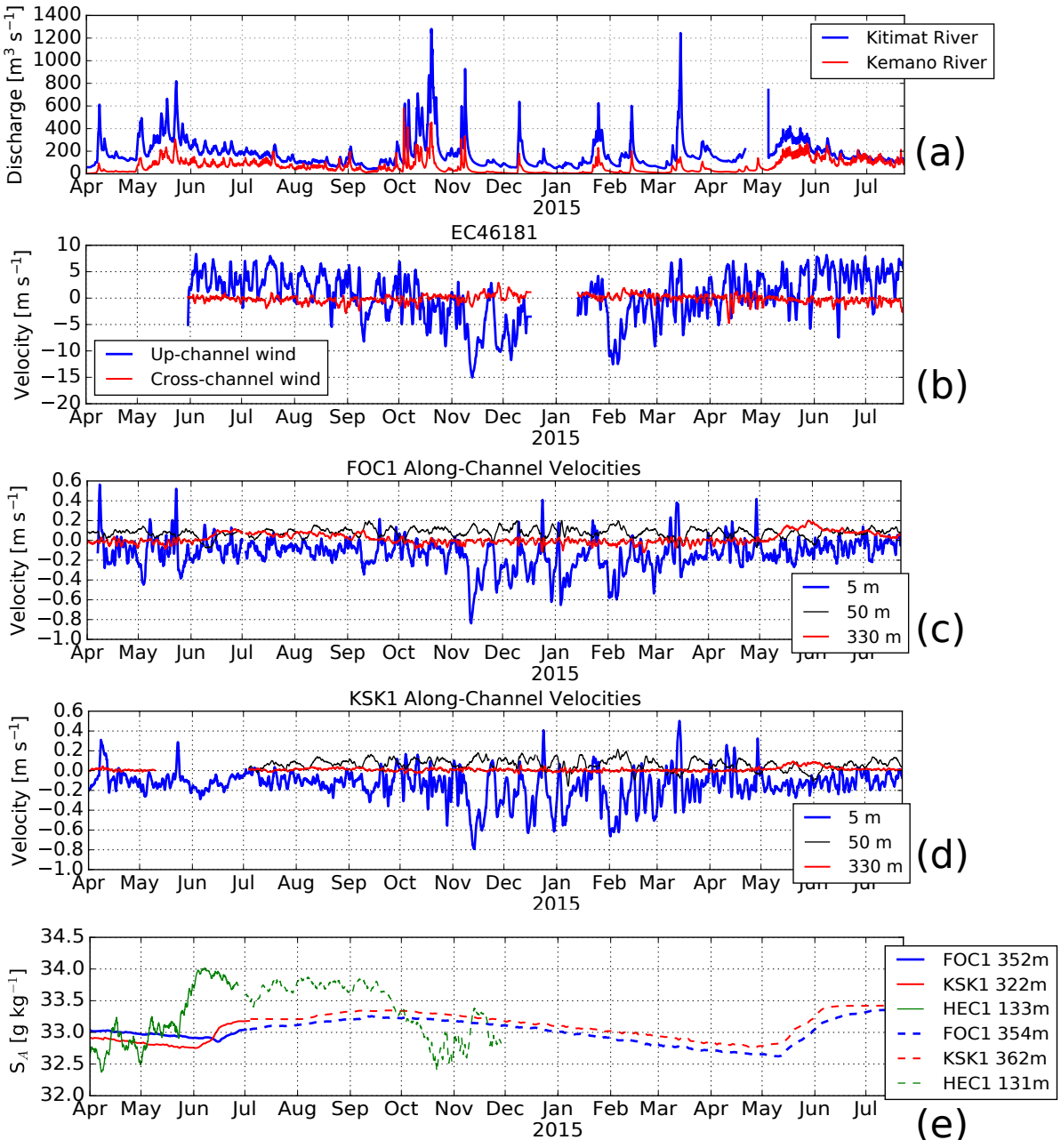

Figure 2.2: Time series (positive velocity points to up-fjord) of (a) the hourly Kitimat and Kemano River discharge, (b) the low-passed wind velocity measured at EC46181, (c and d) the low-passed surface, mid-depth, and the bottom current velocities at KSK1 and FOC1, respectively, and (e) the bottom Absolute Salinity at three mooring stations. Figure A.2 and Figure A.3 show the zoomed in version during the renewal seasons in 2014 and 2015 respectively.

Given that only two rivers in the region are gauged (the Kitimat and Kemano Rivers, Figure 1), other methods must be used to estimate the total freshwater flux into Douglas Channel and Gardner Canal. Using watershed areas, Webster (1980b) estimated that the fresh water flux into Douglas Channel was three times the Kitimat River flow and the flux into Gardner Canal was 17 times the Kemano River flow. Given mean annual fluxes of 150 m^3 s^{-1} for the Kitimat River and 45 m^3 s^{-1} for the Kemano River (averages for the period 1970-2010, Environment Canada) this yields a mean freshwater input of 1215 m^3 s^{-1} (38 km^3 per year). On the other hand, using a simplified watershed model, Morrison et al. (2012) estimated the fresh water fluxes for all the major watersheds basins in British Columbia. Consideration of the individual watersheds in the 'Caamaño' region shows that the total annual freshwater flux into Douglas Channel and Gardner Canal is 1270 m^3 s^{-1} (40 km^3 per year) with 40% into Douglas Channel and 60% into Gardner Canal (Pramod Thupaki and John Morrison, pers. comm. 2016). Their results also showed that the interannual variability was about 10% of the mean. Thus the two estimates are consistent.

The only weather buoy (EC46181) located in the channel is between Station FOC1 and Kitimat (Figure 2.1). From April to August, the average wind direction is up-fjord and the magnitude is smaller than 7 m s^{-1}. Starting from September to October, the mean wind shifts to down-fjord easterly winds (Figure 2.2b). Episodes of strong down-fjord winds (10–15 m s^{-1}) can last for a few days (e.g. Feb 2015). On occasion, the anemometer sensor may freeze during winter. For example, during our deployments, the anemometer stopped working from early February to May 2014 and again from mid-December 2014 to early January 2015.

Surface, mid-depth and the bottom low-passed velocities at FOC1 and KSK1 are shown in Figure 2.2c, d. The variation in the surface (5 m) current velocities at both FOC1 and KSK1 is clearly connected with the along-channel wind, and we discuss this connection in detail in the next section. The velocities at the surface and the mid-depth (at 50-100 m) suggest a persistent estuarine circulation pattern, such that the surface velocities are in the down-fjord direction and the mid-depth velocities are generally in the up-fjord direction. The velocities at the bottom in both basins are smaller than near the surface but are not negligible. In summer (May - September) they are typically about 10 cm/s; in winter, they are around 3–5 cm/s. A closer examination shows that the bottom water undergoes a renewal cycle that lasts for 3 to 4 months in summer as indicated by the changes of the salinity (June to September in Figure 2.2e). This renewal signal is also accompanied by an up-channel bottom

velocity as shown in Figure 2.3b and 2.4b. The bottom salinity increases rapidly over two weeks in 2014 (the first two weeks of June for KSK1, and the last two weeks of June for FOC1), and over four weeks in 2015 (both KSK1 and FOC1); the salinity then gradually increases throughout the summer in 2014 until September (Figure 2.2e). Unfortunately, the bottom CTD at HEC1 on the shelf failed at the end of November 2014, but from the bottom salinity measured during the first deployment (2013–2014, shown in Figure 2.2e, solid lines), we can see that the increase of the basin water salinity follows a rapid increase of the shelf bottom salinity (HEC1), and this increases stops at the end of September when the shelf bottom salinity starts to slowly decline until the next renewal event.

The deep density increase at HEC1 is likely caused by the regional transition from the downwelling to upwelling favourable winds in May/June (Thomson, 1981), and this condition lasts until August - September. This seasonal transition in the wind can also be seen from the wind timeseries inside Douglas Channel. From September to mid October 2014, the wind transitions from up-fjord direction to down-fjord direction, and it transitions back around May 2015.

Not only does the renewal inflow affect the bottom basin flow patterns, it also affects the vertical structure of the currents. Looking at the velocity profiles (Figure 2.3 and 2.4), we see an inflow of bottom water extending from about 150 m to the bottom at both KSK1 and FOC1 stations from May to mid-September. The roughly 50 m thick outflowing layer at 180–230 m depth at KSK1 from Nov 2014 to March 2015 in Figure 2.4b is lifted by the bottom renewal layer to about 100 - 150 m depth during renewal periods with transition periods in between. The surface 40 m profile also reflects this seasonal difference. At KSK1 (Figure 2.4a), the outflowing surface layer is about 30 m thick in summer (May to September), and thinner but highly variable in winter (October to April). The timing of the renewal event is generally consistent with the timing of upwelling to downwelling to upwelling transitions (Thomson, 1981), the wind patterns inside of Douglas Channel (Figure 2.2b) and the salinity patterns at HEC1 (Figure 2.2e). We therefore divide the time series into two different seasons: the summer renewal season (from early May to mid-September) and the winter season (mid-September to early May).

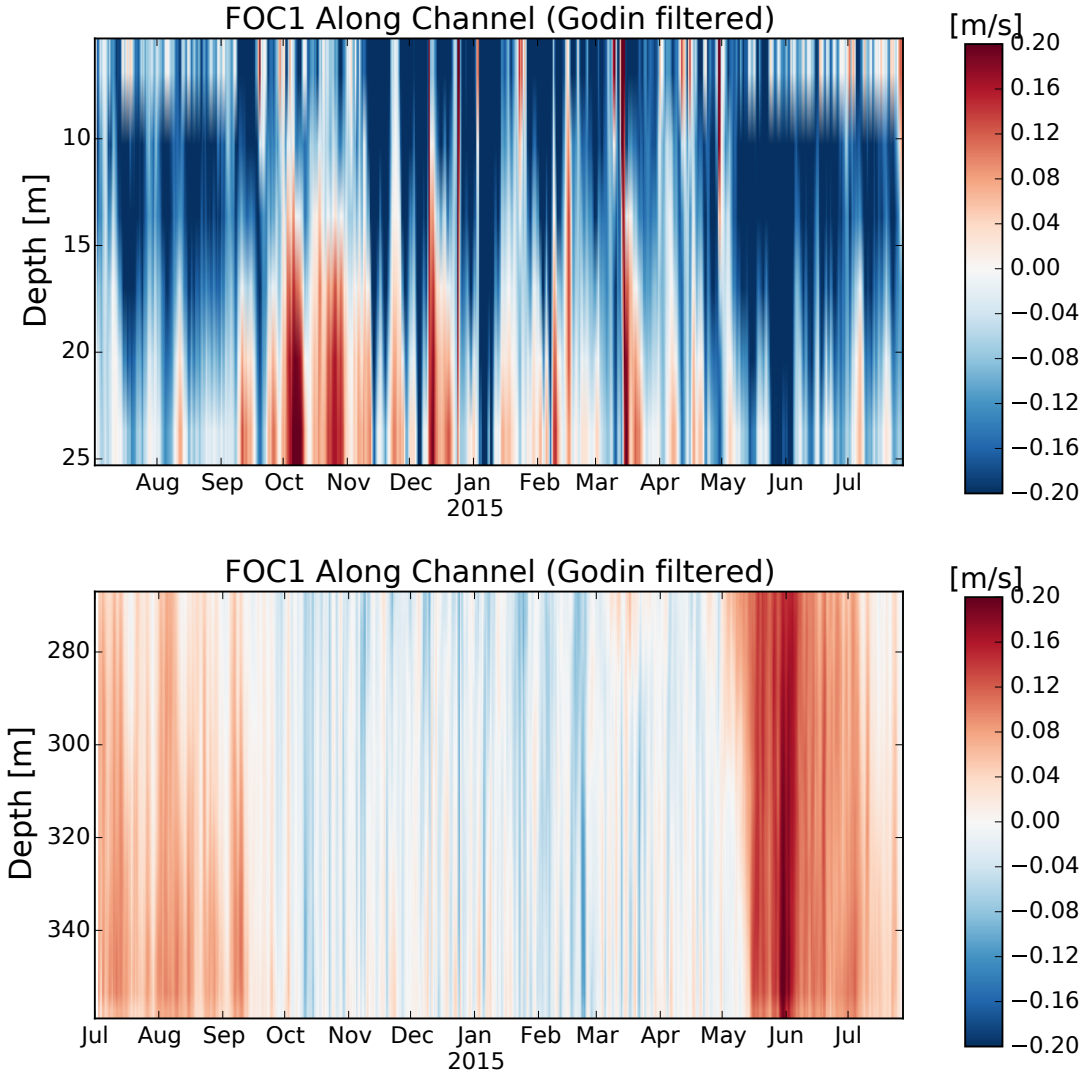

Figure 2.3: Low-passed ADCP velocity time series for the period July 3, 2014 to Jul 22, 2015 from mooring FOC1: (top) the upward looking ADCP at 38 m depth, and (bottom) the downward looking ADCP at 260 m depth. The red colour (positive) represents the in-fjord direction velocity, and the blue colour (negative) represents the down-fjord direction velocity.

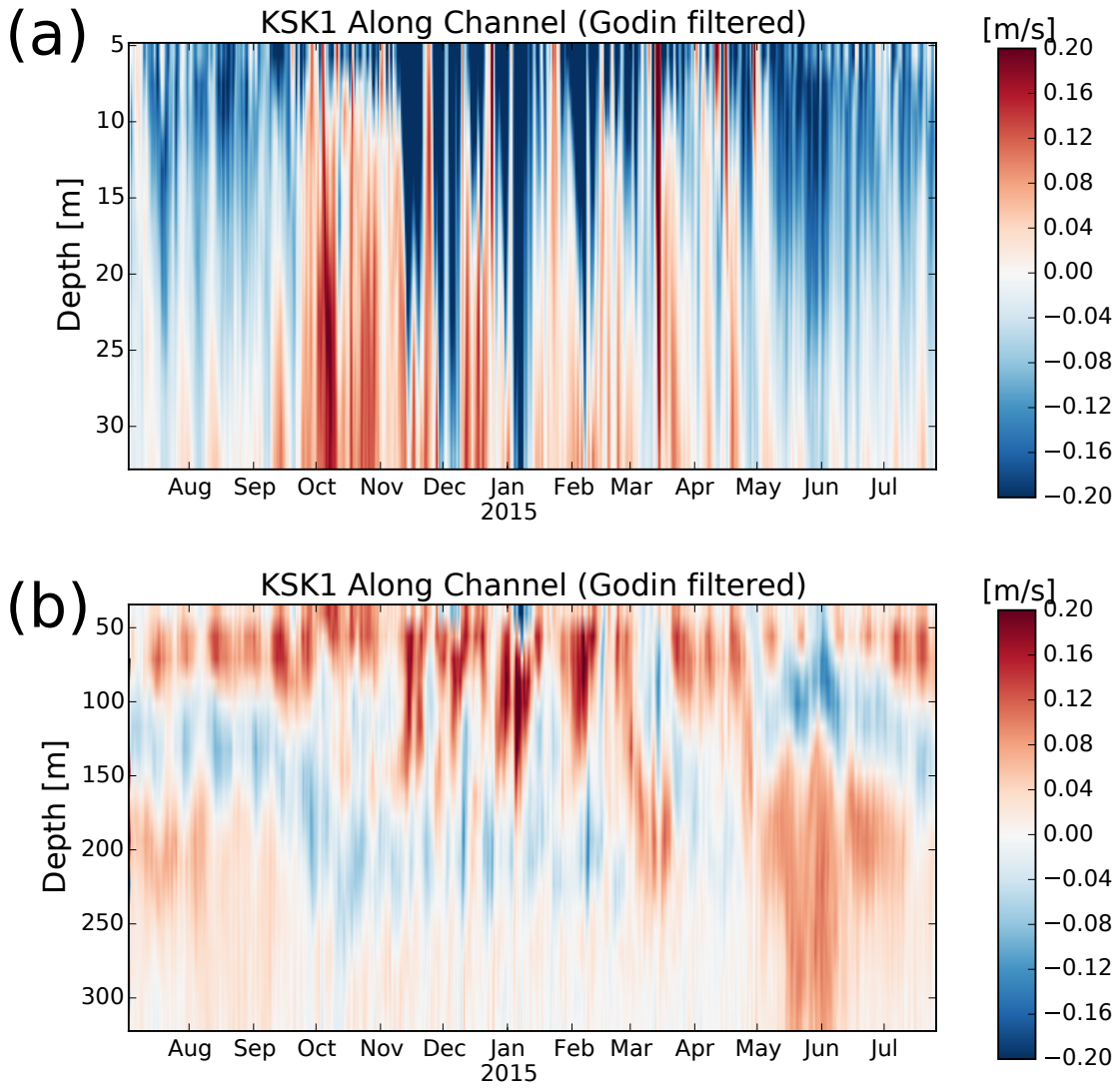

Figure 2.4: Low-passed ADCP velocity time series for the period July 2, 2014 to Jul 22, 2015 from mooring KSK1: (top) the upward looking ADCP at 39 m depth, and (bottom) the upward looking ADCP at 360 m depth. The red colour (positive) represents the in-fjord direction velocity, and the blue colour (negative) represents the down-fjord direction velocity.

2.3.2 Velocity Profile

The most striking feature of the velocity profiles is the difference in the layer structure between summer and winter (Figure 2.5) with 4 layers present in summer and 3 in winter. The layer structure is common between stations FOC1 and KSK1. In both seasons, the upper two layers are estuarine-like with surface outflow and inflow immediately below. Seasonal changes occur in the lower water column. The summer data show the deep inflow of the renewal water with a compensating outflow layer above, whereas the winter shows a weak outflow. At the surface the average up-fjord winds in the summer ($\approx$ 3 m s^{-1}) reduce the surface velocities; the effect is more pronounced at FOC1 than KSK1. The features of the seasonal velocity structure are also evident in the 2013-14 data at FOC1 and KSK1 (Figure A.4 and A.5 in the Supporting Information). The data coverage at KSK1 in 2013-14 did not allow for a full water column analysis, but the structure in the upper 50 m is consistent with that shown here. In Figure 2.5, the time periods for the summer averaging are July 2 to September 10, 2014 and May 11 to July 22, 2015, while the time period for the winter averaging is September 11, 2014 to May 10, 2015. For both stations, there were no reliable measurements of velocity at depths shallower than 5 m or deeper than 360 m, due to the mooring configurations.

In the spline fits, the curves were interpolated and extrapolated from 0 m to 360 m to illustrate the velocity layer structure and for the layer transport calculations. Given that the depths at these two stations are about 380 m, this treatment means we do not take the bottom 20 m into account, although we do not expect large velocities there. The top 5 m velocities are extrapolated from the observations, but the contribution of the top 5 m to the mean profile is less than 0.001 m s^{-1} so this extrapolation is not a big contributor to the net flux that is analyzed later.

There are detailed differences in the vertical structures of the deep flows at KSK1 and FOC1. The deep winter outflow at KSK1 is concentrated in a 80 m thick layer centered at about 200 m depth, whereas the deep outflow at FOC1 covers most of the water column from 150 m to the bottom. Because not all the outflow deep water from the inner basin (FOC1) can make it over the sill to the outer basin (KSK1), and the water that does make it is not dense enough to sink to the bottom of the outer basin, an elevated and thinner outflow at KSK1 (centered at 200 m) is present. Similar flow features have also been observed in the Strait of Georgia by Masson and Cummins (2007). The deeper summer inflow at KSK1 is also centered at about 200 m depth

whereas at FOC1 the inflow covers the lower layer from 250 m to the bottom and is bottom intensified (in 2013-14 it was more vertically uniform over the lower 100 m). These differences suggest that the 200 m deep sill between KSK1 and FOC1 has the biggest impact on the bottom inflow water in the inner basin (renewal season), and on the outflow at the sill depth in the outer basin (winter).

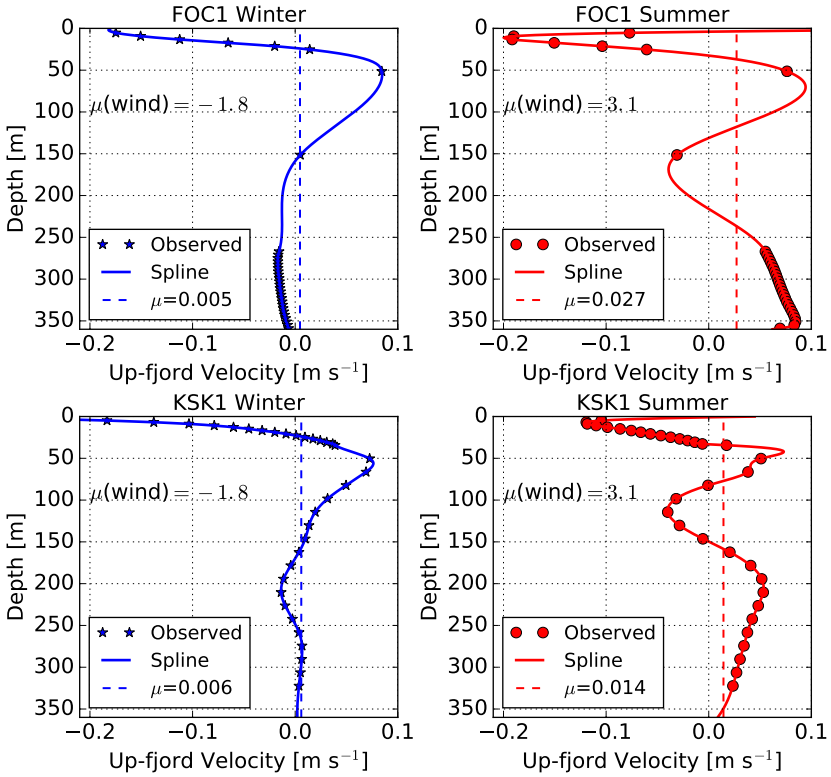

Figure 2.5: Seasonal mean along-channel velocity at Station FOC1 (53.736° N, 129.030° W) and KSK1 (53.480° N, 129.209° W) in Douglas Channel. The observed mean velocities are averaged after applying the low-pass filters, the solid lines are the cubic splines fitted to the observed mean velocities, and the dashed lines (μ values) are the vertically averaged velocity from the surface (0 m) to the bottom (360 m) computed from the spline fits. μ(wind) is the averaged along-channel wind velocity during each time period in the channel.

2.3.3 Deep water renewal

In fjords, yearly renewals are usually associated with the appearance of the dense water at the mouth of the fjord (Syvitski et al., 1987). In early summer (May to June), dense water becomes available at HEC1 (Figure 2.6) and starts to fill both the inner and the outer basins. From May/June to mid-September, there is a continuous renewal in the outer basin in the layer extending from 150 m to the bottom, 'lifting' the overlaying layers up. As shown in Figure 2.5, the zero velocity crossing for the bottom of the second layer at KSK1 is displaced upward from 150 m in winter to 80 m in summer.

In contrast to other well studied shallow-silled inlets (e.g. Knight Inlet by Baker and Pond (1995)), the renewal water from the shelf is dense enough to reach the bottom of both basins in Douglas Channel, but the strongest velocity is at about 200 m depth, below the sill at the shelf at about 140 m depth, for the outer basin, and likely deeper towards the bottom for the inner basin. Furthermore, the inflow does not seem to be interrupted by either the spring or the neap tide (Figure 2.6) — the mixing at the inner sill is not strong enough to inhibit the renewal flow even during spring tide, and the kinetic energy that is provided by the relatively weak neap tide is enough to lift the dense water over the sill. In fact, the velocity at depth at FOC1 is in the up-fjord direction even during some relatively strong ebb tides (approximately from June 20 to July 4, 2014 at FOC1, Figure 2.6).

There are a few interesting points in the salinity timeseries (Figure 2e, Figure 6, Figure A.2 and A.3) that influence the estimate of the time it takes for the renewal water to go from KSK1 to FOC1. It is clear that the deep salinity at KSK1 starts to increase on June 4, 2014 and it starts to increase at FOC1 on June 14, 11 days later. However the salinity at KSK1 (322 m) starts lower than at FOC1 (316 m and 352 m), and does not exceed the salinity at FOC1 until about June 11. The salinity at FOC1 starts to increase on June 14, 3 days later, simultaneously at 316 m and at 322 m depths. In 2015, we only have the salinity measurement at KSK1 at 362 m, which is 40 m deeper than the one in 2014, and the salinity is always higher than the ones at FOC1 (297 m and 354 m). The bottom salinity at KSK1 at 362 m depth started to increase on May 1, 2015. Three days later, the salinity at 297 m starts to increase; the salinity at FOC1's deeper depth (354 m) starts to increase 10 days later on May 11. The two deep salinity timeseries at FOC1 then increase at the same rate. In addition, there is a curious sudden increase followed by a decrease in salinity at

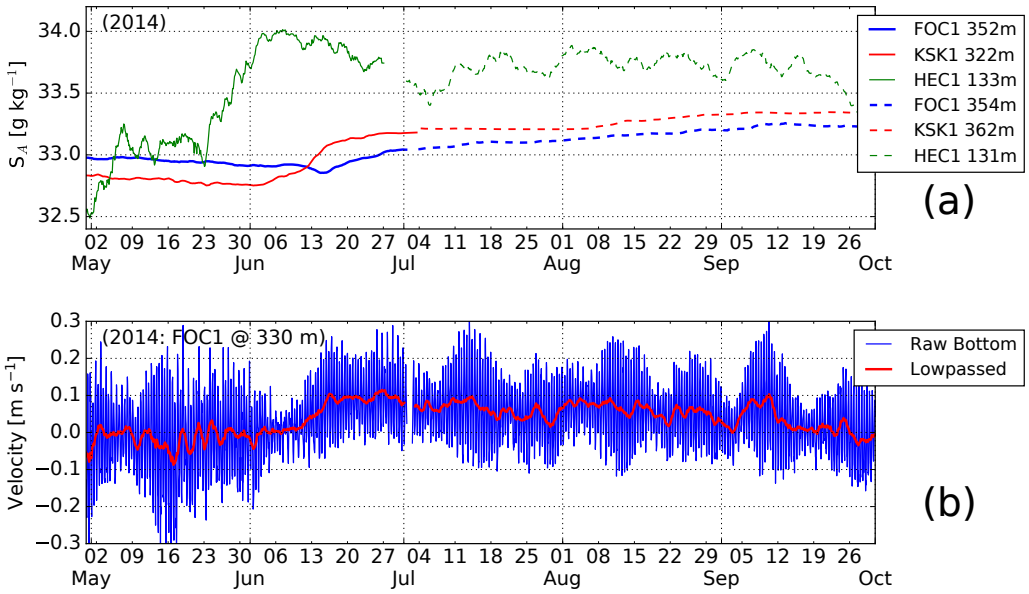

Figure 2.6: (a) Absolute Salinity at the bottom of the three stations during the renewal in 2014. (b) Bottom along-channel velocities (raw and low-passed) at FOC1 during the renewal in 2014. The bottom current meter at KSK1 failed on May 10, 2014, so there are no bottom current observations in the outer basin that captured this summer renewal process. The salinity timeseries during renewal periods are also included in Figure A.2 and A.3 in the Supporting Material.

FOC1 at 352 m depth right before the renewal that is not present in 2015, which we cannot explain at this point.

The picture we draw is as follows. When the high density water appears at depth at HEC1, this water starts to flow over the sill at the shelf and fill the outer basin of Douglas Channel. This water then needs to fill the basin from the bottom up until dense water is able to get over the inner sill. Once this water starts to flow over the sill it continues to do so until the dense water disappears from HEC1 (late September). Our observations and analysis do not allow us to determine whether the water crosses the inner sill at all phases of the tide, but the observations at FOC1 suggest that the renewal flows are not interrupted by spring or neap tides. In fact, from Figure 2.6) we see that the renewal may start at neap tide when the tidal mixing is low, which allows dense water to enter the basins without being mixed too much with the less dense water. The question of how long it takes for the renewal water to get from KSK1 to FOC1 does not have a simple answer because of the need for the renewal water to fill the outer basin. In 2015 it is clear that the renewal water appears at FOC1 on May 4 – 5. However it is not clear whether to start the clock when the renewal water arrives at KSK1 (297 m) and the salinity starts to increase or when the water at KSK1 (297 m) is dense enough to reach the bottom at FOC1. The range of time estimates is 3 – 10 days which gives a range of speeds of 3 – 13 cm s^{-1}.

Given the above evidence, we argue that the dense water flows over the inner sill into the inner basin is driven by density difference between the deep water in the outer and the inner basins. Benjamin (1968) derived the solution for the gravity current speed for steady density currents:

$$c = \left[\frac{(H-d)(2H-d)}{H(H+d)}\right]^{1/2} \sqrt{g'd} \tag{2.1}$$

where H is the water depth (360 m), d is the bottom layer thickness (130 m for FOC1), g' is the reduced gravity ($g\Delta\rho/\rho$), and $\Delta\rho$ is the density difference between the ambient density and the intrusion density. To estimate velocity c, we assume the ambient density is the potential density at FOC1 at 316 m, with a 2-day time lag (estimated transit time from the sill to FOC1), and the intrusion density is the potential density at KSK1 at 322 m less 0.12 kg m^{-3}, which is approximately the density difference between the sill depth (200 m) and the observed depth according to the CTD data from July 2014 cruise. The estimated intrusion velocity is then

$c = 0.05$ to 0.19 m s^{-1} (from June 15 to June 28 2014 estimates), which is consistent with the observed bottom velocity (0.10 m s^{-1}, from June 15 to June 28 2014 in Figure 2.6, noting the rapidly increasing velocities before June 15). These estimates are also consistent previous estimate of 3 – 13 cm s^{-1} from the salinity timeseries. This estimation is sensitive to (1) the estimate of the bottom layer thickness at FOC1, which relied on the spline fit between 150 m and 260 m because the lack of data; (2) and the estimated intrusion density does not account for the mixing at the sill and entrainment between KSK1 and FOC1. Nevertheless, the consistency between various speed estimates support the idea that the renewal water that cascades the inner sill takes the form of gravity currents at the bottom of the inner basin. Similar gravity current intrusions have also been reported in Puget Sound (Geyer and Cannon, 1982), the Strait of Georgia (Masson, 2002), and Nootka Sound for 2016 (Michael Foreman, personal communication).

One usually expects a gravity current to arrive with a sharp front, and this feature has been seen in some fjords. For example, in the basin of Gullmar Fjord, Sweden (Arneborg and Erlandsson, 2004), the dense water filled the bottom 36 meters in less than 24 hours in April 2002. For the Douglas Channel system, the rapid increase of the salinity takes about 10 days for the deep water at FOC1 and KSK1. This is consistent with the deep salinity signal at HEC1. We speculate that the smooth increase in the salinity at KSK1 is a reason that a sharp front is not observed at FOC1.

Although beyond the scope of this paper, we also note that the salinity difference between HEC1 and KSK1 is due to the mixing that occurs between the two. The outer sill at the mouth of the Douglas Channel is not a clearly defined sill, but an about 26 – 30 km wide extended region that connects with the continental shelf (at about 140 m depth). The mixing before the water enters to Douglas Channel could greatly reduce the density of this dense water, whose density gradually increases. This intense mixing at the mouth is supported by the density difference (0.5 - 1.0 kg m^{-3}) between the HEC1 bottom water and the basin water densities. This type of gradual salinity change (5 – 7 days) was observed in Puget Sound, which has a 30 km extended sill at the entrance (Geyer and Cannon, 1982).

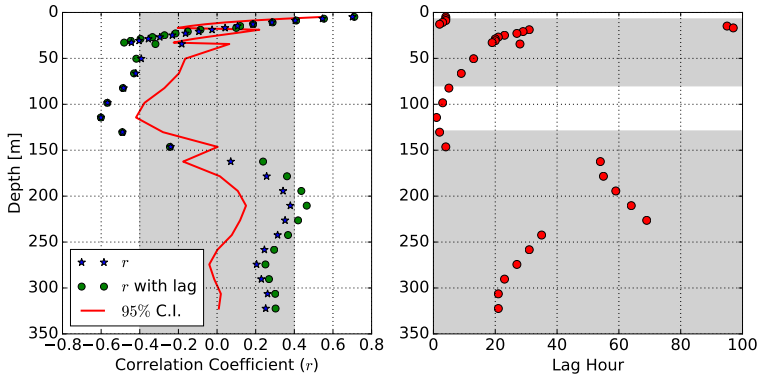

Figure 2.7: Left panel: correlation coefficients r (blue stars) between the along-channel wind velocity and the along-channel current velocities measured at KSK1. Right panel: The time lags for the along-channel wind velocity and the along-channel current velocity to reach the maximum correlation (the green circles in the left panel are the maximum correlation coefficients given the corresponding time lags). The 95% confidence limit for r is labeled in the red line (i.e. when the absolute value of the red line is larger than 0, it is considered as statistically significant but not necessarily practically significant). The regions where r is within $[-0.4, 0.4]$ (i.e. $r^2 < 0.16$) are considered practically not significant for this study and shaded in gray. The time period chosen for this analysis is from Jan 13 to Jul 25, 2015, where we have continuous concurrent current velocity and wind observations.

2.4 Wind-Driven Response

Surface wind driven currents in fjords have been reported in numerous studies. Wind stress is able to enhance or reverse the surface estuarine outflow (e.g. Matsuura and Cannon (1997) in Puget Sound; Baker and Pond (1995) in Knight Inlet; Castillo et al. (2012) in Reloncavi Fjord), and counter-currents at depth were also observed in these fjords [e.g. at around 100 m in Puget Sound by Matsuura and Cannon (1997)]. Next we explore the relationship between the low-passed wind and current velocities in Douglas Channel.

2.4.1 Wind-driven Currents

Simple linear regression analysis between the low-passed along-channel wind velocity and the along-channel current velocity at 5 m at FOC1 shows that the surface current velocity is highly correlated with the wind velocity (current velocity lags the wind by

5 ± 20 hours, $r^2 = 0.63$):

$$u_{F@5m} = 0.027W - 0.14 \text{ m s}^{-1}, \tag{2.2}$$

where W is the up-fjord wind velocity during this time period (Jan 13 to Jul 25, 2015). This simple regression clearly distinguishes the estuarine outflow and the wind-driven currents. During this time period, the estuarine circulation contributes to an average of 0.14 m s^{-1} outflow, and the mean wind ($\overline{W} = 0.88$ m s^{-1} up-fjord) contributes to an average of 0.024 m s^{-1} inflow (0.027×0.88 m s^{-1}), so on average, the net outflow is 0.12 m s^{-1}. For this period, the wind variation can explain 63% of the velocity variation, and the amplitude of the current velocity variation is about 2.7% of the wind velocity variation. This surface current and wind regression coefficient is relatively robust during other time periods (between 2.2% and 3.7%, Table A.1 in the Supporting Information) with some exceptions. These results are roughly consistent with Weber (1983), who showed analytically that the total surface currents should be between 3.1% and 3.4% of the wind speed. The uncertainty is calculated at the 95% significance level, and the effective degrees of freedom are computed as $N/67$, where N is the number of the hourly samples and the energy amplitude drops to half at T = 67 h after the Godin filter.

To provide information about the very near surface currents for pollutant spill applications, we use the regression relationships for the upper three bins for FOC1 and KSK1 to extrapolate the relationships to the surface:

$$u_{F@0m} = 0.049W - 0.14 \text{ m s}^{-1}; \tag{2.3}$$

$$u_{K@0m} = 0.052W - 0.23 \text{ m s}^{-1}. \tag{2.4}$$

The density driven components are different for these two stations, but the wind driven components are roughly the same, around 5% of the wind velocity. These relationships will be tested later in future studies using drifter data collected during this observing program.

The above relations between the wind velocity and the current velocities can be used as a proxy to estimate the current velocities when direct measurements are not available, assuming that the relations are stable over time. Our analyses show reasonably consistent correlations between the wind and the surface current velocities during all available time periods (Table A.1 in Supporting Information). The root-

mean-square deviation (rmsd) can be used as a measure of the difference between the estimator and the actual observations here. The prediction results are reasonable for the surface current velocity. The rms of the observed surface current velocity during this time period (Jan 13 to Jul 25, 2015) is 0.18 m s^{-1}, and the rmsd of the predicted surface (5 m) current velocity by Equation 2.2 during this time period is 0.09 m s^{-1}. During all available time periods listed in Table A.1, the rmsd of the predicted velocities are generally around 0.1 m s^{-1}. Overall, it is relatively robust to use the wind to estimate the sub-tidal surface current velocities, and the estimated velocities are generally 10% smaller than the observed velocities.

2.4.2 Surface Slope Response

We next analyze the wind response in terms of the sea surface slope in the fjord. In a long narrow channel the sea surface is set up in response to wind-forcing, which allows us to estimate the thickness of the layer directly influenced by the wind. Assuming the vertical mixing coefficient in the wind-influenced layer is constant, the steady-state vertically integrated momentum balance for the wind-influenced layer, h_1, that is directly subject to wind influence is (Farmer, 1976):

$$\tau_w - \tau_{h_1} = h_1 \rho_1 g \frac{\partial \eta_1}{\partial x} \tag{2.5}$$

with $\tau_w = \rho_{air} C_d W|W|$ and $\eta_1 = \eta_k - \eta_h$, where τ_w is the surface stress, C_d is the surface drag coefficient (1.2×10^{-3}, Large and Pond (1981)), $\rho_{air} = 1.2$ kg m^{-3} is the air density, $\rho_1 = 1010$ kg m^{-3} is the averaged density of the wind-influenced layer, g is the gravitational acceleration, W is the up-fjord wind velocity, x is the along-fjord axis, τ_{h_1} is the stress at the base of the wind-influenced layer, and η_k and η_h are the sea surface elevations observed at Kitimat and Hartley Bay, respectively (Figure 1). Kitimat and Hartley Bay are 80 km apart, so the barotropic pressure gradient term ($\partial \eta_1 / \partial x$) can be approximated as $(\eta_k - \eta_h)/80$ km.

The steady state approximation is reasonable as the gravity wave speed in 300 m of water is 54 m s^{-1} and signals will propagate from one location to the other in less than 30 minutes. This is fast compared to the subtidal frequencies in the filtered time series.

Now we decompose Equation 2.5 into the time-constant and time-varying components, denoting them as $(\bar{\cdot})$ and $(\tilde{\cdot})$, respectively. Under the assumptions that the

wind-influenced layer thickness h_1 is constant (i.e. $\tilde{h}_1 << \overline{h}_1$ so $h_1 \approx \overline{h}_1$), and $\tilde{\tau}_{h_1}$ is independent of h_1 (Figure 5 shows approximate linear stress in the upper 50 m depth), h_1 can be determined from the slope of the linear regression relationship between the time-varying components of the wind stress and the sea surface slope:

$$\tilde{\tau}_w \sim h_1 \rho_1 g \frac{\partial \tilde{\eta}_1}{\partial x}. \tag{2.6}$$

and the mean bottom shear stress of the wind-influenced layer can then be estimated through the time-constant balance: $\overline{\tau}_{h_1} = \overline{\tau}_w - h_1 \rho_1 g \frac{\partial \overline{\eta}_1}{\partial x}$.

For the period Jan 13 to Jul 25, 2015, the correlation between the wind stress and the barotropic pressure gradient is large and is statistically significantly different from 0 ($r^2 = 0.74$ where the pressure gradient lags the wind by 5 ± 9 hours). The r^2 for the other time periods ranged from 0.72 to 0.77 (see Table A.2 in the Supporting Information). The maximum lagged correlations between the wind stress and the individual sea level time series are much smaller and not significant ($r^2 = 0.17$ and 0.22 at Kitimat and Hartley Bay respectively). The strong correlation between these two terms indicates that more than 70% of the variation in the barotropic pressure gradient variation can be explained by the wind variation, which also indicates that the contribution of the wind stress to the $\tilde{\tau}_{h_1}$ is small because $\tilde{\tau}_{h_1}$ is determined by the background time-varying density driven flow. Nonetheless, we only focus on the wind stress and the surface pressure gradient relationship here.

From the regression we get $h_1 = 8.0 \pm 1.1$ m. The estimations for h_1 are between 8 and 12 for all time periods that we have available (Table A.2 in the Supporting Information). This 8 to 12 m wind-influenced layer thickness is consistent with the rapid decrease with depth of the correlation coefficient between the wind and currents as evident in in Figure 2.7. It is also consistent with the approximately 10 m thickness of the surface water seen in the salinity profiles (Figure 2.9).

2.4.3 Barotropic and Baroclinic Response

The analysis so far has focussed on the surface response to the wind. However when an up- (down-) fjord wind increases (decreases) sea level at the end of the fjord this will depress (raise) the isopycnals. These changes in isopycnal depth can cause a baroclinic response in the density field, which propagates down fjord and affects the currents (Farmer, 1976; Matsuura and Cannon, 1997).

Figure 2.7 shows the correlations between the wind and the currents through the water column at KSK1 for the period Jan 13 to Jul 25, 2015. The correlation coefficient r drops rapidly from 0.7 near the surface to zero at about 20 to 50 m; it has a negative maximum of -0.6 at about 115 m depth; r crosses zero and becomes a small positive number below 150 m. The negative correlation between the wind and the current in the 100 m depth band was also reported in other inlets. Matsuura and Cannon (1997) found the negative maximum correlation occurred at 100-120 m depth in Puget Sound, and a weak wind-induced velocity response was reported near the bottom (below 100 m) in Knight Inlet (Baker and Pond, 1995).

The lagged correlation between the fluctuations in the wind and the near-surface potential density difference between KSK (at 15 m) and FOC (at 12 m) has $r^2 = 0.45 \pm 0.19$ with lag $= 16 \pm 22$ hours (for the period Jan 13 to Jul 25, 2015 at the 95% significance level; see Table A.3 for results during other time periods), which suggests the potential for a baroclinic response. The first mode baroclinic wave has a speed of 0.8 m s^{-1}, so the travel time from Kitimat to KSK is about 24 hours, which is consistent with the observed lag.

The counter-wind current velocity at 115 m depth is in the same direction as the barotropic pressure gradient, indicating the importance of the barotropic response. Given the potential baroclinic response, the dynamics require that we consider both. The linearized momentum equation in the along-channel direction at depth z below the direct wind-driven layer, with forcing terms being the barotropic and baroclinic pressure gradients is:

$$\frac{\partial u}{\partial t}|_z = -g\frac{\partial \eta_1}{\partial x} - \frac{g}{\rho_0}\int_z^\eta \frac{\partial \tilde{\rho}}{\partial x} dz \tag{2.7}$$

where $\tilde{\rho}$ is the perturbation component of the density, and ρ_0 is a reference density. The first term on the r.h.s. is the barotropic pressure gradient at depth z and the second term is the baroclinic pressure gradient. While it is not possible to directly measure the baroclinic pressure gradient given what we have, we will assume that the density gradient anomalies at 12 m at FOC1 and at 15 m at KSK1 gives a reasonable averaged values for the upper 30 - 50 m for the baroclinic gradient term. Then we can estimate at which depth these two terms balance each other by setting the l.h.s of Equation (2.7) to 0, and perform a linear regression to find z. The linear fit (Figure 2.8) results show these two pressure gradient terms balance each other at 34 ± 6 m.

The barotropic and baroclinic pressure gradient terms compete with each other

at all depths. However, because the barotropic pressure gradient does not vary with depth, we hypothesize that the rich vertical profile of the correlation coefficient between the velocity and the wind (Figure 2.7) is ultimately the result of the vertical profile of the baroclinic pressure gradient term.

Below the direct wind-influence layer (top 10 m or so) where the wind stress dominants the velocity, the baroclinic term starts to become important, and is comparable with the barotropic pressure gradient at 30 – 40 m. This is consistent with the insignificant correlation coefficients between the wind and the current velocities at 20 to 40 m depth, where the wind induced barotropic and baroclinic forcings counter balance each other.

Between 50 m and 150 m depths, the current velocity is in the direction of the barotropic pressure gradient (counter wind-direction), which suggests that the adjusted isopycnals below 34 m depth cause the baroclinic term to be insignificant at mid-depth or significant but in the same direction as the barotropic pressure gradient. Therefore, the currents in the 100 m depth band seem to be driven by the barotropic pressure gradient. As it goes deeper than 150 m, the baroclinic pressure gradient opposes the barotropic pressure gradient again, and reaches its peak at 200 m depth. Given our limited observational data, we cannot say for uncertain at this point whether the baroclinic pressure gradient agrees with the correlation vertical profile, but this will be investigated more carefully with numerical experiments along with analytical solutions in our future studies.

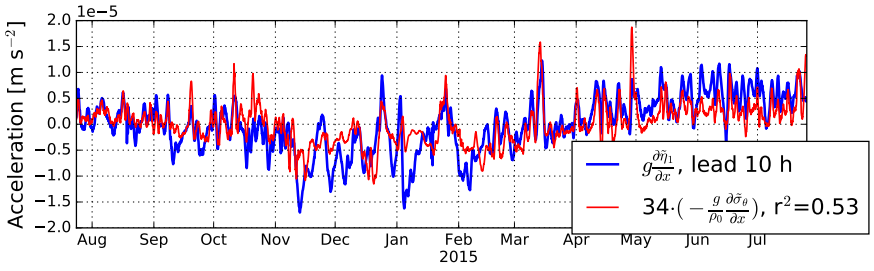

Figure 2.8: Time series of the barotropic ($g\frac{\partial\eta_1}{\partial x}$, blue) and baroclinic ($-h_1\frac{g}{\rho_0}\frac{\partial\bar{\sigma}_\theta}{\partial x}$, red) forcing terms. These two time series are correlated ($r = 0.73 \pm 0.07$), and the fitted coefficient of the linear fit is 34 ± 6 m corresponds to the depth at which these two forcing terms balance each other. The peak correlation occurs when the elevation difference lags the density difference by 10 ± 18 hours (95%).

2.5 Volume Budget and the Surface Outflowing Layer

2.5.1 Volume Budget

The velocity profiles shown in Figure 2.5 provides us a way to look at the volume transport of each velocity 'layer'. Here, we follow examples in other fjord studies (e.g. (Baker and Pond, 1995)) and define the 'layers' as the inflowing and the outflowing water masses. The volume transport of each layer can then be calculated under these assumptions: the cross-sectional velocity and density variation is negligible; the velocity measured by the ADCPs and interpolated by the spline fit is a good representation of the overall along-channel flow; the cross-sectional width is parameterized as a function of depth instead of having uniform width at each depth to minimize the error that could be introduced by the bathymetry (details are given in Table 2.2).

Under these assumptions, the volume transport for each 'layer' is then calculated at FOC1 and KSK1 for both the summer renewal and the winter seasons (Table 2.2). Layer 1 and 2 represent the outflowing and the inflowing layers in classic estuarine circulation. The surface outflow (Layer 1) has similar volume transport at both moorings in both summer and winter (around 10×10^3 m^3 s^{-1}). The summer outflowing layer is 10 m thicker than the winter outflowing layer (30 m compared to 20 m). Layer 2 has similar volume transport (around 20×10^3 m^3 s^{-1}) and thickness between the moorings in winter. In summer, the transport of Layer 2 at KSK1 is reduced by a factor of about two (around 10×10^3 m^3 s^{-1}), whereas Layer 2 at FOC1 does not show this difference. Layer 0 represents the inflowing layer above Layer 1. A relatively small transport layer is present in summer at both stations (in the order of 1×10^3 m^3 s^{-1}), which is a consequence of the summer up-fjord wind.

At KSK1 the data density of the velocity profile is sufficient to constrain the spline fit. However this is not true at FOC1 where between 50 and 250 m there are only data points at 50 m and 150 m. The spline profile gives very similar layer thicknesses at KSK1 and FOC1 in the winter but very different ones in the summer. We note that in the upper 200 m, the spline fit at KSK1 is reasonably consistent with the data points at FOC1 for both winter and summer. In winter the measurements at 150 m at FOC1 happened to define the location of the bottom of layer 2 which was consistent with that observed at KSK1. However in the summer the data at FOC1 does not define the velocity profile zero crossings and the spline profiles in the upper

200 m at FOC1 and KSK1 are very different.

There is a strong argument that the transport in Layer 1 and 2 (the two estuarine flow layers) should be reasonably continuous between FOC1 and KSK1 since there are no substantial side channels to act as sources or sinks. In addition, the fact that the winter profiles are very similar down to 200 m indicates that the sill at 200 m depth between the two moorings is not a major source of mixing that alters the thicknesses of the upper 2 layers.

If Douglas Channel did not have any side channels, the 'net flux' term in the volume budget would be a small negative number representing the fresh water moving down the fjord; however, in Table 2.2 the 'net flux' term is comparable in size to the layer transports and directed up-fjord (positive). Cross-channel variation is often invoked to explain volume transport discrepancies when studying circulation in fjords and inlets (Halverson et al., 2013), because the along-channel flow can be under-resolved given the limited measurement across the channel. It is even considered as a significant contributor in some 'narrow' channels. For example, Baker and Pond (1995) concluded that the cross-channel circulation might be more important than anticipated even in Knight Inlet, even though it is a 'narrow' channel. However, the complexity of the channel network in the Kitimat region gives us another possible explanation for the 'net flux'.

Using simple numerical models, Webster (1980b) suggested that the interpretation of the flows in Douglas Channel in terms of estuarine flow requires that we consider Gardner Canal and Verney Passage and account for the fresh water flux out of the system via Verney Passage (Figure 1). Following this postulation, assuming Layer 2 in Douglas Channel provides all of the required salt flux and the salinity of hypothesized outflowing surface layer in Verney Passage is comparable with the outflowing surface layer in Douglas Channel, we can use the standard estuarine flow equations (Knudsen (1900) as cited by Freeland and Farmer (1980)) to estimate the fresh water flux to see if it gives us a reasonable range: $Q_f = Q_1(S_2 - S_1)/S_2 = Q_1(1 - S_1/S_2)$, where Q_1 is the volume flux out at the surface, S_1 is the average salinity in the outflowing surface layer and S_2 is the average of the deep salinities. Taking $S_2 = 32$ g kg^{-1} (the salinity at 100 m in Figure 2.9) and $S_1 = 29$ g kg^{-1} or 30 g kg^{-1} (the salinity at 10 m at the mouth Figure 2.9), this yields freshwater flux estimates between $[1.2, 1.9] \times 10^3$ m^3 s^{-1}, which matches Morrison et al. (2012) at the lower bound.

Therefore the hypothesis that at least some of the net flux terms in Table 2.2 represent the volume flux required to supply the surface outflow at Verney Passage

is not unreasonable. This hypothesis also reduces the need for horizontal or vertical recirculation patterns to balance the volume fluxes at KSK1 and FOC1. Making sense of this will require a more complete regional analysis of the temperature and salinity properties, and a numerical circulation model that includes all channels and possible strong mixing at channel junction points.

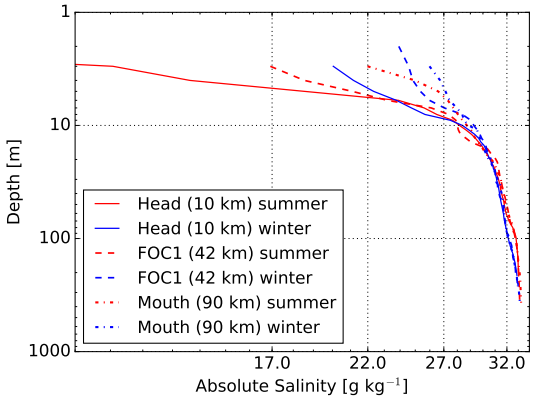

Figure 2.9: Absolute Salinity at the head (solid lines), FOC1 (dashed lines) and at the mouth (dash-dotted lines) of Douglas Channel. The summer data is the average of the July 2013 and July 2014 cruise CTDs, and the winter data is the average of April 2014 and October 2014 cruise CTDs. The vertically averaged Absolute Salinities (in g kg^{-1}) for layers 1 and 2 at the head are: S_1(summer)= 28.41, S_2 (summer)= 31.94; S_1(winter)= 27.75, S_2 (winter)= 32.02; at FOC1: S_1(summer)= 29.00, S_2(summer)= 32.09; S_1(winter)= 28.80, S_2 (winter)= 32.05; at the mouth: S_1(summer)= 30.02, S_2(summer)= 32.00; S_1(winter)= 29.02, S_2 (winter)= 32.03.

2.5.2 Surface Outflowing Layer Thickness

The forgoing analysis suggests that it is the freshwater discharge and the salinity distribution that control the surface transport. But what controls the outflowing surface layer thickness in this system, and in particular, why is the surface layer 10 m thicker in summer than that in winter (Table 2.2)?

The potential density profiles show that the brackish water is mostly in the top 5 – 7 m, and the depth of maximum negative curvature in the salinity (Figure 2.9) and the potential density (Figure A.1) profiles is generally around 6 – 10 m, which is similar to what Webster (1980b) obtained from the cruise CTD profiles (10 - 14

m). However, the velocity ADCP shows that the surface outflow layer is consistently around 30 m thick in summer, and highly variable in winter (Figure 2.4).

An estimation of the surface freshened layer thickness can be made by examining the balance between the wind stress and the density driven flow by the Wedderburn number (Wb) (Farmer and Freeland, 1983; Geyer, 1997; Inall et al., 2015),

$$Wb = \frac{\tau_w L}{\Delta\rho g H_1^2} \tag{2.8}$$

where $\tau_w = \rho_{air} C_d W|W|$ is the wind stress, L is the length of the fjord (80 km in Douglas Channel), and $\Delta\rho$ is the upper layer density difference along the fjord axis. Because we know the wind driven influence at the surface is comparable with the density driven force (e.g. in Figure 2.5 the wind is able to reverse the surface flow in summer), we set $Wb = 1$ to estimate the thickness of the outflowing surface layer (H_1):

$$H_1 = \sqrt{\frac{\tau_w L}{\Delta\rho g}}. \tag{2.9}$$

In Douglas Channel, $\Delta\rho = 1.6$ kg m^{-3} in summer between the head and the mouth, and $\Delta\rho = 1.0$ kg m^{-3} in winter; the values are obtained by averaging the winter (April and October) and the summer (two Julys) the CTD profiles. The predominantly up-inlet wind in summer at 3.1 m s^{-1} on average gives $H_1 = 8$ m, and the predominantly down-inlet wind in winter at 1.8 m s^{-1} on average gives $H_1 = 6$ m. The surface density is averaged over the approximate first velocity layer (35 m in summer and 25 m in winter). If we only consider the surface 10 m for the surface density, the estimated values are $H_1 = 6$ m in summer ($\Delta\rho = 4.0$ kg m^{-3}) and $H_1 = 4$ m in winter ($\Delta\rho = 2.6$ kg m^{-3}). These estimates are 1/5 to 1/3 of the measured thicknesses (recall Table 2: about 32 m in summer and 22 m in winter), indicating that $Wb = 1$ is an overestimation so the density-driven flow dominants over the wind-driven flow at the surface on average.

Up- and down-fjord winds can have different effects in addition to the undirectional estimates above. An up-inlet wind tends to thicken the surface outflowing layer at the head of an estuary and to retard the surface outflow, whereas a down-inlet wind tends to blow the outflowing surface layer water out and enhance the estuarine exchange (Farmer and Osborn, 1976; Farmer, 1976; Inall et al., 2015).

In Douglas Channel the surface outflowing layer thickness can be much different than the mean conditions. When the mean wind direction changes from up-fjord to down-fjord (e.g. mid-September to late-October in 2014, Figure 2), the surface outflow layer thickness is generally less than 10 m (e.g. Figure 2.4, mid-September to late-October in 2014), which agrees with the stratification layer thickness. During high wind stress events, the wind stress influence dominates the density-driven flow in the outflowing surface layer ($W_b = [12, 1]$ given $H_1 = [10, 50]$ m, and $W = 15$ m s^{-1}). The peak wind in Douglas Channel is mostly down-fjord, so we see the deepened (to 50 - 70 m) surface enhanced outflowing surface layer that is driven by the wind stress (early December 2014 and early January 2015 in Figure 2.4), and a compensating inflow layer immediately underneath it.

The near surface stratification in Douglas Channel will inhibit convectively generated turbulence in the outflowing surface layer (Farmer and Freeland, 1983), but other mixing processes, such as wind mixing, can generate turbulence and entrain the underlying water into the surface outflowing layer (Stigebrandt, 2012). Now we explore whether the outflowing surface layer is controlled by the wind mixing from dynamics.

The mechanistic model that Stigebrandt (1981) presented for a stationary surface layer suggested that, in deep stratified fjords, the thickness of the surface outflow layer is controlled by three factors: the wind mixing, the freshwater discharge, and the mixing at a hydraulic control point. In Douglas Channel, there is no obvious location along the channel that provides a horizontal or vertical constriction acting like a hydraulic control point. So the hydraulic effects are not expected to be significant. This allows us to focus on the wind influence component (Stigebrandt, 1981, 2012):

$$H_1(W, Q_f) = a \cdot \frac{W^3}{Q_f}, \tag{2.10}$$

where W is the wind speed, Q_f is the freshwater discharge, and $a = \frac{C_e A_f}{2M}$, with $C_e = 2.5 \cdot 10^{-9}$ being an empirical constant that incorporates the drag coefficient on the air-sea interface, A_f being the area subject to wind mixing, and $M = g\beta S_2$ (g is the gravitational acceleration, β is the salinity contraction coefficient: 0.0008 (g/kg)$^{-1}$, and S_2 is the salinity of the second layer).

The averaged layer thickness estimate (from Equation 2.10) is only 1.4 m in winter, and even smaller (0.6 m) in summer. These estimates are one order of magnitude smaller than those calculated from the velocity profile. Furthermore, even if we

expand the wind-influenced surface area to include Gardner Canal and the connecting passages (i.e. increase A_f from 380 km^2 to 811 km^2), the estimated thickness will still be one order of magnitude smaller and the greater thickness in summer will still not be explained. The estimated wind component of the first layer thickness is able to capture the sudden peaks shown in winter (Figure 3 and 4) of up to 28 m, but still 50% smaller than observed in Figure 2.4 in December and early January.

Other mixing processes may be more or equally important than wind mixing in determining the surface brackish water thickness. Examples include side-wall mixing, internal waves, horizontal entrainment at the intersections of two or more channels, and possible mixing from the internal lee wave formed on the downstream side of the sill during both flood and ebb tides over the 30 m deep sill in Verney Passage (Webster, 1980b). However, we do not have any evidence to pursue this.

Therefore, the outflow layer thickness is greatly influenced by the wind energy input to the surface water through processes captured by the Wedderburn Number. These processes are able to explain the thicker velocity outflow layer as compared to the pycnocline, the relatively constant thickness in summer seasons, the much thinner layer during wind direction transition periods, and the much deepened outflow layer (50 - 70 m) influenced by wind during winter storm events. This hypothesis will be further investigated using numerical models in future research.

2.6 Discussion and Summary

2.6.1 Seasonal Circulation

The dominant feature of the seasonal circulation in Douglas Channel is a 4 layer circulation in summer (May/June to September) and a 3 layer circulation in the winter (October to May/June). In both seasons the upper 2 layers are estuarine-like with a relatively fresh surface outflow layer and a saltier inflow layer immediately below. The mean surface outflow is approximately the same in summer and winter (10×10^3 m^3 s^{-1}) at both KSK1 and FOC1. In summer the volume transport in the second (inflow) layer is approximately in balance with the surface outflow (as expected for estuarine flow) at KSK1, however in winter the transport in the second layer is estimated to be 20×10^3 m^3 s^{-1} (at both KSK1 and FOC1), about twice of what is required to balance the surface outflow.

The summer Layer 2 thickness and transport at FOC1 are questionable because

of the vertical resolution, where between 50 m and 250 m there are only velocity data points at 50 m and 150 m. Since there are no substantial side channels between FOC1 and KSK1 to act as sources or sinks and the sill between them is much deeper than the bottom of the second layer, we expect that the transport of the surface two layers at the moorings to be in a reasonable agreement. At KSK1 the vertical resolution of the velocity profile is sufficient to constrain the spline fit (Figure 2.5). In winter the measurements at 150 m at FOC1 happened to define the location of the bottom of layer 2 which was consistent with that observed at KSK1. However in summer the data at FOC1 does not constrain the velocity profile zero crossings, so we face a more significant spatial aliasing problem here. Therefore, the spline fit and the velocity profile at FOC1 in summer could be more misleading than informative.

The mean surface outflow layer thickness is about 30 m thick in summer (at KSK1) and only about 20 m thick in winter. The scaling analysis based on the Wedderburn number (Wb) indicates the thicker surface outflow layer in summer is due to the larger magnitude of the mean wind. The second layer (inflow) also shows substantial differences between seasons; at KSK1 it extends from about 30-80 m depth in summer, whereas it extends from about 20 m to 170 m in winter. This thicker winter inflow layer, which delivers shelf water into Douglas Channel, was inferred by Macdonald (1983) from the water properties.

In summer, below the surface estuarine circulation, there is a season long renewal event with inflow at the bottom and an outflow above that. This deep inflow is caused by the appearance of dense water at depth at the entrance to the fjord system which cascades through the system until it disappears from the entrance, at the speed of 0.1 – 0.2 m s^{-1}, which is consistent with gravity currents.. The timing of the dense water appears to be related to the regional transition on the British Columbia coast from a downwelling regime to upwelling in May/June and then back to downwelling in September. In winter the deep flows in the inner basin (FOC1) are directed outwards over at least the bottom 60 m, whereas in the outer basin there is an outward flow centered at about 200 m (the inner sill depth).

The salinity of the deep water in the basins is dictated by the summer renewal signal. The deep salinity increases during renewal season, most rapidly in the first 10 days. It decreases gradually from the end of the renewal until it starts again next year, which indicates that diffusion and entrainment are the dominant mixing processes in the deep basin in winter. This gradual change in salinity between renewals was also observed in the deep waters between renewals in Strait of Georgia (LeBlond et al.,

1991; Masson, 2002) and Indian Arm (de Young and Pond, 1988).

The multi-layer circulation observed in Douglas Channel is not unique. A multi-layer structure with an estuarine circulation overlaying a complex deep water circulation was observed in the inner basin in spring 1988 and in the outer basin in summer 1989 (Baker and Pond, 1995). However, during the same time periods, the complex structure was not observed in the other basin (the outer basin in spring 1988 and the inner basin in summer 1989). The difference in layer structures between the basins is much larger than in Douglas Channel, which is attributed to stronger mixing over the shallow sills in Knight Inlet.

Deep water renewals are studied in many fjords, such as in Puget Sound (Geyer and Cannon, 1982), Indian Arm (de Young and Pond, 1988), Knight Inlet (Baker and Pond, 1995), and Strait of Georgia (Masson, 2002). They focused on how the spring/neap tidal cycle controls the renewal events once the dense water becomes available at the mouth. For example, in Knight Inlet, the enhanced mixing at the outer shallower sill (64 m) inhibits the intrusion, so the renewal signal is observed during the less energetic tides (neap tides); the deep-water renewal of the inner basin requires the more energetic spring tides for the dense water to go over the relatively deeper sill (68 m), and the return flow is observed both above and below the deep-water renewal layer. Our observations show that the renewal happens during the less energetic tides (neap tides), and this is probably due to the strong mixing in Hecate Strait where the bottom is rough. It is worthnoting that there are weather buoys (C46185, C46147 and C46207) that are located in Hecate Strait and adjacent shelf. While analyzing the winds is beyond the scope of this paper, the timing of the along-shelf changes from downwelling-favourable to upwelling-favourable should be studied in relation to the deep-water renewal in Douglas Channel.

The volume budget at the two moorings in Douglas Channel does not close under the assumption of uniform cross-channel velocities. In both seasons, at both moorings, there is an up-fjord directed transport equivalent in magnitude to the individual layer transports. We note that the channel is narrow (3-5 km) relative the internal Rossby radius (8 km) so we do not expect substantial cross-channel variations. However, there could be headland eddies and flow separations that make for more complicated cross-channel structure than we expect. In Knight Inlet (Baker and Pond, 1995), the net volume transport was estimated to be 1 order of magnitude larger than the mean freshwater input, and cross-channel variation was invoked to explain the imbalance.

In Douglas Channel, there is another potential explanation. As noted by Webster

(1980b) the head of the fjord system is not the Kitimat River at the head of Douglas Channel but the mouth of the Kitlope River at the head of Gardner Canal. As such, the interpretation of the volume and salt transports in Douglas Channel in terms of an estuarine flow conceptual model requires understanding the partitioning of the fresh water leaving Gardner Canal between the two potential outflow pathways: Verney Passage and Douglas Channel. As discussed by Webster (1980b) the partition of the fresh water likely depends on the spatial patterns of both the wind and the recent fresh water inputs as each will affect the pressure gradients along Devastation Channel which connects Gardner Canal, Verney Passage and Douglas Channel. This partitioning was not addressed by the mooring program discussed here and the origin of the volume imbalance observed in Douglas Channel remains an open question.

Douglas Channel is not isolated – it is closely connected to the neighbouring shelf region. In the winter the connection is through the upper inflow layer and in the summer it is through the deep renewal event. Therefore changes in the shelf water properties and biota should be expected to appear in Douglas Channel within a season or so. In addition, any changes in the timing of the regional transitions between upwelling and downwelling regimes should be expected to have an immediate impact on the timing of the renewal season.

2.6.2 Wind-driven Circulation

The wind-driven response was also investigated. The near-surface current velocity fluctuations and the surface elevation slope are dominated by the along-channel wind. The near-surface currents (4 – 5 m) at KSK and FOC are well correlated with the wind (r^2 ranges from 0.43 to 0.56) and the surface current fluctuations were about 2-4% of the wind speed depending on the period of the analysis: the rule of thumb is about 3% (Weber, 1983). From the relationship between the wind and the sealevel slope between Kitimat and Hartley Bay, we were able to estimate that the mean direct effect of the wind on the currents extended to 8 – 12 m into the water column, which is consistent with the vertical profile of the correlation between the wind and the currents. We suspect that the range in value of the coupling term between the wind and surface current is due to differences in the mixing and stratification during the analysis periods. As such the application of the relationship between the wind and the currents to estimate surface drift should respect the uncertainty in the value of the coupling coefficient.

The wind-induced changes in the surface slope in the channel should cause upwelling and downwelling at the head of the channel and result in isopycnal changes. Evidence was found for changes in near-surface (12-14 m) density gradients linked to the surface pressure gradient. We were able to estimate that the baroclinic and barotropic pressure gradients should balance at approximately 30 m. Below that depth we expect the change in the baroclinic term is the one that causes the changes in the velocity profile. We hypothesize that the peak of the anti-correlation between wind and currents at 114 m is a signature of the barotropic response to the wind. These finding are consistent with our results in similar inlets (e.g. enhanced or reversed surface outflow observed in Alberni Inlet (Farmer and Osborn, 1976; Farmer, 1976), Puget Sound (Matsuura and Cannon, 1997); Knight Inlet (Baker and Pond, 1995); Reloncavi Fjord (Castillo et al., 2012), and counter-currents at depth at around 100 m in Puget Sound (Matsuura and Cannon, 1997)).

The overall circulation in Douglas Channel in the seasonal and meteorological bands is a complex mixture of estuarine flow, directly wind driven flow, and the barotropic and baroclinic responses to changes to the surface pressure gradient caused by the wind driven currents. One unresolved question is 'What controls the thickness of the surface fresh layer and the thickness of the surface outflow layer'. The analysis with the Wedderburn number indicates that the magnitude of the surface wind plays an important role but wind mixing does not seem to be the entire answer. The role of internal wave mixing from waves generated at the various sills (including the 30 m deep sill in Verney Passage), and from other topographic features has not been addressed here. Not only are the answers to these questions essential in understanding the physical dynamics of the system, but they will also help us make better decisions to support the response planning for various pollutants, which may be neutrally buoyant at various depths in different seasons. The next natural research step would be to implement numerical models to study the sub-tidal circulation to explore the ideas suggested here. For example, it was clear that the wind mixing and the freshwater discharge alone cannot explain the thickness of the first outflow layer, and numerical "experiments" should provide a better understanding of other mixing mechanisms that could contribute to the first layer formation.

Acknowledgment

Data are available upon request from the corresponding author (di.wan@dfo-mpo.gc.ca). The authors would like to thank Bodo de Lange Boom at Canadian Hydrographic Service for discussions on the tide gauge data; the officers and crew of the research vessels CCG Tully and CCG Vector for helping us with the mooring deployment and recovery; Tamas Juhasz, David Spear, Lucius Perreault, Andrew Lee and others at the Institute of Ocean Sciences who helped with the mooring work and initial data processing; Richard Thomson and Jody Klymak for discussions during the earlier stages of this paper; and Patrick Cummins and the two anonymous reviewers for their constructive reviews and suggestions for making it a better paper. This work was supported by Fisheries and Oceans Canada through the World Class Prevention, Preparedness and Response to Oil Spills from Ships Initiative.

Table 2.2: Volume budget at FOC1 and KSK1. Negative numbers represent seaward flow, and positive numbers represent landward flow. The cross-channel widths (w_f for FOC1 and w_k for KSK1) at these two stations are parameterized as a function of depth (d): $w_f(d) = -7.7 \cdot d + 3770$ m, $w_k(d) = -10.2 \cdot d + 5286$ m, with d going from 0 to 360 m (results are from linear fits). The volume transport of each layer is then calculated by integrating the velocity profile (obtained from the cubic spline fits, Figure 2.5) over the cross-sectional area of the corresponding layer, assuming no cross-channel variation. The cross-sectional areas for FOC1 and KSK1 are $860,000$ m^2 and $1,242,000$ m^2, respectively.

		KSK1 Summer		FOC1 Summer		KSK1 Winter		FOC1 Winter
Layer	Depth [m]	10^3 [m^3 s^{-1}]	Depth [m]	10^3 [m^3 s^{-1}]	Depth [m]	10^3 [m^3 s^{-1}]	Depth [m]	10^3 [m^3 s^{-1}]
0	0	0.236	0-3	2.046				
1	1-33	-10.903	4-32	-11.524	0-22	-13.448	0-23	-10.300
2	34-82	9.405	33-131	19.105	23-169	22.206	24-158	22.142
3	83-149	-7.241	132-233	-5.263	170-248	-2.087	159-360	-4.287
4	150-360	19.689	234-360	11.798	249-360	1.067		
Net	0-360	11.186	0-360	17.304	0-360	6.864	0-360	7.555

Chapter 3

Wind-driven currents in a 'wide' narrow channel, with application to Douglas Channel, BC

Abstract

This paper applies a structured grid, 3-Dimensional Regional Ocean Modelling System (ROMS) to examine wind-driven currents of an idealized stratified channel, representative of Douglas Channel, British Columbia, Canada, where the increased marine activities require an improved understanding of the physical oceanography. The surface along-channel elevation slope resulting from the wind stress is strongly affected by the surface stratification and can serve as a proxy for gauging surface stratification in operational systems. In the case of strong surface stratification, due to rotational effects an apparently narrow (width << length) channel can be dynamically wide with pronounced cross-channel variation. The thickness of the surface wind-driven layer is scaled using the thermal wind relation, which provides a scaling factor to estimate the thickness of the surface layer. This scaling factor is not restricted to the wind-driven flow and could be expanded to the surface mean estuarine outflow layers.

3.1 Introduction

The response of fjords to wind forcing has been the subject of several observational, analytical and numerical modelling studies. Notable examples include the work of

Farmer and Osborn (1976) who found that the up-fjord winds deepen the surface outflow while down-fjord winds decrease the depth of the halocline. In Puget Sound, Matsuura and Cannon (1997) detected a sub-tidal direct wind response at 100 m depth when the stratification was weak; Bretschneider et al. (1985) and Matsuura and Cannon (1997) observed weak counter-wind currents in the lower outflow layer, and used an Empirical Orthogonal Function (EOF) analysis to relate it to the wind stress. Klinck et al. (1981) used a simple two-layer numerical model to study the wind influence in a narrow channel and on the shelf. They concluded that the modelled free-surface slope in a narrow channel reflects the tilt of the pycnocline and thus is a baroclinic effect. Physically narrow channels have narrow widths and the aspect ratio between the width and length is usually 1/10, or even smaller. The Rossby radius of deformation in dynamically narrow channels is much larger than the width of the channel so that Coriolis effects can be neglected. These classical results assume that a physically narrow channel is also dynamically narrow.

Studies on the response of fjords to wind forcing have typically neglected rotational effects based on observations that the Rossby radius of deformation is usually large in comparison with the fjord width. Farmer and Freeland (1983) suggest that rotation is of secondary importance when $W/R_d < 1$, where W is a scale width of the channel and $R_d = \sqrt{g'h}/f$ with g' being the reduced gravity, h is the depth of the channel, and f the Coriolis parameter. Rotational effects are also expected to be unimportant for short term fluctuations (periods less than half a pendulum day). Spall et al. (2017) examined two primary regimes: fjords that are narrow, and broad as compared to the first baroclinic deformation radius, concluding that rotational effects can become important as the width of the fjord becomes much wider than the Rossby radius. Rotational effects are usually neglected in dynamically narrow channels ($W/R_d < 1$) where the width is smaller than the first Rossby radius. The channel becomes dynamically wide if W/R_d is larger than 1, and intermediate when it is around 1.

Here, we consider the wind-driven response of a physically narrow channel (width/length $<<$ 0.1) in the context of Douglas Channel (Figure 3.1), a deep fjord on the west coast of British Columbia, Canada, which is a major transport artery to the town of Kitimat B.C. Because of the steep sides of channel, the wind in the system should follow approximately along the channels. We use the wind in Nanaska Shoal Buoy (Figure 3.1) to the wind in the Douglas Channel. Increases in marine transportation, such as resulting from a proposed Liquified Natural Gas (LNG) facility, have led to increasing concerns about spill accidents. A clear understanding of the wind-driven

circulation in the area is important for improving models of LNG transport.

Pioneering observational oceanographic work done by Pickard (1963), Webster (1980a,b) and Macdonald (1983) provided detailed descriptions of oceanographic conditions based on the extensive measurements carried out in 1977 and 1978 in the Kitimat fjord system, of which Douglas Channel is the main waterway. More recently, Wan et al. (2017) provided a thorough analysis of observations made between 2013 and 2015 on the sub-tidal circulation in Douglas Channel. The magnitude of the direct wind-driven surface (5 m depth) current is about $2-4\%$ of the wind velocity on average, and this result is consistent throughout all available observational time periods between July 2013 and July 2015 (Wan et al., 2017). Below this direct wind-driven surface layer, the correlation between currents and wind decreases rapidly becoming negative below 20 m; the anti-correlation peaks between $50-150$ m depth [Figure 7 in (Wan et al., 2017)]. The average depth of the channel is about 400 m. The mid-depth (around 50 to 200 m) anti-correlation and the small lag (less than 5 hours) suggest that the flow is mostly a barotropic response. Although Wan et al. (2017) did not discuss the deep response in detail, a weak but positive correlation is present just below the sill depth at about 220 m.

In this paper, based on numerical simulations that represent an idealization of the Douglas Channel, we study 1) how the structure of the velocity field changes in response to variations in the strength of the wind forcing; and 2) the sensitivity of the response to variations in the stratification and Coriolis parameter. Contrary to initial expectations, it is found that the wind-driven response has significant cross-channel structure due to the importance of motions that project onto the higher-order vertical modes whose deformation radii are smaller than the channel width. Implications of the importance of higher modes to the wind-driven circulation are discussed below.

In the following section, the configuration of the numerical model is described. Results of the simulations are presented in Section 3, followed by a discussion of these results in Section 4. Conclusions are given in Section 5.

3.2 Numerical model setup

The numerical model used in this study is the hydrostatic regular grid Regional Ocean Modeling System (ROMS) 3.7 (Shchepetkin and McWilliams, 2005). ROMS is designed as a general circulation model for regional applications (Haidvogel et al., 2000, 2008), including applications in estuaries and fjords (Warner et al., 2005a;

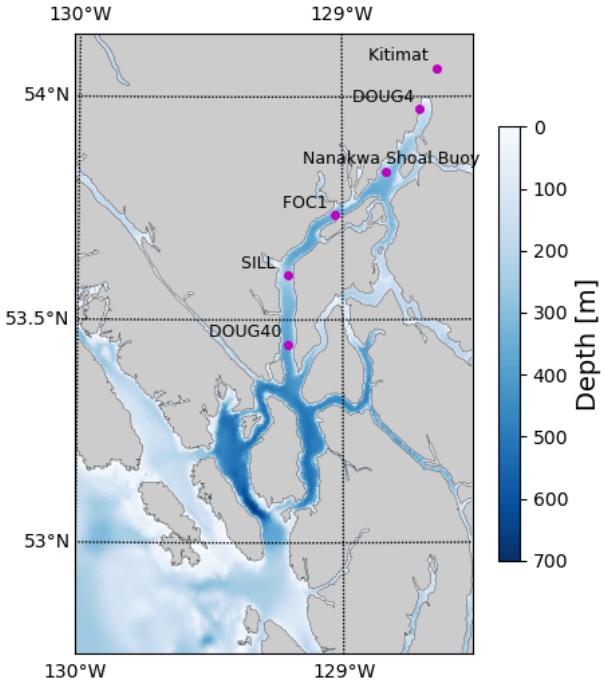

Figure 3.1: Map of Kitimat system. For the purpose of the paper here, we consider Douglas Channel, the main waterway of the system, as the channel from the northern end close to DOUG4 to the shelf. The 200 m deep sill is located between FOC1 and DOUG40. The observed wind data are taken from the Nanakwa Shoal buoy. FOC1, DOUG4, DOUG40 are the locations of CTD stations.

Myksvoll et al., 2012).

Our interest in the circulation is in the along-channel wind-driven response, and the model is configured such that it captures the characteristic dimensions that are broadly consistent with Douglas Channel. For the sake of simplicity, we align the along-channel direction of the model with the west-east direction, and the east 150 km section of the model domain represents Douglas Channel from the head to the shelf. The model domain is 700 km long and 5 km wide (Figure 3.2). The west 300 km is set as a sponge layer to ensure there is no reflection of any signal from the west boundary. The water depth is 400 m everywhere except the inclusion of a sill situated 55 km from the head of the channel (eastern end). The top of the sill is 200 m deep, and is analytically represented by two hyperbolic-tangent functions with no cross-channel variation. The landward basin is referred to as the inner basin and the seaward basin is referred to as the outer basin. The north, south, and east boundaries are closed free-slip boundaries; gradient open boundary conditions are implemented at the west boundary for momentum, free-surface displacement, and tracers (salinity in this case). The horizontal resolution is uniform at 1 km in the x-direction (along-channel), and 250 m in the y-direction (cross-channel). Free-slip boundary conditions are used here because the resolution is insufficient to resolve the frictional boundary layers and boundary effects are not the focus of this study.

In the vertical, a 30-level S-coordinate system is used. The resolution at the surface is increased using the ROMS parameter $\theta_s = 3.0$ to account for the stronger stratification, and the bottom resolution is only slightly increased with $\theta_b = 1.5$, using the stretching functions described in Shchepetkin and McWilliams (2009). This transformation yields approximately 1–4 m resolution at the surface and about 20 m from mid-depth to the bottom in the 400 m of water. For the vertical mixing, the $k-\epsilon$ scheme is used as the turbulence closure scheme (Warner et al., 2005b), and the horizontal viscosity coefficient is set to be constant at 25 $\mathrm{m^2\ s^{-1}}$.

The model is forced by a uniform wind stress directed from the west (open boundary) to the east end (fjord head, closed boundary) with a linear ramping-up time of 2 days after which time the winds remain constant over the entire domain. Two cases of wind forcing are considered: a low wind stress case (0.025 $\mathrm{N\ m^{-2}}$, equivalent to 4.3 $\mathrm{m\ s^{-1}}$) and a high wind stress case (0.1 $\mathrm{N\ m^{-2}}$, equivalent to 8.6 $\mathrm{m\ s^{-1}}$). The Coriolis parameter is set to $1.18 \times 10^{-4}\ \mathrm{s^{-1}}$, corresponding to 54° N, the approximate latitude of Douglas Channel.

The initial salinity is parametrized by a linear dependence through the top 15

m, followed by an exponential function from 15 m to the bottom (Figure 3.3), closer to the summer stratification. Summer and winter profiles are not very different and there is one run that is more stratified than r_3–r_5 (Table 3.1) and other two runs are less stratified. The initial conditions are horizontally homogeneous. For the sake of simplicity, temperature is kept at 8°C, so density is dependent only on salinity. The horizontal homogeneous density initial condition profile ($\partial\rho/\partial x = 0$, and $\partial\rho/\partial y = 0$) is set up because we are studying the wind-driven component in this idealized study. The estuarine circulation is present in the channel, but here we only focus on the wind-driven modification to the dynamics. The first baroclinic Rossby radius is about $7-8$ km, which is larger than the width of the channel (5 km).

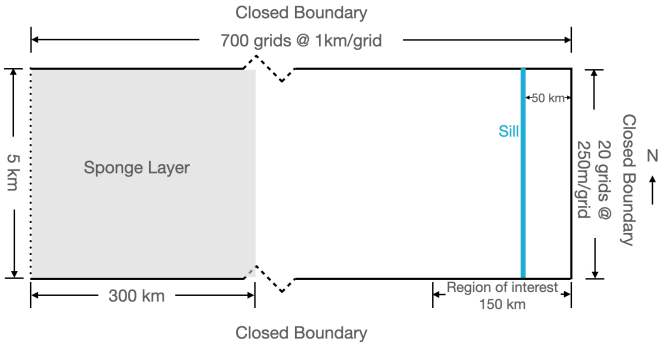

Figure 3.2: Top view of the setup of ROMS model. Wind stress is applied uniformly in the entire domain with linear damping within the sponge layer. The bottom friction in the sponge layer increase linearly from east to west.

In addition to having a source of fresh water at its head, as is typical of many fjords, substantial freshwater also enters Douglas Channel along its entire length from the runoff of precipitation on its steep sides (Weber, 1983; Wan et al., 2017). This leads to the rapid restoration of the surface stratification following wind events that mixed the surface layer. For example, in October to November 2015, a few wind events occurred during a survey cruise (Cruise ID 2015-54). CTD profiles taken before and after these wind events (Figure B.1 and B.2 in the Supporting Information) show that the stratification is restored quickly at the seaward station (Doug40). The Nov 1 and Nov 6 profiles at Doug 40 are almost identical despite the fact that a consistent positive wind signal occurred between these profiles. The profiles before and after the strong outflow wind event (Oct 24 to Oct 29) did not change the profile at Doug40 significantly if we compare the Oct 19 and the Nov 1 Doug40 profiles (Figure B.2).

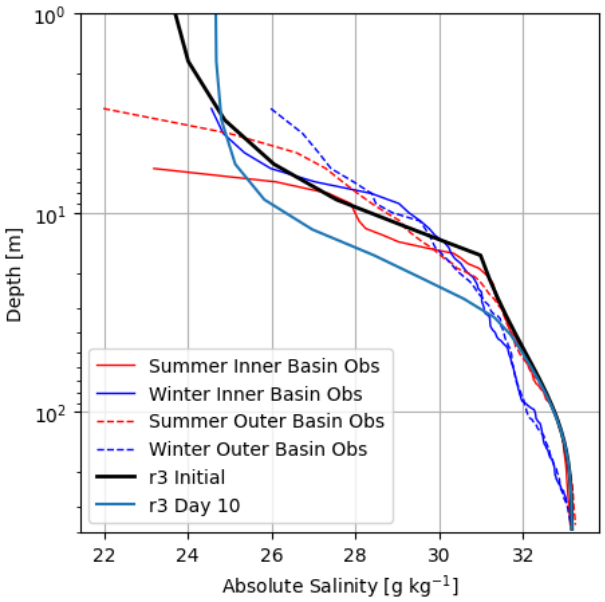

Figure 3.3: Observed and the base run initial Absolute Salinity. The inner basin location is at FOC1 and the outer basin location is at KSK1. The summer profile is averaged from the July 2013 and July 2014 cruise CTD data, and the winter profile is averaged from the April 2014 and October 2014 cruise CTD data.

Profiles at Doug4 (landward station) also showed a quick restoration of the surface stratification (Oct 19, Oct 24, and Nov 6). The fresher surface water at Doug4 seems to be related to the increase of freshwater discharge prior to Oct 24 (Figure B.1 shows the Kitimat River discharge during the same time period). These CTD profiles demonstrate the fast restoration of stratification in Douglas Channel, and the freshwater input throughout the channel is the presumed mechanism responsible for this. This justifies a need for a tight 2-3 day time scale nudging over the entire domain in the numerical model. A 2-day nudging for salinity is chosen for the model runs when nudging is applied to represent this restoration mechanism.

We consider a range of stratifications to approximate Douglas Channel. The basic stratification is linear in the top 15 m where the stratification is varied in the stratified experiments (Table 3.1, with these profiles shown in Figure B.3 in the Supporting Information), and exponential below that. The surface salinity varies from 20 to 30 g kg^{-1}, and the salinity at 15 m is set to 30.7 g kg^{-1} for all cases. The e-folding scale is chosen to be 50 m to match the observations.

3.3 Results

In total, 10 model runs are considered here (Table 3.1): 2 barotropic runs with 2 wind stresses (r_{1_0} and r_{1_1}, respectively), and 8 stratified runs: 4 stratifications, with 2 wind stresses (r_2 to r_5). In all the model runs, the first number refers to the initial stratification (r_4 is the least stratified and r_5 is the most stratified), and the second number refers to the wind stress (_0 and _3 are the low wind cases, and _1 and _4 are the high wind cases).

3.3.1 Barotropic runs

For the barotropic case, the surface slope ($\partial\eta/\partial x$) is very small, where η is the surface elevation, and x is the along-channel direction coordinate. There is less than a 1 mm rise at the end of the channel in the low wind case, and a less than 3 mm rise in the high wind case. These small values are not surprising given the substantial depth of the channel. Starting from the linearized momentum equation and neglecting Coriolis force, at steady-state ($\partial u/\partial t = 0$, where u is the along-channel velocity), the vertically

Table 3.1: Model Setups. r_1s are the barotropic runs. The salinity at $z[-15, 0]$ (from -15 m to surface) is $-\frac{c_0 \cdot (z+15)}{15} + 30.7$, and the salinity at $z[\text{bot}, -15]$ (from the bottom to -15 m) is $33 - 3 \cdot \exp(z/50)$. c_0 is shown in the table.

Run	c_0	Wind Stress $[\frac{\text{kg}}{\text{ms}^2}]$	Nudging
r_{1_0}	n/a	0.025	No
r_{1_1}	n/a	0.1	No
r_{2_3}	2.7	0.025	Yes
r_{2_4}	2.7	0.1	Yes
r_{3_3}	7.7	0.025	Yes
r_{3_4}	7.7	0.1	Yes
r_{4_3}	0.7	0.025	Yes
r_{4_4}	0.7	0.1	Yes
r_{5_3}	10.7	0.025	Yes
r_{5_4}	10.7	0.1	Yes

integrated equation of motion (Farmer, 1976) is:

$$\tau_s - \tau_b = H\rho_0 g \frac{\partial \eta}{\partial x}, \tag{3.1}$$

where τ_s is the surface stress, τ_b is the bottom stress, H is the depth of the channel, g is the gravitational acceleration, ρ_0 is the density, and η is the surface elevation. Assuming τ_b is negligible and H is uniform at 400 m, the magnitude of $\partial\eta/\partial x$ is the order of $O(10^{-9})$ for the low wind case and $O(10^{-8})$ for the high wind case. These results show that, in the absence of stratification, a channel with the dimensions of Douglas Channel is at least one order of magnitude too deep for the wind stress to provide significant observable surface elevation changes.

Below the surface Ekman layer, the velocities in these barotropic runs are generally very small. Wind stress acts directly on the surface layer, and the momentum propagates down the water column through the vertical viscosity. In the top layer ($<$ 1 m depth), the along-channel velocity is around 1% of the wind speed in both the low and high wind cases as shown in Figure 3.8. This is smaller but generally consistent with the 3% rule of thumb of (Weber, 1983) and the observed $2-4\%$ in Douglas Channel (Wan et al., 2017). This velocity decreases very quickly with depth, and reverses to the counter-wind direction with a very small magnitude. The counter-wind direction velocity seems to be driven by the surface pressure gradient due to the small surface elevation from the numerical results. The system reaches steady state quickly after the wind stabilized after 2 days and the vertically integrated along-channel velocity tends to zero.

3.3.2 Base run

The base baroclinic case (r_{3_3} in Table 1) has a surface salinity of 23 g kg^{-1}, low winds (0.025 N m^{-2}), and includes nudging of salinity to its initial state.

The along-channel surface elevation slope increases in the first 5 days and reaches steady state around Day 8 at $3\cdot10^{-7}$ (3 cm over 100 km). The surface elevation shows that there is along- and cross-channel variation. The surface elevation is higher at the south boundary than the north boundary due to Coriolis force. The surface elevation slope in the cross-channel direction is generally one order of magnitude higher than in the along-channel direction (Figure 3.4 Top Panel).

The surface velocity in the along-channel direction (Figure 3.4) is generally up-

channel (eastward) with a weak return flow in the north-east end of the channel. The surface cross-channel velocity is mostly southward except at the eastern end of the channel, where stronger northward return flow is present at the east end of the channel due to volume conservation.

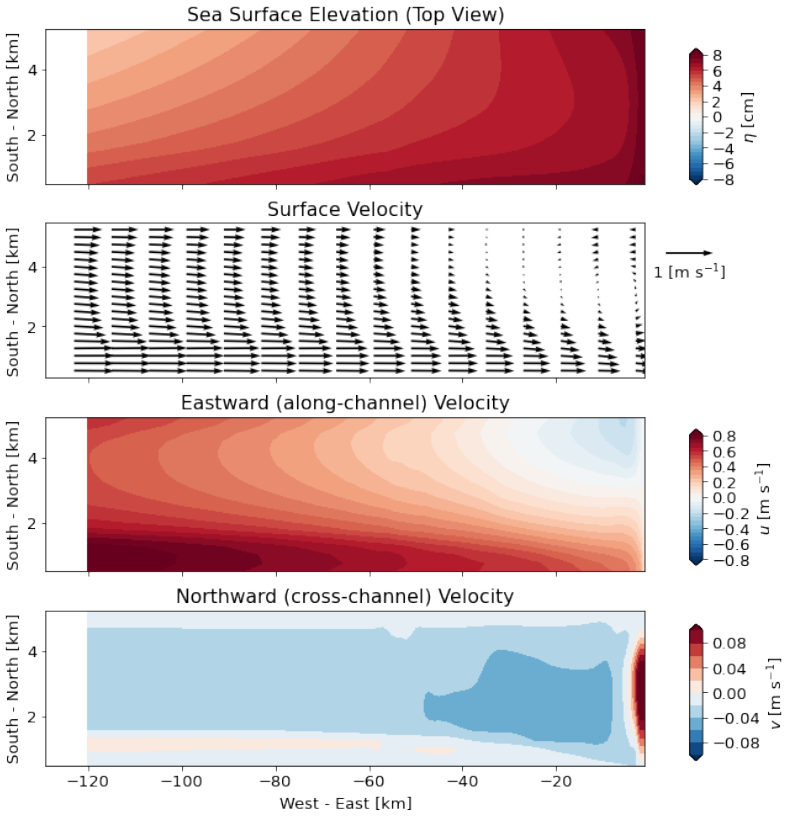

Figure 3.4: Plan view of the surface elevation η, and surface velocity in case r_{3_3}. Top: Sea surface elevation contour plot; second: surface velocity quiver plot; third: eastward (along-channel) velocity (u); bottom: northward (cross-channel) velocity.

The volume is overall balanced by return flows under the surface layer. The along-channel velocity below the surface velocity layer is westward in the out-fjord direction at mid-depth (Figure 3.5). The cross-channel velocity below the surface is northward.

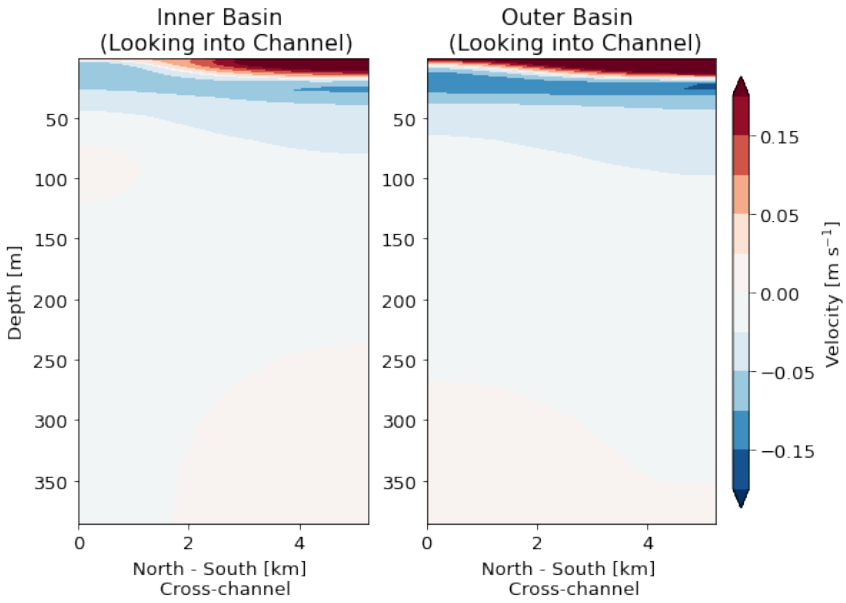

Figure 3.5: Contours of the along-channel velocity in experiment r_{3_3}. Looking into the channel denotes looking from the west to the east direction. Red is in the up-fjord direction. The inner basin cross-section is taken at about 40 km from the head of the closed east end representing FOC1, and the outer basin cross-section is taken at about 80 km from the head of the closed end of the channel representing KSK1.

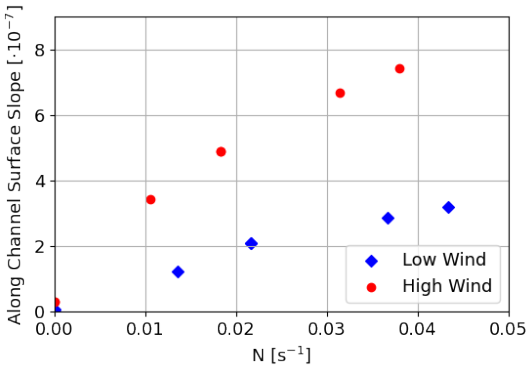

Figure 3.6: Surface elevation slopes in 4 different initial stratifications averaged between Day 15 and Day 20. $N = \sqrt{\frac{g}{\rho_0}\frac{\rho(40)-\rho(0)}{40\text{m}}}$, where $\rho_0 = 1025$ kg m^{-3}.

3.3.3 Baroclinic runs

The effect of stratification on the Surface Slope

The along-channel surface slope response varies with the surface stratification. The along-channel slope results are shown in Table 3.2 and Figure 3.6. These slopes are cross-channel averaged values. As expected, stronger wind produces larger surface slopes, and the surface slope monotonically increases with the surface stratification as measured by the Brunt Väisälä frequency, N. The latter is based on the density difference across the top 40 m, temporally averaged between days 15 and 20 of the simulations, assuming linear stratification.

Table 3.2: Surface Slope Results

Run	N initial	N (Day 15-20)	Slope 10^{-7}	Nudging
r_{2_0}	0.026	0.023	1.8	No
r_{2_1}	0.026	0.011	4.2	No
r_{2_3}	0.026	0.022	2.4	Yes
r_{2_4}	0.026	0.020	5.6	Yes
r_{3_0}	0.040	0.039	2.6	No
r_{3_1}	0.040	0.029	6.5	No
r_{3_3}	0.040	0.037	3.2	Yes
r_{3_4}	0.040	0.032	8.1	Yes
r_{4_0}	0.018	0.006	1.3	No
r_{4_1}	0.018	0.001	2.9	No
r_{4_3}	0.018	0.014	1.3	Yes
r_{4_4}	0.018	0.012	3.9	Yes
r_{5_0}	0.047	0.046	2.8	No
r_{5_1}	0.047	0.038	7.4	No
r_{5_3}	0.047	0.044	3.5	Yes
r_{5_4}	0.047	0.039	9.0	Yes

Surface Velocity

The along-channel component of the surface current is in the same direction as the wind – into the fjord, and we call this layer the surface layer. The thickness of this surface layer is determined by the depth of the zero-crossing of the along-channel velocity, and this thickness varies in the along- and cross-channel directions.

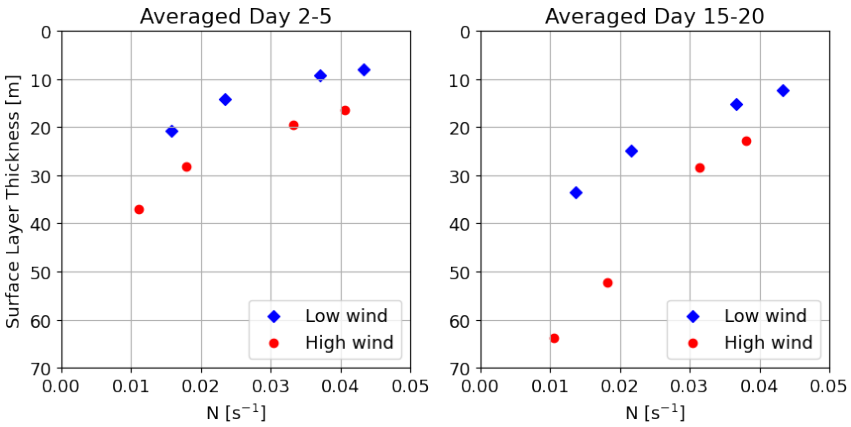

Figure 3.7: Surface velocity layer thickness in the low wind and the high wind cases and the surface stratification. The thicknesses are calculated in the inner basin.

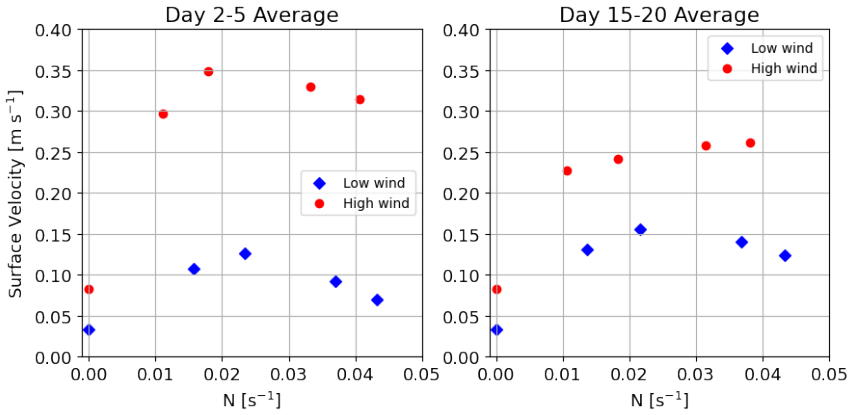

Figure 3.8: Along-channel surface velocity at 5 m depth in cases with different initial stratifications and for the barotropic runs. The velocities were taken from the top layer. Left: averaged surface velocity and N between Day 2 and Day 5; right: averaged between Day 15 and 20. The surface velocity and N are averaged in the cross-channel direction at 40 km from the eastern boundary.

The spatial variation in the cross-channel direction is caused by the closed east boundary. The section plot in Figure 3.5 shows that the surface up-fjord velocity layer in the inner basin (up-inlet from the sill) is more concentrated and weaker on the south side of the channel than in the outer basin, and the return flow is weaker in the inner basin than in the outer basin.

The cross-channel averaged thickness of the surface velocity layer decreases with increasing surface stratification, with increasing wind forcing resulting in a thicker surface layer (Figure 3.7). Under the conditions of strong wind forcing and weak stratification, this surface velocity layer extends to as deep as 63 m in the inner basin.

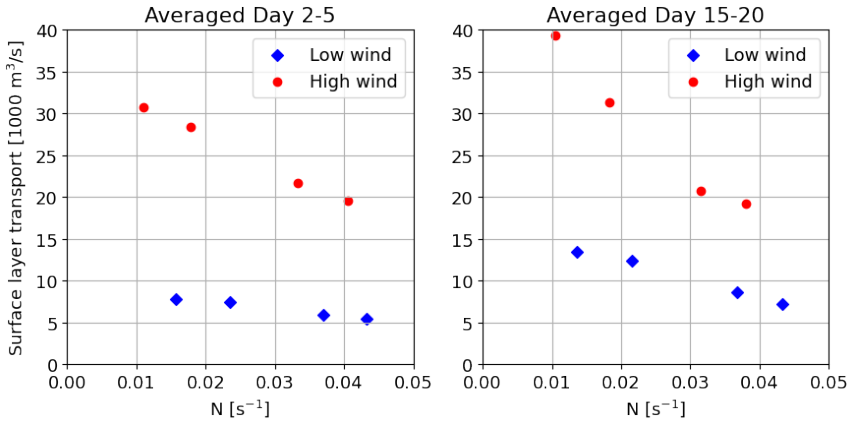

Figure 3.9: Surface velocity layer transport in the low wind and the high wind cases and the surface stratification. The transports are calculated in the inner basin.

The surface layer volume transport generally decreases as the surface stratification increases (Figure 3.9), and the increase of the volume transport in the high wind case as compared to the low wind conditions is approximately proportional to the wind stress (4 times difference between the high and low wind stresses).

Transient state vs. steady state

The time evolution of the along-channel elevation slope and density slope has two dominant time scales. After the initial start up, $\Delta\eta/\Delta x$ increases, which represents the pile-up of water in the inner basin, and deepens the isopycnals in the inner basin. The surface time evolution is largely done by Day $3-4$. Baroclinic adjustment

continues, and isopycnals become shallower and eventually reach steady state on around Day 8, lagging the barotropic surface response by about 3 days (Figure 3.10).

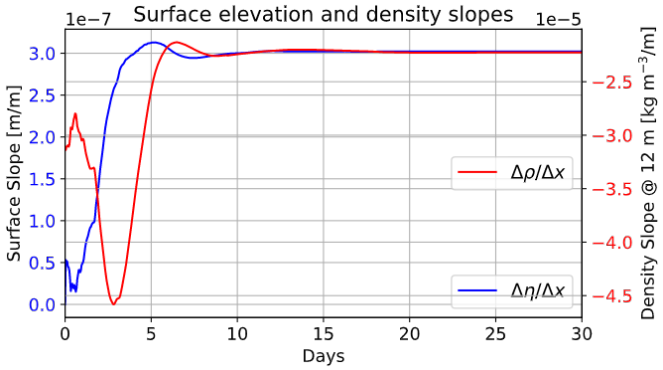

Figure 3.10: Surface elevation slope ($\Delta\eta/\Delta x$) and the density slope ($\Delta\rho/\Delta x$ at 12 m depth) between the inner and the outer basins.

3.4 Discussion

In this section, we first look at how the along-channel surface slope responds to the surface stratification and then we focus on the surface layer thickness analysis. We use thermal wind to explain the surface dynamics, and explore the vertical velocity structure using vertical mode analysis. Finally, we propose a scaling factor for the surface layer thickness to analyze the relative importance of different variables in determining the surface layer thicknesses.

3.4.1 Along-channel Surface Slope and Stratification

The along-channel free surface slope is mostly a baroclinic effect, similar to what Klinck et al. (1981) found in their two-layer model where they argued that the free surface slope was a reflection of the pycnocline tilt. The deepening of the isopycnal at the head of the inlet requires more less-dense fluid to balance a larger surface slope. In the baroclinic runs (r_2 to r_5), the surface elevation slope varies with the surface stratification (Figure 3.6). The slope is quite sensitive to the stratification. Given the initial stratification between $N = 0.019$ s^{-1} and 0.056 s^{-1} in the top 50 m, the slope differs by 2 to 3 times. This translates to $2-3$ cm elevation difference at the head of

the channel in the high wind case and $1-2$ cm elevation difference in the low wind case. Dynamically, this relationship can be demonstrated through introducing density into the vertically integrated linearized momentum equation, neglecting Coriolis force:

$$\tau_s - \tau_b = Hg\rho_0 \frac{\partial \eta}{\partial x} + g \int_{-H}^{\eta} \int_{-H}^{\eta} \frac{\partial \rho}{\partial x} dz' dz \tag{3.2}$$

In this case, the horizontal baroclinic pressure gradient may balance a larger surface slope, $\frac{\partial \eta}{\partial x}$, while the wind and bottom stresses on the left hand side are unchanged.

Assuming τ_b is negligible and dividing Equation (3.2) by $\rho_0 g \frac{\partial \eta}{\partial x}$, we have:

$$h_s = \frac{\tau_s}{\rho_0 g \frac{\partial \eta}{\partial x}} = H + \frac{g \int_{-H}^{\eta} \int_{-H}^{\eta} \frac{\partial \rho}{\partial x} dz' dz}{\rho_0 g \frac{\partial \eta}{\partial x}}, \tag{3.3}$$

where h_s is a measure of stratification and it indicates how much baroclinic component there is in the surface elevation tilt. If there is no stratification, $h_s = H$, and the surface stress balances the surface pressure gradient. h_s decreases to close to 0 if the surface slope is just a reflection of the baroclinic adjustment, such as the isopycnal tilt in a two-layer model set up. Conceptually speaking, h_s is the water depth minus the baroclinic adjustment. We call this h_s as the surface layer thickness as it is the remaining part of the water depth that is not balanced by the baroclinic adjustment. In this study, we kept the wind steady during the entire baroclinic adjustment period. In reality, this is not likely to happen. However, the mechanism and the formulation of h_s remains valid: h_s changes with the second baroclinic adjustment term.

The surface layer thickness h_s can be estimated from the observations of the wind stress and the along-channel elevation gradient using Equation (3.3). The top panel of Figure 3.11 shows observations of the wind stress in Douglas Channel (Nanakwa Shoal Buoy in Figure 3.1) and the along-channel elevation gradient estimated from the tide gauges at Hartley Bay and Kitimat (Figure 3.1; positive means that Kitimat sea level is higher than Hartely Bay). Both the winds and the water levels have been filtered through a Godin filter (Godin, 1972) to remove the high frequency signals. Figure 3.11 shows the time series for the period July through November 2015. The positive wind stress means the wind is in the up-fjord direction.

Continuous sea surface elevation and wind stress observations in Douglas Channel from July to Nov 25, 2015 (Figure 3.11) show that h_s is generally less than 10 m in July and August, indicating the surface slope is mostly caused by tilt of the pycnocline. h_s has more variability between September and November, with peaks as high as 100

m, suggesting low stratification events.

The top panel in Figure 3.11 shows a difference in the slope response between the up- and down-fjord wind. When the wind is blowing up-fjord, the surface slope tends to be enhanced, corresponding to higher surface stratification; when the wind is blowing down-fjord, the surface slope is reduced, corresponding to lower surface stratification. These responses are consistent with results in Farmer (1976): down-fjord winds decrease the depth of the halocline.

The wind stress and elevation can be used to estimate the surface layer thickness from Equation (3). The thickness (h_s) is typically less than 10 m in July and August, which shows that the surface slope is dominated by the tilt of the pycnocline. In the fall (September to November), h_s shows much more variability with peaks as high as 100 m during large storms suggesting low stratification events. The fact that h_s returns to values between 1 and 10 between storms indicates that the stratification is rapidly re-established after a storm.

3.4.2 Surface Layer Thickness and Geostrophic Balance

If we define the thickness of the surface wind-driven layer by the first zero-crossing of the velocity profile where the along-channel velocities change from the along-wind direction to counter-wind direction, we see that this surface layer thickness becomes thinner as the stratification becomes stronger in all the runs with nudging (Figure 3.7). The depths of these velocity zero-crossings are in fact well below the mixed layer depths in all cases (Figure B.4), and this suggests that the wind is not the sole factor that is responsible for the thickness of the surface layer.

Integrating the forcing terms in the along-channel direction over the first two days shows that the Coriolis term is the key contributor in determining the thickness of the surface layer. The surface Ekman layer is defined as where the vertical viscosity term in the in-fjord direction is balanced by the Coriolis force (see Figure 3.12) . Below the Ekman layer, the Coriolis term changes direction from the counter-wind direction to along-wind direction and is the dominant term. This changing Coriolis term is caused by the return flow in the cross-channel direction that is set up by the cross-channel barotropic pressure gradient. The Coriolis term balances the along-channel pressure gradient forces, which forms the geostrophic flow in the along-channel direction (Figure 3.12).

The dynamics governing the thickness of the surface velocity layer is simply under-

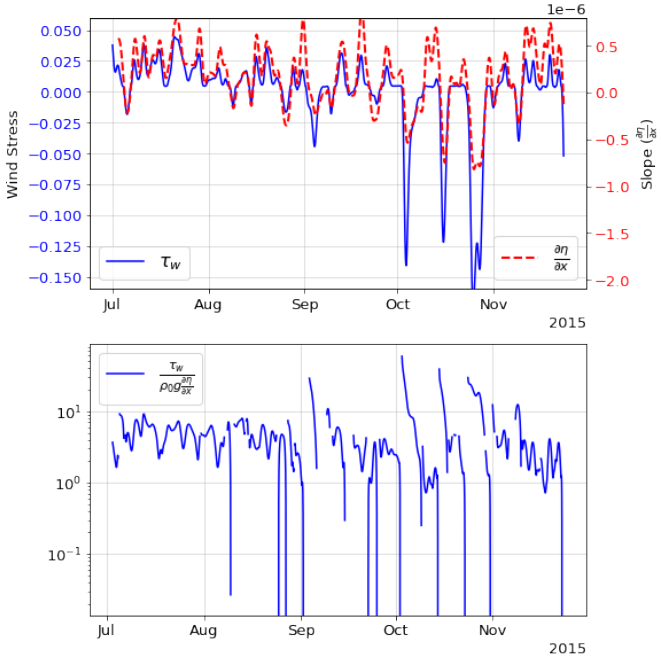

Figure 3.11: Top: Low-passed surface elevation slope from observations and the wind stress in Douglas Channel from July to Nov 2015. Bottom: wind stress divided by $\rho_0 g \frac{\partial \eta}{\partial x}$, and the results are h_s, where h_s is the measure of stratification explained in Equation 3.3. The surface slope is calculated from the elevations in Kitimat and Hartley Bay. The wind data and the elevation data are re-sampled every hour and the Godin filter is used to remove high frequency signals. In the lower panel, $\frac{\partial \eta}{\partial x}$ values in the range [-0.1, 0.1] $\cdot 10^{-6}$ were deleted avoid near 0 values.

stood from geostrophy and the thermal wind relation. Combining the cross-channel geostrophic balance and hydrostatic balance (Pedlosky, 1987), we then obtain the thermal wind relation for the along-channel flow (Thomson and Ware, 1996; Thomson et al., 2007):

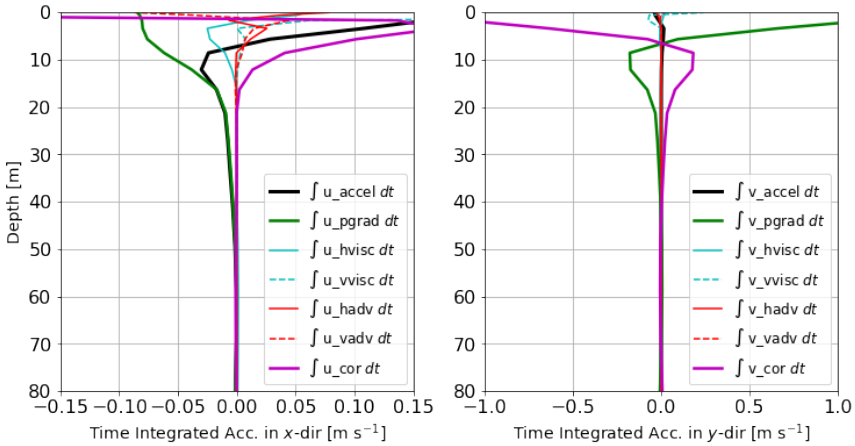

Figure 3.12: Integrated acceleration diagnostic terms from Day 0 to Day 2 in case r_{4_3}. The x axes are truncated in order to show the structure of the other terms. The x-dir is in the along-channel direction, and the y-dir is in the cross-channel direction.

$$f\frac{\partial u}{\partial z} = \frac{g}{\rho_0}\frac{\partial \rho}{\partial y} \tag{3.4}$$

where ρ is the water density and ρ_0 is the reference density.

From the geostrophic equation $fu = -\frac{1}{\rho}\frac{\partial p}{\partial y}$, we can see the zero-crossing for the along-channel velocity occurs when the pressure gradient in the cross-channel direction equals 0: the barotropic and the baroclinic pressure gradients balance each other. The thermal wind equation relates the cross-channel isopycnal tilt with the vertical shear of the along-channel velocity. The vertical shear of the along-channel velocity is enhanced with increased surface stratification due to shoaling of the depth of the velocity zero-crossing. This explains why the surface velocity layer thickness becomes smaller as the stratification becomes stronger in Figure 3.7. Relating thermal wind relations with the along-channel velocity structure is shown previously in wide channels. For example, in Juan de Fuca strait (Thomson et al., 2007) and in Clyde Sea (Janzen et al., 2005), where the widths are about 15 - 40 km and 40 km, respectively, thermal wind relations are used to provide explanations to the cross-channel

structures. Now we will look at the vertical modes supported by the vertical density profiles to see if the thermal wind structure is consistent with the vertical modes.

3.4.3 Vertical Modes

The vertical structure of the horizontal velocity profiles leads to further examinations into the vertical modal structures. Assuming a flat bottom, the vertical structure of normal modes (Kundu and Cohen, 2008) are governed by:

$$\frac{d}{dz}\left(\frac{1}{N^2}\frac{d\psi_n}{dz}\right)+\frac{1}{c_n^2}\psi_n=0, \tag{3.5}$$

where ψ_n is the vertical structure of the mode number $n = 0, 1, 2, ...$, and c_n is the separation constant (eigenvalue) whose physical interpretation is the phase speed for mode n. The boundary conditions are imposed at the surface and the bottom:

$$\frac{d\psi_n}{dz}=0 \text{ at } z=0,-H. \tag{3.6}$$

ψ is normalized so that $\int_{-H}^{0}\psi^2 dz = 1$. The vertical mode shapes (ψ_n) can be numerically solved as an eigenvalue problem by providing N^2, with c_n being the eigenvalues, and ψ_n the eigenvectors. The vertical modes are normalized according to the condition: $\frac{1}{H}\int_{-H}^{0}\psi_k\psi_j dz = \delta_{kj}$, where δ_{kj} is the Kronecker delta. The Rossby radius for mode n is given by c_n/f. The modes are normalized according to the condition:

$$\frac{d\psi_n}{dz}=0 \text{ at } z=0,-H. \tag{3.7}$$

The horizontal current velocity can then be decomposed as:

$$u(z)=\sum_n a_n\psi_n(z), \tag{3.8}$$

where u is the velocity at depth z, and a_n are the amplitudes of the vertical structure of modes.

The modal structures are numerically calculated using the density profiles in the middle of the channel in the inner and the outer basins on Day 10 (Figure 3.13). The first 3 modes account for about 80% of the velocity structure. The magnitudes associated with the second and the third modes are generally twice as large as those of the first mode (Table 3.3) even though the Rossby Radius from Mode 1 is wider than the width of the channel. Webster (1980b) carried out similar analysis for the

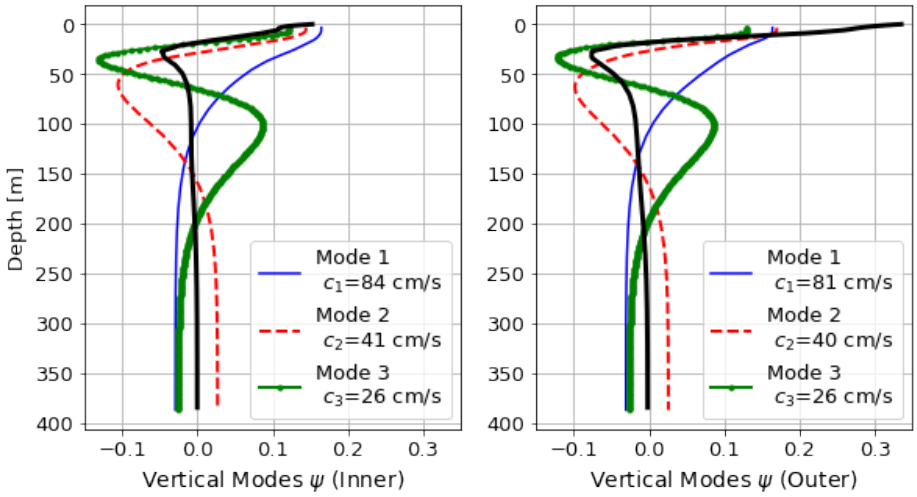

Figure 3.13: Vertical modes (r_{2_3} as an example) from the inner (left) and the outer (right) basins. The black lines represent the velocity profiles. The vertical modes are calculated numerically using the density profile in the middle of the channel.

M_2 internal tides in Douglas Channel. It was found that the energy in the second mode is often comparable and sometimes higher than the first mode.

The second baroclinic Rossby radius from the observations is about 3 km and the third baroclinic Rossby radius is about 2 km, and both are smaller than the width of Douglas Channel (about 4 to 5 km). Therefore, Douglas Channel cannot be treated as a dynamically narrow channel. The dominance of the second and the third modes explain most of the cross-channel spatial structure shown in Figure 3.4. It seems that Douglas Channel fits in the intermediate-width channel range described by Cushman-Roisin et al. (1994), where the channel width is on the order of the relevant Rossby radii, and the Coriolis force causes upwelling and downwelling responses at the closed side walls.

3.4.4 Scaling of the Surface Layer Thickness

Another un-answered question is what is controlling the thickness of the surface layer. Given the observed salinity, there is not any obvious mixed layer depth at the surface. Having shown that Douglas Channel is a dynamically intermediate width channel, we use the thermal wind relation to estimate the thickness of the surface layer whose velocity is in the direction of the wind. Define D as the depth where $u = 0$, W

Table 3.3: Decomposition results.

Run	a_1[m s^{-1}]	a_2[m s^{-1}]	a_3[m s^{-1}]	(%) Accounted For	Rd_1
r_{2_3}	0.14	0.30	0.22	81%	7 km
r_{3_3}	0.11	0.22	0.23	75%	8 km
r_{4_3}	0.15	0.27	0.19	79%	7 km
r_{5_3}	0.08	0.18	0.25	76%	9 km
r_{2_4}	0.14	0.30	0.22	81%	8 km
r_{3_4}	0.11	0.22	0.23	75%	10 km
r_{4_4}	0.15	0.27	0.19	79%	8 km
r_{5_4}	0.08	0.18	0.25	76%	11 km

the channel width, $U = |u(z = -2 \text{ m})|$ the surface along-channel velocity, $g' = g(\rho_2 - \rho_1)/\rho_0$, then the thermal wind relation can be scaled as:

$$f\frac{U}{D} = \frac{g}{\rho}\frac{\rho_2 - \rho_1}{W} \tag{3.9}$$

$$D = \frac{fUW}{g'} \tag{3.10}$$

This represents the critical condition (Cushman-Roisin et al., 1994) where the isopycnal in the cross-channel direction surfaces at the north end.

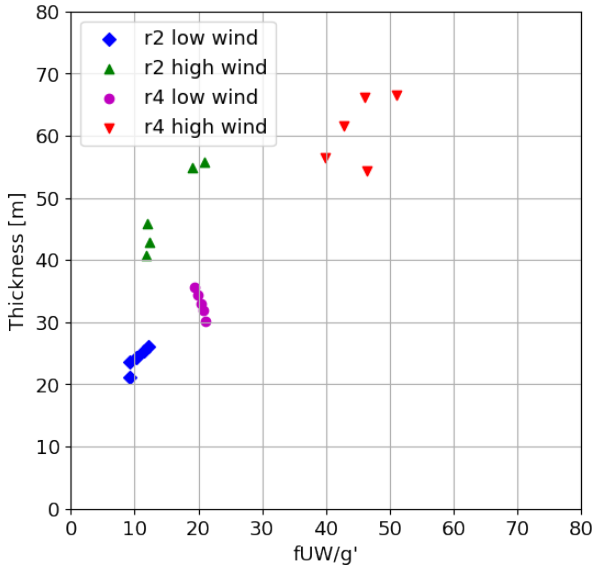

Figure 3.14: The surface velocity thickness averaged cross-channel and the scaling factors in 4 different cases.

Additional model runs are used to test sensitivity to the Coriolis parameter. In addition to the original $f = f(54° \text{ N})$ case, four different Coriolis parameters are set up: $f = f(15°\text{N})$, $f(25°\text{N})$, $f(35°\text{N})$, and $f(80°\text{N})$. For negative Coriolis coefficients, the results in the cross-channel direction simply reverse. Since the first layer thickness changes across the channel, D is calculated as the cross-channel averaged value. g' is calculated from the $\rho_2 = \rho(z = -35\text{m})$ and $\rho_1 = \rho(z = -15\text{m})$. The depths used here to calculate g' are chosen to match the approximate observations but it should be noted that the calculations are very sensitive to g'. The scaling factor D estimates

the first layer thickness well in both low and high wind cases (Figure 3.14). The results show that the thickness of the surface layer increases as the Coriolis increases, and decreases as the surface stratification increases. D provides a credible indicator to estimate the thickness of the surface velocity layer.

This scaling factor is not restricted to the wind-driven flow. Its use can be expanded by recognizing that the only requirement here is a near surface along-channel geostrophic velocity U. Apply this scaling factor to Station FOC1 as observed in Wan et al. (2017) and because f and W are constant, the only relevant ratio is U/g'. In summer, g' is larger than in winter, but the near-surface along-channel estuarine velocity U in summer seems to be larger than in winter. These two competing factors lead to comparable averaged layer thicknesses at FOC1 in these two seasons: the outflow zero-crossings are at 31 m in summer and 23 m in winter. Providing $g' = 0.003$ m s^{-2} to 0.004 m s^{-2}, and $U = 0.15$ m s^{-1} to 0.2 m s^{-1} from observations, the estimated thickness for the outflow layer is in the 25 to 45 m range, which is consistent with the observed outflow layer thicknesses in Wan et al. (2017). In the 2 km wide Reloncavi fjord, the surface layer thickness defined by density is less than 4 m but the outflow layer extends to 8 m (Valle-Levinson et al., 2007). Estuario Reloncaví, which is 55 km long, 3 km wide, about 200 m deep with a sill at 150 m, has a strong stratified surface layer (Valle-Levinson et al., 2007). The surface salinity increases from 17 to 30 within the top 4 m, and the surface layer lays above a homogeneous deep water layer. The sub-tidal velocity shows a 3-layer system where the surface layer is an 8 m thick outflow layer. The 3-layer pattern was suggested to attribute to a non-linear tidal residual flow in Valle-Levinson et al. (2007). While their theory is not tested for Douglas Channel and cannot be rejected, here we are providing another possible explanation to close the gap between the hydrographic and the observed surface layer thickness in these cases.

3.5 Summary and Conclusions

This study uses an idealized 3D numerical model to study the wind-driven responses in a deep, stratified fjord off the west coast of British Columbia, Canada. An estimating parameter h_s is derived as a measure of the contribution of baroclinicity to the surface elevation tilt. Since it is sensitive to changes in surface stratification, calculation of h_s may provide a useful diagnostic tool for application with numerical models, in particular, for an operational model of Douglas Channel, monitoring elevations in

Kitimat and Hartley Bay provides a robust index to assess whether the model is maintaining a reasonable surface stratification. This is particularly important in the Kitimat fjord system as operational models are applied to support spill responses.

Modal analysis shows that even though Douglas Channel appears to be a dynamically narrow channel, it should be considered as a intermediate-width channel when studying responses close to the surface where vertical modes 2 and 3 could be more important than the first mode. Given a typical density profile in Douglas Channel, the zero-crossing of the first mode usually occurs in the middle of the water column as shown in Figure 3.13, as well as in Figure 4 of Webster (1980b) where the zero-crossing of the first mode is at about 120 m depth. Strong stratification and velocity shear in the upper 25 m favour the higher modes, and modes 2 and 3 are clearly required to represent the modelled velocity shear (Figure 14 and Table 3). Accordingly to study dynamics in fjords, including the wind influenced currents, one needs to look at higher modes to explain potentially significant cross-channel variation, even in those physically narrow fjords.

The thermal wind relation is used to study the thickness of the surface wind-driven layer, and a scaling relationship is derived for the thickness of this layer. This demonstrates the importance of rotational effects in the presence of strong stratification. As well, it provides an explanation as to why the estimated surface flow thickness in Wan et al. (2017) is smaller than the observed surface layer thickness. While the scaling factor is sensitive to choices of g', its applicability is not restricted to wind-driven flows, but also includes estuarine outflow. The results presented in this paper may help account for sub-tidal flow patterns and layer thicknesses in fjords with strong surface stratification.

Acknowledgments

Data are available upon request from the corresponding author (di.wan@dfo-mpo.gc.ca). The authors would like to thank Bodo de Lange Boom at Canadian Hydrographic Service for discussions on the tide gauge data; the officers and crew of the research vessels CCG Tully and CCG Vector for helping us with the deployment and recovery; Germaine Gatien, David Spear, Lucius Perreault, Andrew Lee and others at the Institute of Ocean Sciences who helped with the mooring work and initial data processing; Angelica Peña for ROMS discussion and questions; Jody Klymak for discussions during the earlier stages of this paper; and Richard Thomson and Pramod

Thupaki for their valuable suggestions and inputs at the later stages of this paper. This work was supported by Fisheries and Oceans Canada through the World Class Prevention, Preparedness and Response to Oil Spills from Ships Initiative. Data are available upon request from the IOS CTD Dataset that is published on CIOOS (Canadian Integrated Ocean Observing System): `https://catalogue.cioospacific.ca/dataset/d98c6fb7-fbdf-4430-85f2-1472c9be3b9a` or from the corresponding author (DiWan@uvic.ca or Di.Wan@dfo-mpo.gc.ca).

Chapter 4

Remote coastal trapped waves drive seasonal and intraseasonal variations in upwelling off the coast of British Columbia

4.1 Introduction

The physical oceanography of British Columbia (BC) coastal waters has been studied extensively over the past several decades. Intense southerly winds in winter produce strong downwelling of relatively warm, low salinity water along the outer coast, while moderately strong northerly winds in summer produce upwelling of relatively cold, high salinity water with high nutrient and low oxygen concentrations over the inner slope and outer shelf (Crawford and Thomson, 1991; Thomson and Krassovski, 2010). Thomson and Ware (1996) and Hickey and Banas (2008) showed that the spring transition off the BC coast, defined as the time when the upper ocean currents over the shelf break switch from mainly poleward to mainly equatorward, occurs before the west coast of Vancouver Island winds change direction. The enhanced supply of nutrients to the waters off the west coast of Vancouver Island is thought to originate with poleward transport by the California Undercurrent, a part of which enters Juan de Fuca Strait off northern Washington and is then incorporated into the estuarine-driven outflow from the mouth of the Strait and then transported poleward within the Vancouver Island Coastal Current (Crawford and Dewey, 1989; Thomson et al.,

1986; MacKas et al., 1987; Davis et al., 2014). Ware and Thomson (2005) examined the distribution of sea surface chlorophyll from California to Alaska and showed that the broad southern BC shelf had the highest average chlorophyll-a values but that the upwelling season, as defined by the local alongshore winds, was of shorter duration and less intense than to the south. As a consequence. local winds did not appear to be the primary factor driving the upwelling that brings nutrients up from depth to support the primary production on the west coast of Vancouver Island.

The prevailing winds from the north in summer are typically of weak to moderate strength, whereby the persistent summer upwelling and associated onshore transport of low oxygen events onto the shelf, are generally believed to be due to the relaxation of the more pronounced winter downwelling (Crawford et al., 2007). Few studies have attempted to connect upwelling on the BC shelf with remote forcing from the south. In an early study of the relationship between sea level and winds in summer along the west coast from California to BC, Halliwell and Allen (1984) concluded that the local wind stress was too weak to cause the observed sea level fluctuations and thus the sea level variation observed in BC was free wave energy propagated from the California and Oregon region (39°N to 45°N). Based on numerical simulations, Masson and Fine (2012) showed that both local and remote forcing contributed importantly to the seasonal coastal circulation variability off the BC coast. Based on observed currents at the outer edge of the Vancouver Island shelf (A1 mooring at 48.54°N, 126.19°W), Thomson and Krassovski (2010) showed that velocity fluctuations in the California Undercurrent (CUC) off BC are driven by winds along the southern Oregon-northern California coast, with peak coherence between alongshore currents at A1 and alongshore wind stress occurring at "synoptic" (10–40 day) periods. The undercurrent lag of 3 $\pm$2 days relative to the winds at Cape Blanco (42.8°N) within the synoptic frequency band is consistent with low mode poleward propagating oscillations. Using the same data from A1, Engida et al. (2016) showed that velocity fluctuations at 30, 100 and 175 m, with periods of roughly 5–25 days, were largely forced by wind-driven variability as far south as 36°N, with peak current-wind coherence for alongshore winds between 42.8°N and 47°N. The phase lags were consistent with coastal trapped waves. Enfield and Allen (1980) studied the sea surface heights and temperature along the eastern Pacific coast from 33°S to 59°N using lagged correlation analysis and estimated poleward propagating waves travelling at speeds of 180$\pm$100 km day^{-1} (2.08 ± 1.15 m s^{-1}). The general consensus, based on these studies, is that lower mode coastal trapped waves (CTWs) are likely responsible for the current variations

off the Washington and southern Vancouver Island coasts (Battisti and Hickey, 1984; Connolly et al., 2014).

CTWs are sub-inertial oscillations that are trapped over continental margins under the influence of the topographic slope, stratification and the Coriolis effect (Brink, 1991; Inall et al., 2015). These sub-inertial waves travel along the coast with the continental shelf on the right (left) in the northern (southern) hemisphere and represent a hybrid combination of internal Kelvin waves (baroclinic limit) and continental shelf waves (barotropic limit) depending on the shelf slope and stratification (Wang and Mooers, 1976; Inall et al., 2015; de Freitas et al., 2021). Thus, the common oceanographic distinction between barotropic motions (e.g., density-independent sea level fluctuations) and baroclinic motions (density-effected perturbations) is not applicable.

Coastal trapped waves provide an important mechanism for the transfer of energy from the atmosphere to the oceans as they are capable of propagating energy over long distances along continental margins (Brink, 1991; de Freitas et al., 2021). CTWs are generated by mid-latitude atmospheric forcing (Mysak, 1980) and tidal currents (Crawford and Thomson, 1984; Cummins et al., 2000), or as extensions of equatorially forced Kelvin waves that turn poleward upon encountering continental boundaries (Pietri et al., 2014). The waves are closely related to quasi-biweekly (QBW) oscillations, which are important oceanic motions generated by tropical and subtropical weather systems (Kikuchi and Wang, 2009; Miyama et al., 2006). Links between QBW oscillations and CTWs have been identified in many regions of the ocean, including the Bay of Bengal (Anup et al., 2021) and the Gulf of Guinea (Vangriesheim et al., 2005). The high energy frequency bands reported in Thomson and Krassovski (2010) and Engida et al. (2016) contain this quasi-biweekly band. However, these studies did not associated the observed motions on the BC shelf with QBW oscillations.

Given that motions linked to CTWs are coherent across continental margins (Hickey et al., 2016), their presence over the upper continental slope makes it reasonable to expect remotely forced CTWs to be present on the BC shelf. However, there has not been an examination of remotely forced CTWs on the BC shelf. To the south, Battisti and Hickey (1984), Hickey et al. (2016), and others have shown that the subtidal velocity fluctuations on the continental shelf off Washington State have a large component forced by CTWs, caused by along-shelf winds much further to the south. We note that Battisti and Hickey (1984) refer to winds within 600 km to the south as local winds in the winter.

Here, our focus is on the inner Vancouver Island shelf where an increase in water density provides a mechanism for deep water renewal in the adjoining inlets and fjords at least as far north as Douglas Channel (Thomson et al., 2017; Wan et al., 2017; Jackson et al., 2021). Density in the lower layer of the water column is used as a proxy for upwelling. The upwelled water is generally cooler and higher in nutrients, but lower in oxygen than the water it displaces on the shelf. However, oxygen concentrations are often higher than the near-bottom values in the inlets, and so annual renewal can increase near-bottom oxygen in deep basins (Thomson and Davis, 2017; Pawlowicz, 2017). These renewal events are the key to reoxygenation of the deep basins of the inlets.

The objective of this study is to examine the remote influence of upwelling-/downwelling events on the continental shelf of BC coast. We present evidence that CTWs generated by alongshore winds along the southern Oregon and northern California coasts, and even as far south as the equatorial Pacific, drive upwelling processes on the BC shelf within the quasi-biweekly and intraseasonal frequency bands.

4.2 Data

Since the early 1980s, an oceanographic mooring has been maintained at location E01 [49.29°N, 126.60°W, Figure 4.1, Thomson and Davis (2017)] in 90 m of water off the west coast of Vancouver Island. Temperature and salinity have been measured most consistently at depths of 35 m and 75 m. This paper focuses on the period from 2008 to 2013, which used modern instruments and was relatively free of data gaps. The sampling interval over this period ranges from 10 minutes to 3 hours, depending on the type of instrument and its settings . We processed the time series using a low-pass Godin filter, in which three consecutive moving averages with widths of 24, 24, and 25 hours were applied (Godin, 1972; Thomson and Emery, 2014) to remove high frequency signals and tides. The filtered time series were then re-sampled to daily intervals.

The daily upwelling index (Bakun, 1973, 1975) values have been downloaded from the Environmental Research Division (ERD) with NOAA Fisheries - Southwest Fisheries Science Center. The index is the daily average of the of the cross-shore, wind-driven Ekman transport computed from FNMOC (U.S. Navy Fleet Numerical Meterological and Oceanographic Center) six-hourly surface pressure analyses (`https://oceanview.pfeg.noaa.gov/products/upwelling/dnld`).

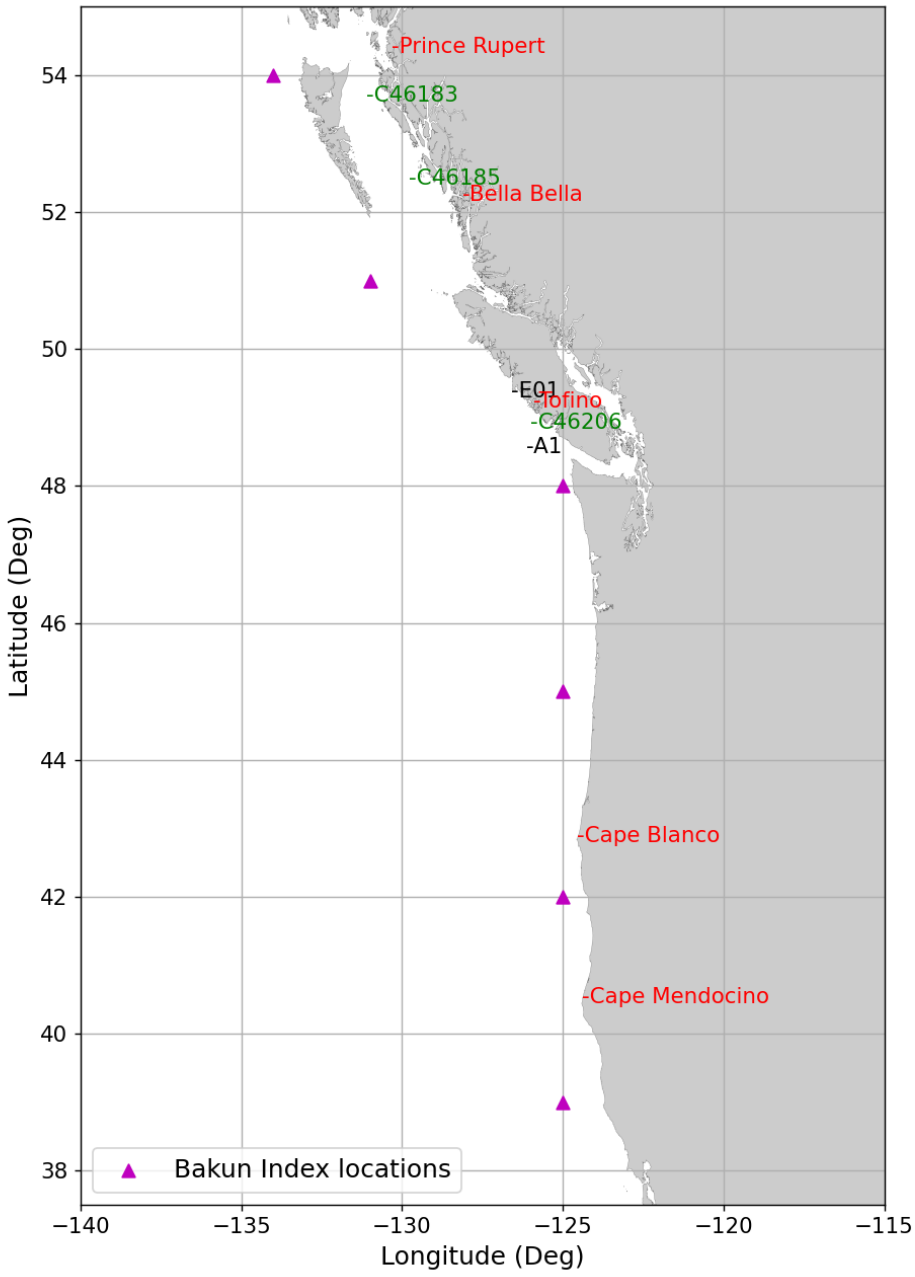

Figure 4.1: Map showing the locations of meteorological and oceanographic observation sites mentioned in this study.

Hourly sea-surface height (SSH) data are obtained from the Canadian Hydrographic Services at two coastal stations: Tofino (49.15°N, 125.92°W) and Bella Bella (52.17°N, 128.13°W). A Godin filter (Godin, 1972) is applied to the hourly data to remove the tidal and higher frequency signals, and the data are then re-sampled to daily values. Inverse barometer corrections are applied to the sea-surface elevation data using air pressure measured at two weather buoys: C46206 (for the Tofino SSH) and C46185 (for the Bella Bella SSH) (Figure 4.1, `https://catalogue.cioospacific.ca/dataset/ca-cioos_ae6d17ac-c26c-4b96-8c3c-b795545ebc67?local=en`.). The root-mean-square (rms) amplitude of the inverse barometer corrections is 0.07 m for both stations, which is $< 4\%$ of the rms amplitude for the corresponding SSHs after low-pass filtering.

4.3 Results

4.3.1 Linear regression of E01 density and upwelling indices

The seasonal cycle of water properties at E01 at 75 m depth is similar to other sites along the west coast of BC, with salinity higher in summer than in winter and temperature higher in winter than in summer (Figure 4.2*a*). The density difference between waters at 35 and 75 m depth at the E01 location is greater in summer than in winter, indicating there is more mixing in winter but that the water column it is not fully mixed (4.2*c*). The Bakun indices at 39°N and 48°N (Figure 4.2*b*) show persistent downwelling values in winter. Upwelling values at 39°N are high in summer, but almost zero at 48°N. Density variations off the BC coast are thought to be linked to the downwelling and upwelling processes (Thomson and Krassovski, 2010; Hickey et al., 2016) along the shelf. Finding the correlation between upwelling indices and E01 water density is a natural start when searching for the dominant drivers of the density variability. The overall correlations between the low-passed daily density at E01 at 75 m depth and the upwelling indices at three different latitudes (39°N, 48°N, and 51°N) are shown in Figure 4.3. The correlation reaches a maximum when the indices are shifted by +2 days for 48°N and 51°N, and shifted by 3 days for 39°N. In other words, the bottom density at E01 lags the upwelling indices by 2 days at 48°N and 51°N, and 3 days at 39°N. The clearly defined peaks in the correlation function indicate that the values are above background noise correlation. The relatively slow drop in all three correlations between the peaks and 75 days suggests there is a broad

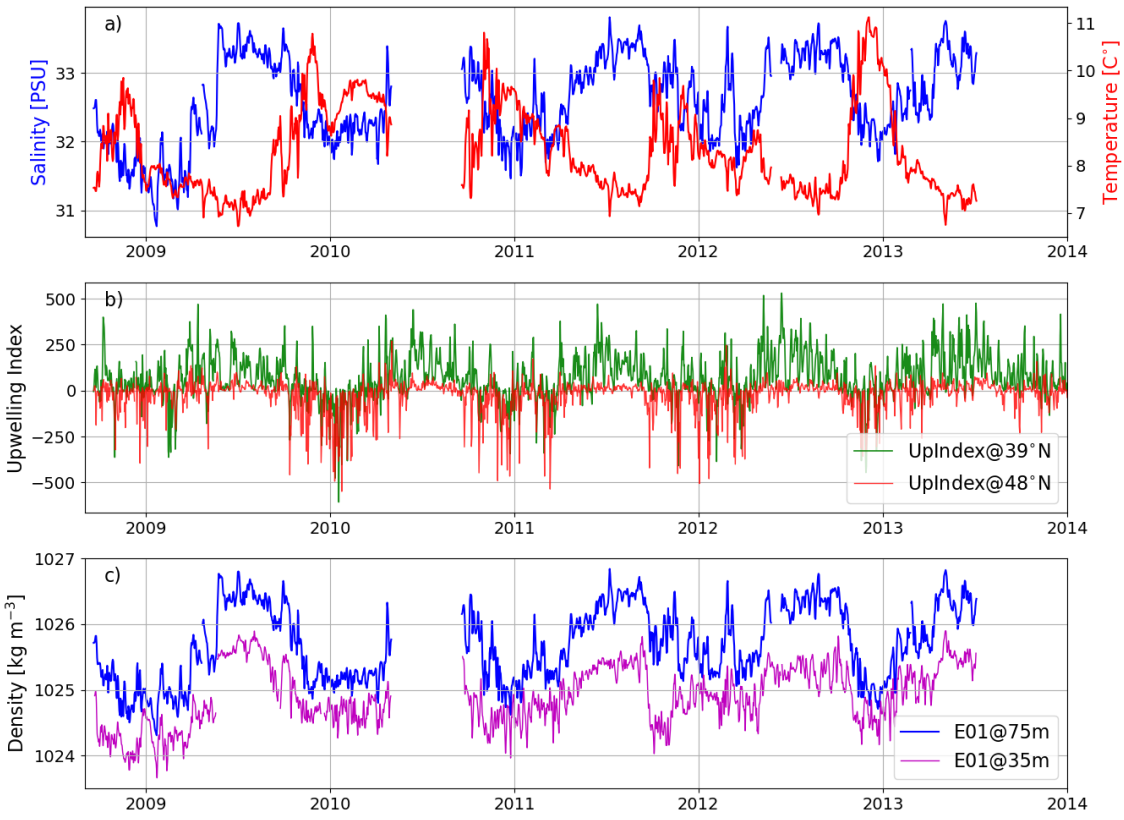

Figure 4.2: a) Time series of salinity and temperature at E01 at 75 m depth. b) Density time series of E01 at 75 m and the Bakun indices at 39°N and 48°N. c) Density time series of E01 at 35 m and 75 m.

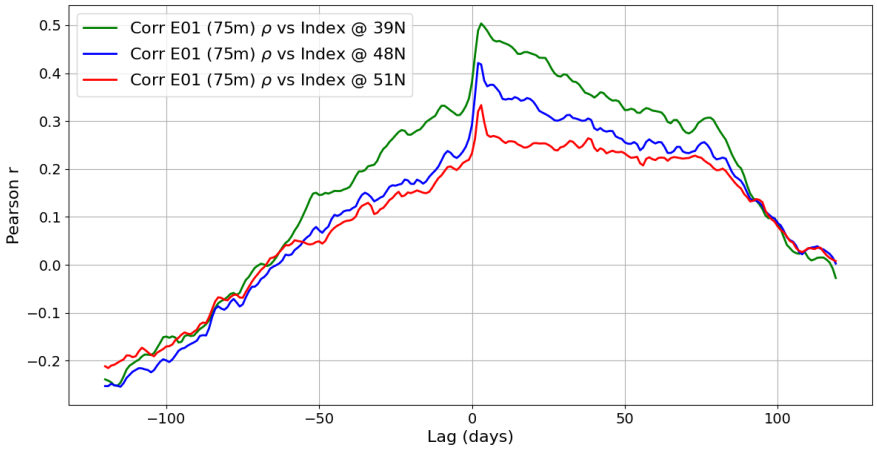

Figure 4.3: Lagged correlations between the low-passed density at E01 at 75 m and upwelling indices at three latitudes. Positive lag is for Bakun index leading.

correlation between the density at E01 and the Bakun indices between 2 (or 3 for 39°N) to the 75 day period. From here on, only 75 m depth density is considered as the 75 m and the 35 m density time series track each other and the deep density is less likely influenced by the surface dynamics, such as local wind mixing, and more representative of the deep renewal process.

The power spectral density for the E01 density time series (Figure 4.4) reveals that the variations roughly follow a red-noise frequency distribution ($1/f^2$ noted on the plot), characteristic of oceanic fluctuations caused by atmospheric forcing (Di Lorenzo and Ohman, 2013). There are discernible spectral peaks around 0.1 cpd (10-day period) and at lower frequencies.

Linear regressions are used next to explore whether E01 density can be predicted from the upwelling indices. Linear regressions show that the deep density at E01 correlates slightly better with the upwelling indices at 39°N than 48°N and 51°N (Figure 4.5 and Table 4.1). While the root-mean-square error (rmse) are similar for all regressions, the upwelling index at 39°N visibly captures the variability better than at 48°N in summer months. The 'local' winds (48°N and 51°N) do not provide enough variability in the summer months, so they cannot capture the higher summer values in density. The rmse is 0.42 kg m^{-3} when we use all indices as dependent variables for the prediction (figure not shown). Furthermore, these results do not improve significantly if winter and summer values are calculated separately. To put these rmse values in perspective, the rmse found when using the mean density to

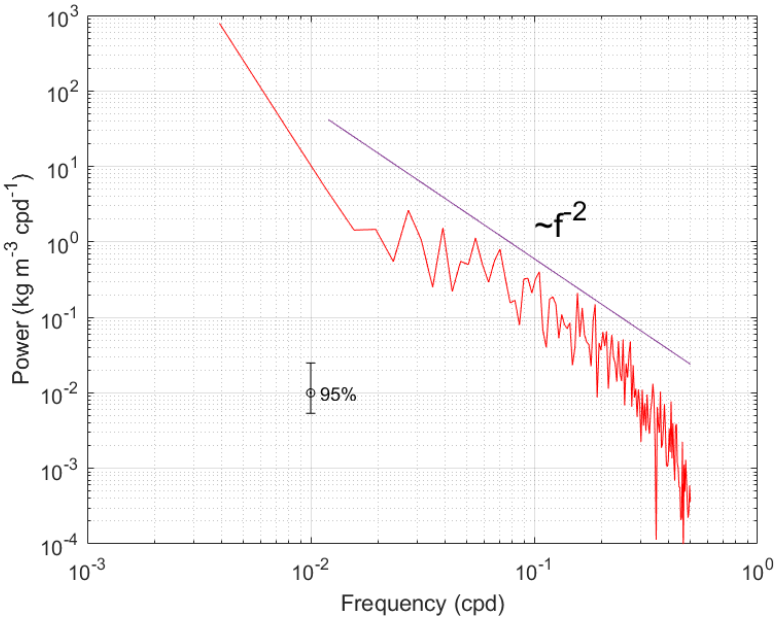

Figure 4.4: Power spectral density of E01 density with 95% confidence intervals. Note that the M2 and K1 tidal components are at the right end of the curve where it drops from f^{-1} trend.

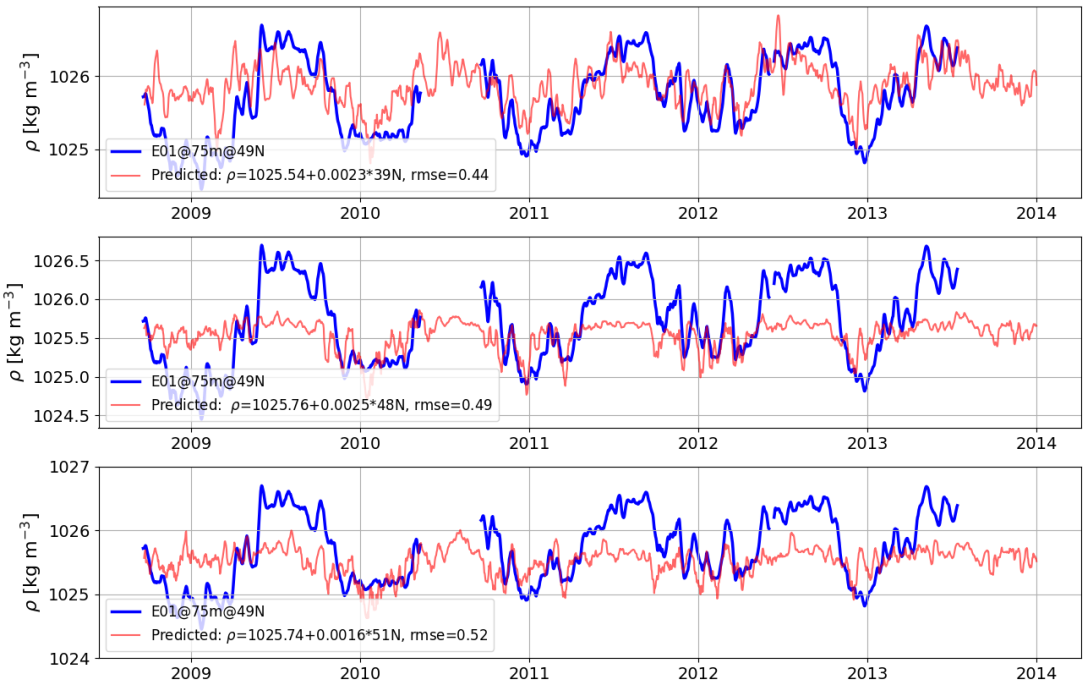

Figure 4.5: Linear regression results between the 10-day averaged density at E01 (75 m) and the 10-day averaged upwelling indices.

predict the variability (persistence) is about 0.55 kg m^{-3}. These high rmse values are consistent with the correlation results. The best correlation (Bakun index at 39°N) only captures 25% of the variance.

The wind stress at all three locations are highly correlated and so linear regression alone would not be able to separate the relative importance. Furthermore, density and wind time series are not stationary, having no consistent amplitudes and phases. Therefore, we use wavelet analysis to expand the analysis to frequency-time space in order to explore the links between the density and wind forcing within different frequency bands at different locations.

Table 4.1: Linear regression results (summary of Figure 4.5). The 'rmse' is the root-mean-square errors of the prediction.

Index intercept	slope [kg m^{-3}]	rmse [kg m^{-3}]
39°N	0.0023	0.44
48°N	0.0025	0.49
51°N	0.0018	0.52

4.3.2 Analysis of E01 density and upwelling indices in frequency-time space

The analysis in frequency-time space is based on continuous daily data from 2010-09-19 to 2013-05-01 (956 days). A 19-day gap from 2012-05-25 to 2012-06-13 and a 1-day gap on 2013-02-25 were filled using linear interpolation. We note that the analysis-period spans a transition period from the El Niño period of 2009/2010 to the La Niña conditions of 2010/2012.

As a start, we look at the wavelet coherence between variations in water density at E01 and variations in the Bakun indices at different latitudes, from 21°N to 54°N. Results (Figures 4.6 and 4.7) show that: (a) the overall coherence magnitude is relatively low for latitudes between 21°N to 33°N but increases from 36°N northward, and then drops again starting from 51°N; (b) within the 'weather band' (< 8 days), the coherence is highest with the local wind stress (45°N to 48°N), indicating that local winds play an important role in the weather band upwelling and downwelling dynamics; (c) strong intermittent events are associated with the QBW band (periods, 12 to 20 days) in all coherence plots. Although the duration of the QBW events varies, the events tend to last for about 50 to 100 days; and (d) at the seasonal scale, high coherence is found starting from 36°N and increases until 48°N.

Note that the green and yellow colours in the wavelet coherence squared plots indicate that r^2 values are larger than 0.5. Nonetheless, some of the regions that lie outside the 95% significance level still have a high coherence level relative to background values.

Spatial variations in the time-averaged coherence amplitudes are plotted in Figure 4.8. Within the weather band, the squared coherence values are slightly higher at 48°N and decrease gradually to the south and north. Within the QBW band, there are two high coherence regions: 39°N to 48°N and 24°N to 27°N. Within the intraseasonal band (50–130 day), high coherence is found between latitudes 36°N to 48°N.

The above results suggest that there is a regime change in the wind stress at around 39°N, which is where the wind stress transitions from seasonally varying between upwelling and downwelling favourable (39°N) to permanently upwelling favourable (36°N) [Figure 1b in Hickey et al. (2016)]. Wavelet coherence between wind stress records from 48°N and other latitudes (Figure 4.9) reveals generally high values between 39°N and 48°N and low coherence for other latitudes, suggesting the coastal ocean is forced coherently by the alongshore winds within this latitudinal band.

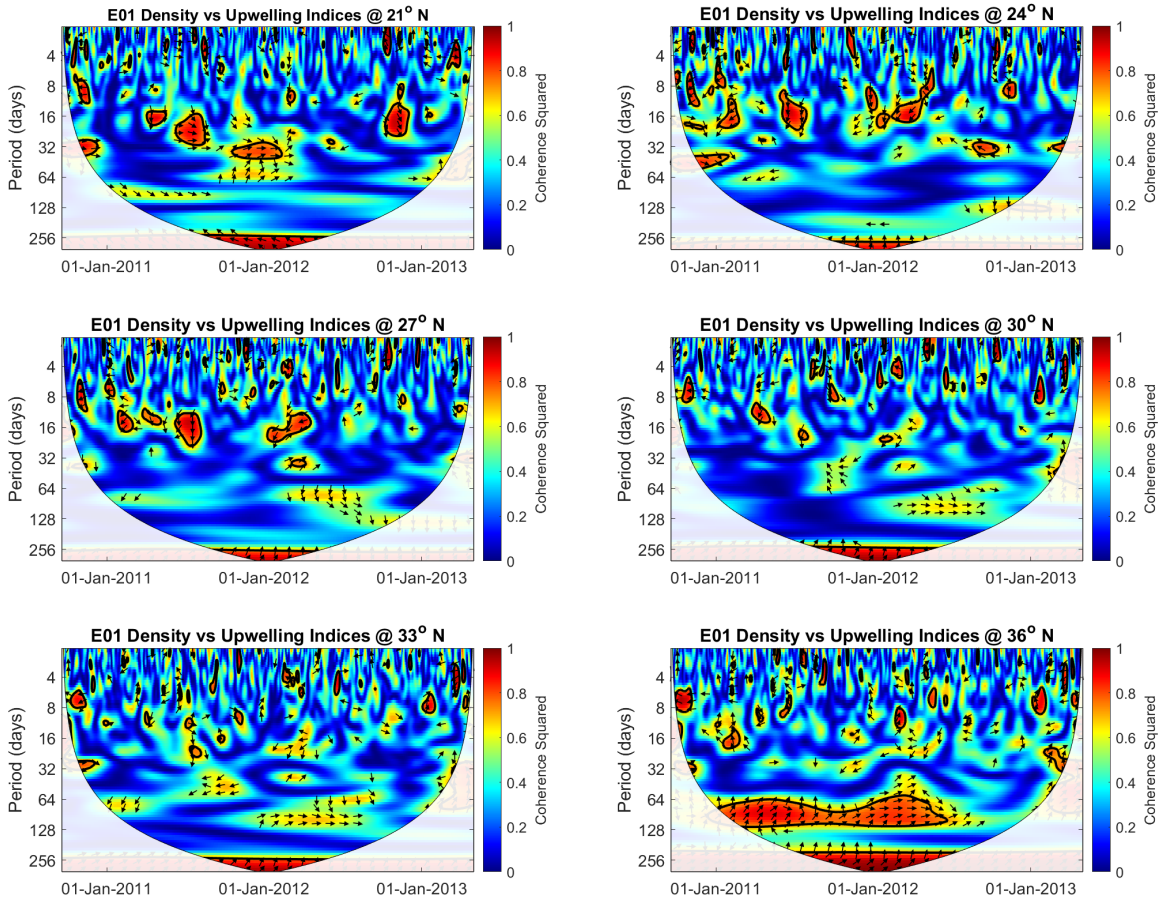

Figure 4.6: Wavelet coherence amplitude-squared between the E01 (75 m) water density and Bakun upwelling indices from 21°N to 36°N. The values encompassed by the black lines are the squared coherence values exceed the 95% confidence interval. The arrows in the figure shows the phase angle: pointing right indicates 0° lag, and pointing upward (downward) indicates density lagging (leading) wind by 90°. The arrows are only plotted where the coherence squared values exceed 0.5 (roughly at the 95% level).

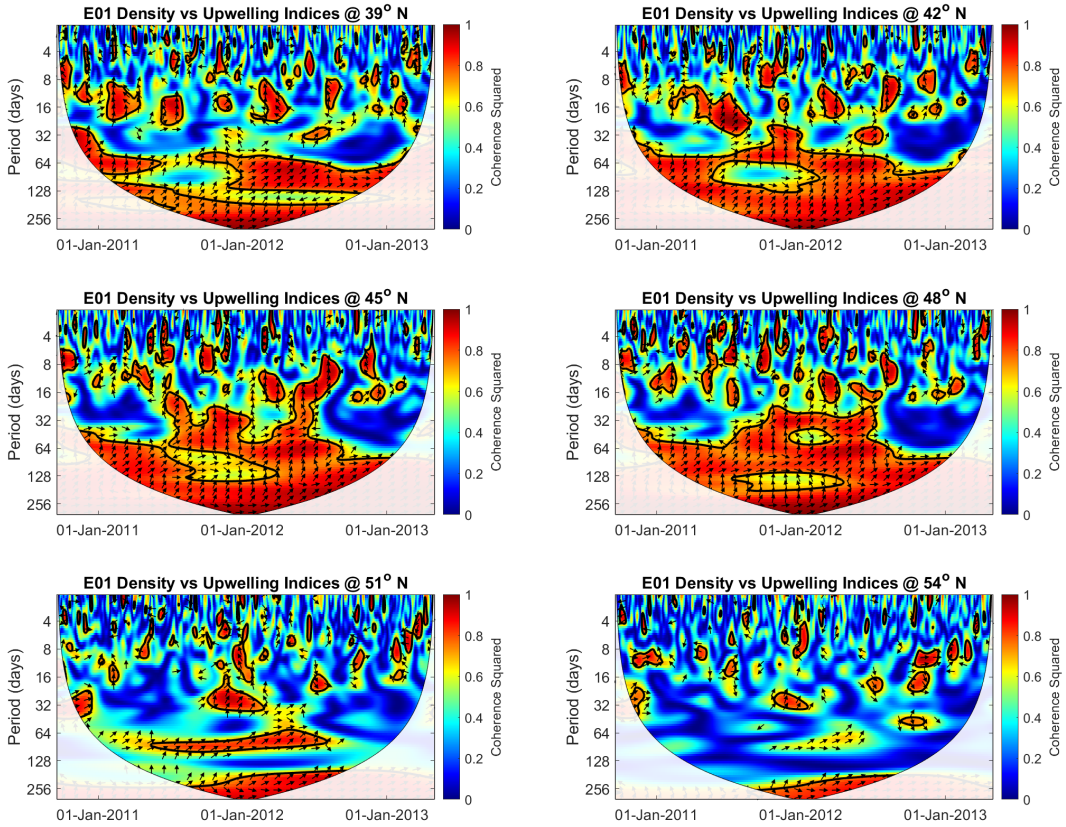

Figure 4.7: Wavelet coherence amplitude squared between the E01 (75 m) density and Bakun upwelling indices from 39°N to 54°N. The values encompassed by the black lines are where the confidence interval exceed the 95% confidence interval. The arrows in the figure shows the phase angle: pointing right indicates 0° lag, and pointing upward (downward) indicates density lagging (leading) wind by 90°. The arrows are only showing where the coherence squared values exceed 0.5 (roughly at at 95% level).

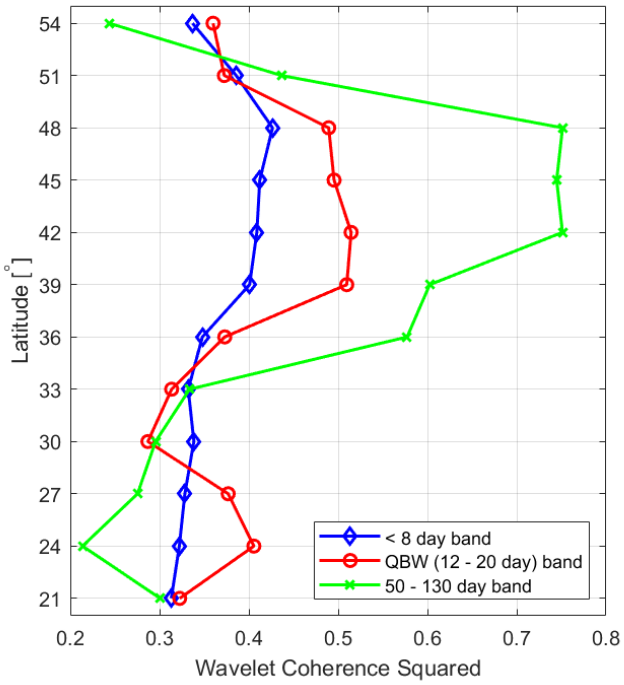

Figure 4.8: Temporally averaged wavelet coherence squared for Figures 4.6 and 4.7. The squared coherences are averaged over the entire time period of 2010 to 2013. Note that E01 is at 49.3°N

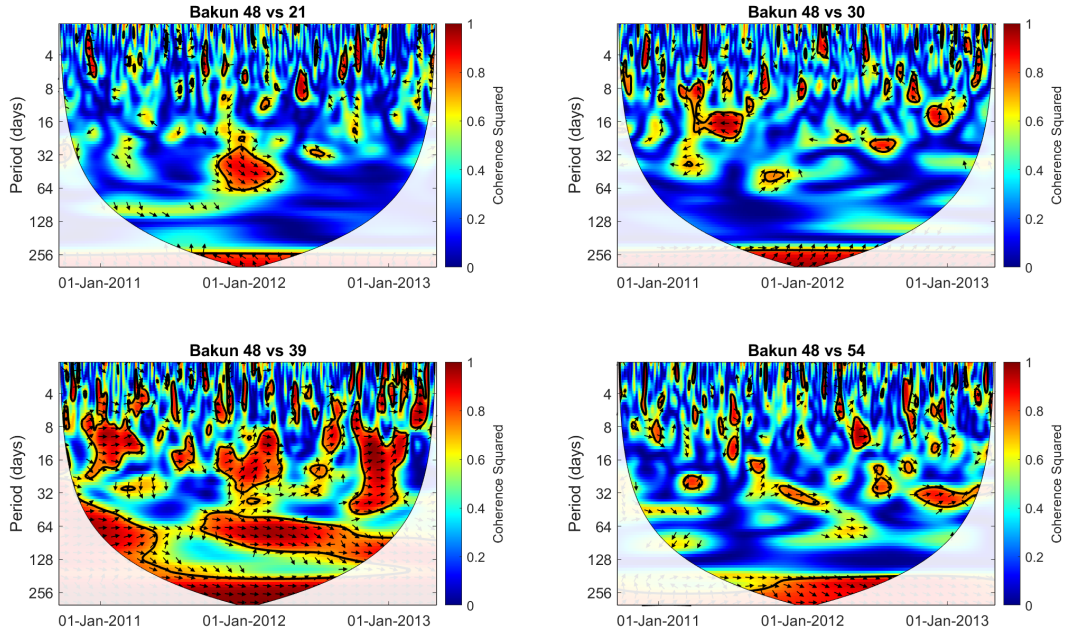

Figure 4.9: Wavelet coherence amplitude squared between 48°N and other latitudes. The values in the black lines are where the confidence interval exceed 95%. The arrows in the figure shows the phase angle: pointing right indicates 0° lag, and pointing upward (downward) indicates Bakun index at 48°N lagging (leading) the other index by 90°. The arrows are only showing where the coherence squared values exceed 0.5 (roughly at 95% level).

4.3.3 Sea surface height variability

The notion that CTWs are partially responsible for sea level variability along the Washington, Oregon and BC coasts was advanced by Halliwell and Allen (1984). In their study, the authors used empirical orthogonal function (EOF) analysis to conclude that most of the sea-surface height (SSH) variance along this region of the coast is due to remote wind forcing originating off northern California. In particular, they state "Local forcing was so weak along the British Columbia coast that ζ (sea levels) fluctuations were apparently dominated by free wave energy propagating poleward from the northern forcing region". The northern forcing region referred to is the northern California and Oregon coasts (roughly 40°N and 46°N). Battisti and Hickey (1984) found that CTWs generated off California propagate poleward along the west coast to Oregon and Washington during summer, but the winter subsurface pressure response is mostly dominated by local (up to 600 km) wind stress. The 'southern forcing region' corresponds to the secondary maximum in QBW coherence in Figure 4.8. These studies used relatively short periods of data [two summers for Halliwell and Allen (1984) and three segments of less than 40 day periods for Battisti and Hickey (1984)].

We performed wavelet coherence analysis between the low-pass filtered sea levels at Tofino (49.15°N, 125.92°W) and Bella Bella (52.17° N, 128.13°W), Bakun indices from 39°N to 48°N, and water density at E01 at 75 m depth. The wavelet coherence in SSH between Tofino and Bella Bella was first examined for any signal propagating from south to north (Figure 4.10). In general, the two series are coherent at all frequencies examined. Within the weather (< 8 day) band, the two signals are highly coherent and largely in-phase. Within the QBW (8 to 20 day) band, a relatively consistent phase lag is observed (Bella Bella lags Tofino by about 2 days). The coherence is higher in winter, when we expect more uniform winds along the coast. From the phase lag, we estimate that the CTWs are travelling at roughly 200 km day^{-1} (2.3 m s^{-1}) from Tofino to Bella Bella (about 400 km). At the intraseasonal and seasonal scale, the two SSH signals are essentially highly coherent and in-phase.

To better understand the roles barotropic and baroclinic motions in upwelling variability on BC coast, we examined the coherence between sea levels and the upwelling indices and the density variations. In Figure 4.11, the top four panels show the coherence between the SSHs and the Bakun indices at 39°N and 48°N. The SSHs and the upwelling indices are generally 180° out-of-phase, as expected (i.e. strong

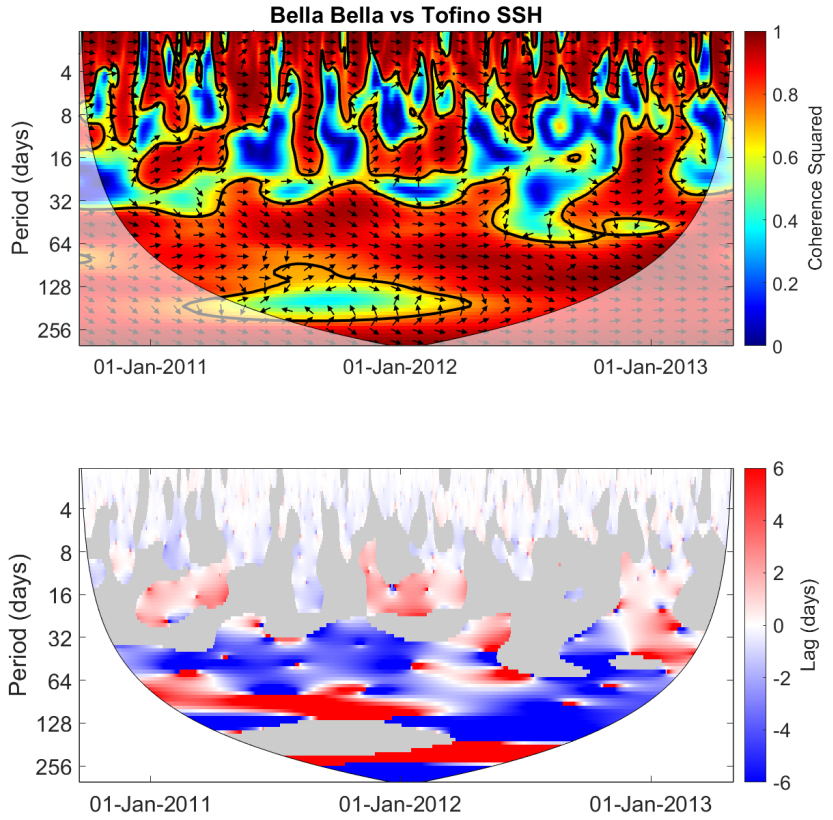

Figure 4.10: Wavelet coherence amplitude squared between SSHs at Tofino (49.15°N, 125.92°W) and Bella Bella (52.17° N, 128.13°W). The values encompassed by the black lines exceed the 95% confidence interval. The arrows in the figure shows the phase angle: pointing right indicates 0° lag, and pointing upward (downward) indicates Bella Bella SSH lagging (leading) Tofino by 90°. The arrows are only showing where the coherence squared values exceed 0.5 (roughly at the 95% level). The bottom panel shows the phase lag where the coherence squared exceeds the 95% confidence level. The phases are converted to time values, i.e. Bella Bella lagging Tofino by 90° at a 12-day period indicates a time lag of 3 days. Negative phases mean Bella Bella leads.

upwelling-favourable winds are associated with low SSHs). The coherence with the Bakun Indices in the < 8 day band are generally low for both Tofino and Bella Bella as shown in Figure 4.11, indicating the along-shelf wind stress is probably not the key factor determining the SSHs within weather band. As with the previous panels (Tofino vs Bella Bella SSHs), the QBW (8 to 20 day) band, shows intermittent highly coherent events in all four plots that tend to be more intense in winter. At intraseasonal time scales, there appears to be a high coherent band in all four plots for periods of 50 to 130 days. The bottom two panels in Figure 4.11 show the coherence between SSHs and the E01 (75 m) water density, which are generally out of phase. Noteworthy, is the observation that the coherence between SSH and E01 density is not significant in either the weather band or the QBW band, and only highly coherent at the intraseasonal and seasonal bands. Because SSH is a measure of both barotropic and baroclinic motions, The low coherence between Tofino SSH and the E01 density (75 m) at the sub-intraseasonal scales suggests that the SSH signal at Tofino is not just a reflection of the adjusted subsurface isopycnal change, but it represents the barotropic motion that can be connected through remote and local forcing, such as wind stress. Another possible reason why there is low coherence between SSH and the E01 (75 m) density is that local freshwater runoff may be affecting SSHs at Tofino and Bella Bella, but not water density in the offshore region.

4.4 Discussion

Even though our interest is in the driving mechanisms of the water property variation on the BC shelf rather than the CTWs themselves, we use the CTW formulation (Wang and Mooers, 1976; Brink, 1991) to explain the results we presented here.
The linearized density perturbation is given by:

$$\frac{\partial \rho'}{\partial t} + w\frac{\partial \bar{\rho}}{\partial z} = 0 \tag{4.1}$$

where t is time, z is the vertical coordinate, and w is the vertical velocity, density, ρ, is written as the sum of the background density ρ_0, a depth-varying mean density $\bar{\rho}(z)$, and a density perturbation $\rho'(x, y, z, t)$. The density perturbation has the form $\rho' \sim e^{i\omega t}$, where ω is the frequency, and the perturbation equation can then be rewritten as:

$$\rho' \sim -\frac{w\frac{\partial \bar{\rho}}{\partial z}}{i\omega}, \tag{4.2}$$

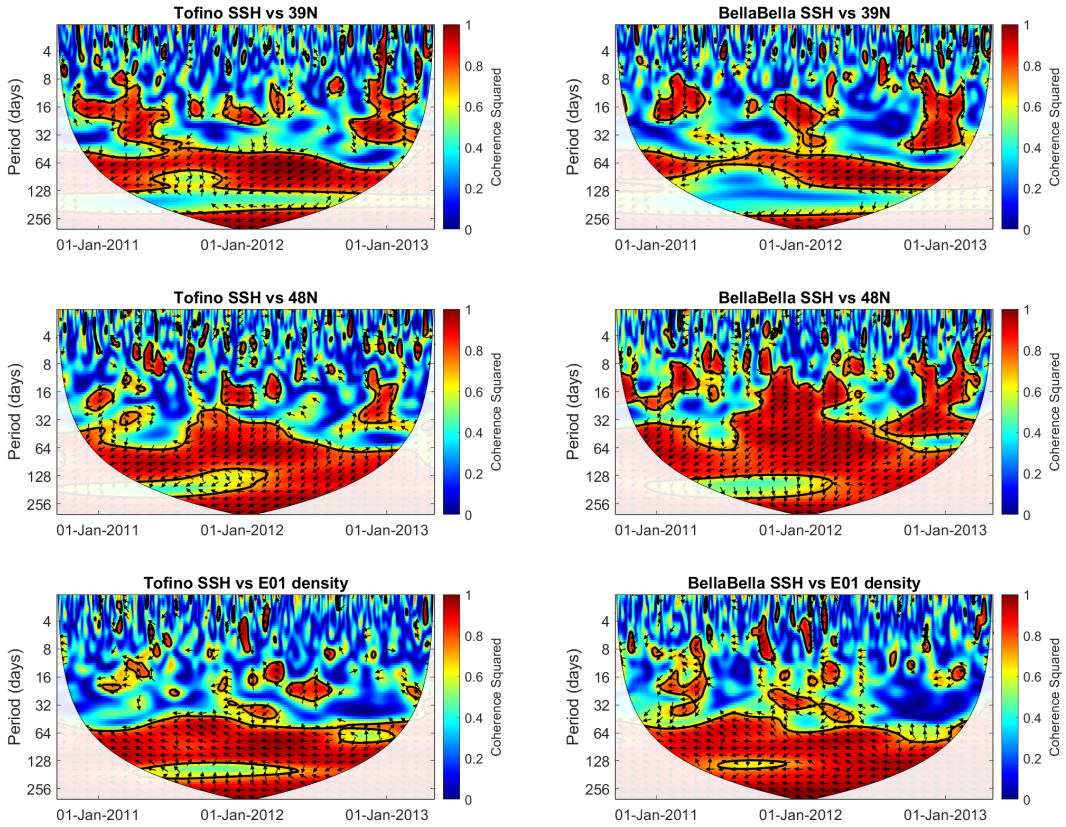

Figure 4.11: Wavelet coherence amplitude squared between SSHs at Tofino (49.15°N, 125.92°W) and Bella Bella (52.17°N, 128.13°W) and Bakun upwelling indices (top four) and E01 density (bottom two). The values encompassed by the black lines exceed the 95% confidence interval. The arrows in the figure shows the phase angle: pointing right indicates 0° lag, and pointing upward (downward) indicates SSH lagging (leading) wind (top four) or E01 density (bottom two) by 90°. The arrows are only showing where the coherence squared values exceed 0.5 (roughly at 95% level).

and we can see that the density perturbation is

- proportional to the vertical velocity, w,
- 90 degrees out-of-phase with changes in w, and
- proportional to stratification $\frac{\partial \bar{\rho}}{\partial z}$.

Having shown the connection between the E01 density variability, Bakun upwelling indices and sea level. We consider these results in different frequency bands to consider connections between the high coherence hot spots and potential driving forces. The first band considered is the high-frequency (¡8 days) or 'weather' band, second we consider the QBW frequency band, which is often associated with Coastally Trapped Waves (CTWs) and finally, we consider the intraseasonal band.

4.4.1 The weather band dynamics

Within the weather band (high-frequency, <8 days), we find that the near bottom water density (at 75 m depth) at E01 is slightly more coherent ($r^2 \sim 0.4$) with the local wind-stress (at 48°N) than with wind stress to the south and north ($r^2 \sim 0.3$, Figure 4.8). The density at E01 and the SSHs at Tofino and Bella Bella are mostly 180° out-of-phase with the local upwelling indices, suggesting there is almost no time lag between the SSH and the density response. The coherence values between the density at E01 (at 75 m depth) and the SSHs (Tofino and Bella Bella) are not high (around 0.4 or lower), while the values are high between the SSHs at Tofino and Bella Bella (Figures 4.10 and 4.11). Additionally, the local along-shelf wind stress is not expected to cause any significant SSH fluctuations (Halliwell and Allen, 1984). The combination of these results indicates that the driving force in this frequency band is likely caused by relatively long wavelength CTWs.

In addition to the CTWs, there is at 5-day time scales, a globally coherent response to Rossby–Haurwitz surface air pressure waves. Thomson and Fine (2021) have shown this motion through bottom pressure observations and numerical models. This could be one process that is causing the high coherence between the SSHs. Weak coherence is observed between the SSHs and the E01 density (75 m) in this high-frequency band. This decoupling between the SSHs and the density indicates there are differences in the response and the driving force between the barotropic and baroclinic motions. Thus, the sea level fluctuations arise from more than just the CTWs, whereby the barotropic and baroclinic adjustments are tightly coupled.

4.4.2 Quasi-biweekly band

The wavelet coherence plots (Figures 4.6, 4.7, 4.8 and 4.10) provided evidence of CTWs within both the QBW band and the low-frequency intraseasonal band (50–130 day band).

The QBW frequency band (periods of 12–20 days) (Kikuchi and Wang, 2009) is associated with monsoons (Keshavamurty, 1972). QBW oscillations are well known in the tropical and subtropical regions of the western Pacific, Indian Ocean and Central America (Kikuchi and Wang, 2009). Many studies have linked the SSH variation with the CTWs generated by the QBW oscillation, such as in Anup et al. (2021), and lower mode CTWs are more likely to be responsible for the current variations off the Washington and southern Vancouver Island coasts (Battisti and Hickey, 1984; Connolly et al., 2014).

The wavelet coherence analysis between SSHs at Tofino and Bella Bella (Figure 4.10) suggests waves are travelling at 2.3 m s^{-1} from Tofino to Bella Bella. This is consistent with first-mode CTWs, which have speeds of around 2–4 m s^{-1}, as summarized in Aydln and Beşiktepe (2022).

The lack of high coherence between the SSHs and the density field in the QBW-band suggest other sources for SSHs in this frequency band that are not associated with QBW band CTWs. The difference we observe could be due to the differences between barotropic and baroclinic responses. There is both barotropic and baroclinic information in the SSH signal and it is difficult to differentiate these two from our observations. Additional complications arise from the sensitivity differences between the instruments (tidal gauges versus temperature and conductivity), which determine the weaker response in the density data.

From the overall lagged correlation analysis between the upwelling indices at 39°N and the density signal at E01 (75 m), we estimate that the wave speed is roughly 400 km d^{-1} (1200 km over 3 days, 4.6 m s^{-1}). This is in agreement with the estimates using the dispersion relation. Using Estevan Point's depth and stratification presented in Figure 4.10 in Cummins et al. (2000), the phase speed is estimated to be 4.2 m s^{-1}. This is only slightly faster than other studies. Using sea level height and buoy wind data from stations between 60°N and 33°S, Enfield and Allen (1980) estimated phase speeds of 180 ± 100 km d^{-1} (2.08 ± 1.16 m s^{-1}) using correlation calculations and 60 – 100 km d^{-1} (0.69 – 1.16 m s^{-1}) using cross spectral estimates; Thomson and Krassovski (2015) estimated the CTW phase speed from Cape Blanco (Southern

Oregon) to A1 is around 300 km d^{-1} (3.47 m s^{-1}) (high frequencies, periods < 10 days) to 375 km d^{-1} (4.34 m s^{-1}); Pringle and Riser (2003) estimated a phase speed of 220 km d^{-1} (2.55 m s^{-1}) from lagged correlation analysis between winds off Baja California (31°N) and nearshore bottom (depths of 15 and 33 m) temperatures off San Diego (33°N); Engida et al. (2016) estimated 270 km d^{-1} (3.13 m s^{-1}) using coherence phases between winds off Cape Mendocino (40.44°N) and temperatures at A1 at 400 m depth. These estimates from observations are in an general agreement with CTW numerical model results, which find first and fourth mode phase speeds along the California coast of 334 km d^{-1} (3.87 m s^{-1}) and 63 km d^{-1} (0.73 m s^{-1}), respectively (Connolly et al., 2014; Hickey et al., 2016). It is the first mode of the CTWs that is most likely detected off the BC coast as higher modes are known to be dissipated along the way (Thomson and Krassovski, 2015).

From the coherence summary plot (Figure 4.8, for the 12–20 day band), we find that the high coherence region clearly coincides with the region of intraseasonal varying winds observed between Northern California (39°N) and Southern Vancouver Island (48°N), suggesting that this broad region as a forcing zone for the QBW band for E01 density variations. The duration of 50 to 100 days for each event seen in Figures 4.6 and 4.7 likely relates to the number of storms or intensified wind conditions within this coastal region. Specifically, a sequence of 3 to 5 major storms with lags of 12 to 20 days between storms could account for the observations. The intervals of roughly 60–120 days between events could be due to a beat frequency produced between the QBW band in the wind and another signal that is interfering at periods of around 24–30 days. One possible interference signal is mode-1 equatorial Kelvin wave with periods of 50–70 days. The beating between the QBW band and mode-1 equatorial Kelvin wave would produce an approximate 30-day interval. Alternatively, an atmospheric teleconnection between the equatorial and mid-latitude regions could be responsible for the mode 1 (50–70 day period) and mode 2 (90–130 day period) Kelvin waves could be causing corresponding variations in the trains of coastal storms or strengthened alongshore winds forcing the QBW motions off the west coast of North America. Further analyses and numerical modeling are required to test these hypotheses.

4.4.3 Intraseasonal (50–130 day) band

The high coherence is observed within the intraseasonal (50–130 day) band between variations in near bottom water density at E01 and SSH at Tofino and Bella Bella, as well as between variations in E01 density and Bakun indices at different latitudes along the west coast, especially between 39°N and 48°N. In searching for remote mechanisms that could be driving the subsurface density variability at E01, we consider two possibilities: the first involves CTWs that originate directly from Kelvin waves in the equatorial Pacific that turn northward along the west coast off Central America; while the second involves CTWs that are generated by the coastal winds at mid-latitude between 39°N and 48°N.

The high coherence between variations in the E01 density record and the alongshore winds between 39°N and 48°N points to the second possibility, which is that the equatorial Kelvin waves are associated with changes in the atmospheric conditions over the Eastern Pacific. This subsequently leads to an atmospheric teleconnection between the subtropical Pacific and upwelling winds off the Washington and Oregon coast. Thus, the CTWs observed off BC could be linked to equatorial dynamics through the atmosphere rather than through the ocean, as in the first proposed mechanism. A search for such an equatorial-mid latitude teleconnection is beyond the scope of this work.

In the case of equatorial Kelvin waves, the narrow ($< 5°$) equatorial belt centered at the zero of the Coriolis parameter (i.e. f = 0), serves as a waveguide for low frequency baroclinic disturbances (Gill, 1982). The trapped, non-dispersive Kelvin waves propagate eastward until they hit the eastern boundary of the ocean basin, where they split into southward and northward propagating branches. The wave energy is then transmitted poleward along the coast in the form of CTWs (Moore, 1968; Enfield and Allen, 1980; Brink, 1991; Thomson and Davis, 2017). The mode-1 (50–70 day period) and mode-2 (90–130 day period) equatorial Kelvin waves that dominate the wave guide (Cravatte et al., 2003; Mosquera-Vasquez et al., 2014) are converted to baroclinic CTWs in the subtropical region after arriving at the shelf and then transmitted poleward along the west coast of North America.

We note that both of these mechanisms could co-exist and that future numerical modelling work should be able to quantify the relative influences of the two processes.

4.4.4 Generation of CTWs

Equatorial Kelvin waves are one of the possible sources of CTWs (Moore, 1968; Enfield and Allen, 1980; Brink, 1991; Thomson and Davis, 2017). Enfield et al. (1987) showed poleward propagating waves that are not coherent with wind stress have power spectral peaks in the 1 to 2 week band during 1976-1977 and 1982-1983 El Niño events, and argued that these CTWs are of equatorial origin. More recently, Thomson and Davis (2017) found that the propagating first mode equatorial baroclinic Kelvin waves (or a mix of the first and the second modes) are responsible for the currents/sediment resuspension observed at 61 ($\pm$24) day periods at the bottom of the Middle American Trench at depths of 4300 m off Costa Rica. Our SSHs plots show high coherence in these periods; however, the mixed phase difference (Bella Bella leading Tofino in some cases in the 50 to 130 day band) suggest that local atmospheric forcing could also play an important role in this band as well, especially given the strong coherence between the SSHs and the local upwelling indices shown in Figure 4.11.

Mid-latitude coastal winds are a common forcing in CTWs forcing mechanism (Brink, 1991), in which it was suggested that the summer alongshore wind stress conditions are better for CTW generation. Results from Battisti and Hickey (1984) showed that the winter subsurface pressure response was mostly dominated by local winds along the west coast of Oregon and Washington but they mostly investigated in the 'weather' band frequency due to the lengths of the data records ($<$ 40 days). Hickey et al. (2016) argued that remote wind forcing is not as important in winter months in setting up CTWs as the coastal wind is more uniform (i.e. no along-shelf pressure gradient) along the coast in winter, which is not ideal for CTWs to be developed. Using monthly mean data, Hickey et al. (2016) showed that the year-to-year water property extremes observed at mid-shelf are highly variable and better correlated with the local wind stress in winter than summer. In our study, we do not see a significant intensification of coherence in summer; rather, we find intensified events in winter seasons in the QBW band. This winter intensification is also observed in Thomson and Krassovski (2015).

Figures 4.6 and 4.7 indicate higher and more sustained coherence in winter months. However, computing winter vs summer (modified version of Figure 4.8) did not reveal significant differences. The important difference between winter and summer is that in winter the winds are coherent along the coast and less so in summer. It is possible that the winter winds act like a line source and summer is more like a point source.

In addition to the statistical methods and differences in the length of the time series used in previous studies, difference between the summer and winter CTW responses could be due to the source of the generation. In summer, the winds along the west coast are not spatially coherent, so the generation of CTWs can be seen as coming from point sources, where the coherence is high for a particular location. For the BC coast, we see a much weaker signal after the CTWs propagate over a long distance. In winter, the winds are highly coherent along the coast, therefore acting as a line source-forcing mechanism. While it is difficult to separate the local and remote influences, the end result from a line source for CTWs could be a much stronger cumulative upwelling response along the BC coast.

4.4.5 Implications for regional numerical models

While the regional model applied by Masson and Fine (2012) did allow for remote forcing of variability along the BC coast, their analysis did not focus on the role of CTWs. Moreover, the forcing applied along the boundaries of their model was updated at monthly intervals; thus variability associated with remotely generated CTWs of quasi-biweekly periodicity was not represented in their model. The ROMS model presented by Peña et al. (2019) used SODA (Simple Ocean Data Assimilation, `https://climatedataguide.ucar.edu/climate-data/soda-simple-ocean-data-assimilation`) for their boundary forcing so they may have captured some CTWs. However, CTW was not their objective so this model results will need to be revisited. Regional numerical models on the BC coast, such as CIOPS-W (`https://catalogue.ec.gc.ca/geonetwork/oilsands/api/records/390abee6-4ba0-4d6e-ae79-25753d1c43f3`), are forced by basin-scale or global models. CIOPS-W has its southern boundary at 44°N, which is in the middle of the CTW forcing region. The model open boundary conditions (OBCs) for CIOPS-W probably were not developed or tested with CTWs in mind, thus it would not be surprising if the CTW energy from south of 44°N is missing. In addition, the model has never been evaluated for CTW propagation in the interior as far as we are aware, so the quality of the numerical representation of the dynamics is unknown. This is a relatively simple test: we could reproduce the wavelet coherence analysis (Figures 4.6 and 4.7) to compare the wavelet coherence between the model derived bottom density at E01 (at 75 m) and the winds on the coast. Additionally, it is not known whether the model that forces CIOPS-W, which is the RIOPS (Regional Ice Ocean Prediction System, `https://science.gc.ca/site/science/en/concepts/`

prediction-systems/regional-ice-ocean-prediction-system-riops), contains proper CTW energy. Moreover, the character of CTWs can vary between two limiting cases: internal Kelvin waves and continental shelf waves. Brink et al. (1992) used a stratification parameter S (Burger number) $\left(\frac{N_0 H}{fL}\right)^2$, where N_0, H, L are the typical values for the buoyancy frequency, depth, and cross-shelf length scale, to describe these two limits. Based on the calculated S along the shelf, CTWs of different properties are propagated. Numerical models will be able to help with charactering the CTWs that enters the BC shelf water. CTW testing in BC regional models is beyond the scope of the present study but is planned for the future.

4.5 Summary

This work expands the study of the processes and frequencies that influences upwelling on the BC shelf to the QBW band and the equatorial Pacific and northern California regions. This is the first study to present evidence for QBW oscillations and intraseasonal (50–130 day period) processes affecting upwelling intensity and timing on the Vancouver Island shelf. The QBW oscillations are ubiquitous elsewhere on continental shelves but have never been examined for the BC shelf. Upwelling plays an important role in the region by lifting cooler and relatively high dissolved oxygen (as compared to the bottom of adjoining inlets), nutrient-rich water onto the shelf so that it is available for deep water renewal events. The long-range connection between the BC coast and remote regions also impacts regional numerical models where the propagation of coastal trapped waves is required to accurately model sea levels, along-shore velocities, and even cross-shore velocities and water properties. Long-term variability research on BC coast needs to consider both local and remote changes.

Future work could include incorporating pressure data from different moorings, evaluating how representative of upwelling are Bakun indices are as compared with using local wind stresses and other established indices, such as $I_{35/175}$, which is based on the velocity difference between the alongshore currents at 35 m and 175 m depths at A1 (Ware and Thomson, 2005). Barotropic and baroclinic motions, and the origins of CTWs can be examined more closely with numerical models by running experiments with different stratification conditions. Direct tests of the propagation of CTWs should be performed for the models that force regional models to ensure the CTW dynamics are properly captured. Given that the 2011 La Niña is one of the strongest

on record (Boening et al., 2012), it is important to quantify the effect of the La Niña conditions on the results of this study. Furthermore, connections between CTWs on the BC coast and the El Niño and La Niña events should be studied to better understand the effects of remote events on the variability on the BC coast.

Chapter 5

Conclusion

The primary objective of this thesis was to gain an improved understanding of the circulation and the deep water renewals in Douglas Channel, British Columbia, Canada. In this thesis, I analyzed observations of current velocities and considered their connections to wind forcing, and determined that the overall circulation in Douglas Channel is a mixture of estuarine flow, wind-driven flow, and the barotropic and baroclinic responses to changes to the surface pressure gradients.

For the sub-tidal circulation in the along-channel direction, a three-layer structure is found in winters and a four-layer structure in summers due to deep water renewals. The multi-layer current structure provides direct evidence showing that the deep basin water is renewed every summer and the multi-layer structure directly supports previous studies, for example, Gardner (1982) who hypothesized that deep water intrusion must have happened between April and November 1977 due to the otherwise unexplained increase in three copepod species. A wind-driven response in the current velocity is observed not only at the surface but even at 150 m depth in a counter-wind direction. Further studies of the wind-driven response in the channel for this thesis follow naturally.

The intention of studying the wind-driven circulation was to validate the hypothesis that the mid-depth counter-wind velocity currents were caused by the along-channel barotropic and baroclinic pressure gradients. By analysing results from a numerical model with an idealized configuration representing Douglas Channel, it was found that this physically narrow channel, which is also considered as dynamically narrow (its width is smaller than the first mode Rossby radius), is actually dynamically wide. The cross-channel geostrophic balance dictates the along-channel velocity layer thicknesses and directions. A surface stratification and the existence

of a current velocity at the surface are the only conditions required to reach this conclusion. This allowed me to expand this conclusion to other flows at the surface of fjords, such as the estuarine circulation's outflowing layer, and finally to provide a possibly answer to address an important but unanswered question: why is the surface outflowing layer thicker than the stratified layer depth? The thickness of the surface outflowing layer should also consider the cross-channel dynamics given surface high stratification. A re-examination is needed for other similar fjords to help explain the thicknesses of their outflowing layers.

Douglas Channel is well connected with the rest of the Kitimat fjord system. Webster (1980b) noted that the head of the fjord system is not the Kitimat River at the head of Douglas Channel but the mouth of the Kitlope River at the head of Gardner Canal. The interpretation of the volume and salt transports in Douglas Channel analyzed in this thesis requires an understanding of the partitioning of the freshwater leaving Gardner Canal between the two potential outflow pathways: Verney Passage and Douglas Channel. This partitioning was not addressed by the mooring program discussed here and the origin of the volume imbalance observed in Douglas Channel remains an open question. Following this, the later study done by Shan et al. (2019) confirmed the volume flux shown in Wan et al. (2017) using numerical model results.

Douglas Channel is well connected with the neighbouring continental shelf. In the winter the connection is through the upper estuarine circulation and in the summer it is through the estuarine circulation and the deep renewal events. Changes in the shelf water properties and biota should be expected to appear in Douglas Channel within a season or so. In addition, any changes in the timing of the regional transitions between upwelling and downwelling regimes should be expected to have an immediate impact on the timing of the renewal

During the study of the renewal events, the search for the source of the dense water on the continental shelf of BC connected the variation of this channel with the variation on the northern California coast and even in the equatorial regions. Evidence of coastal trapped waves was presented from the density time series at the bottom of E01 and the sea levels at Tofino and Bella Bella. The mechanism of the upwelling on the BC coasts has always been thought to be the weakened downwelling in summer. This work expands the study of the processes and frequencies that influence upwelling on the BC coast to the quasi-biweekly (QBW) band and equatorial Pacific and northern California regions. This is the first study to present evidence of the remote QBW oscillation influence and the 50 – 130 day period processes on the Vancouver Island

shelf. Upwelling plays a key role on the continental shelf of BC bringing up higher nutrients, lower temperature, and relatively oxygen rich water onto the shelf so that it is available for deep inlet renewal events. These studies should consider both local and remote influences.

Given the complex waterway system and the shelf dynamics, Douglas Channel is by no means an isolated fjord. I look forward to seeing results from this thesis applied to other similar fjords. The long-range connection between the coast of BC and remote regions also impacts regional numerical models where the propagation of coastal trapped waves is required to accurately model sea levels, along-shore velocities, and even cross-shore velocities and water properties. Long-term variability research on BC coast needs to consider both local and remote changes. Connections between CTWs on the BC coast and the El Niño and La Ni na events should be studied to better understand the effects of remote events on the variability on the BC coast. I expect many new studies that will validate and advance this topic.

Appendix A

Supplementary Information for Chapter 2

Introduction

The regression analysis in the paper itself is mostly focused on the time period of 2014-2015. We list the regression results during other time periods here as the supplementary material.

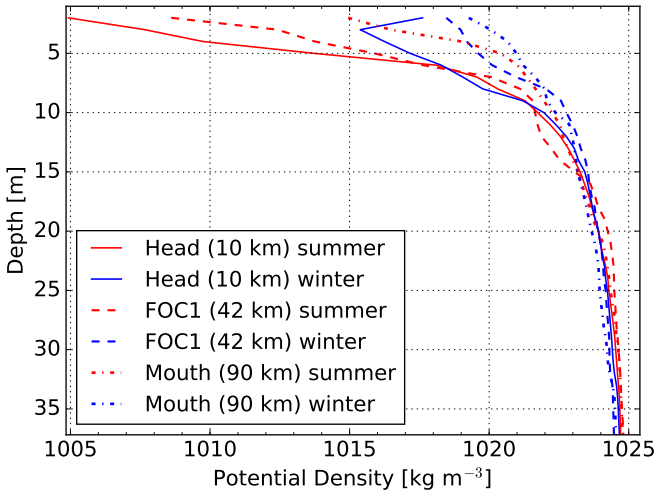

Figure A.1: Top 35 m Potential Density at the head (solid lines), FOC1 (dashed lines) and at the mouth (dash-dotted lines) of Douglas Channel. The summer data is the average of the July 2013 and July 2014 cruise CTDs, and the winter data is the average of April 2014 and October 2014 cruise CTDs.

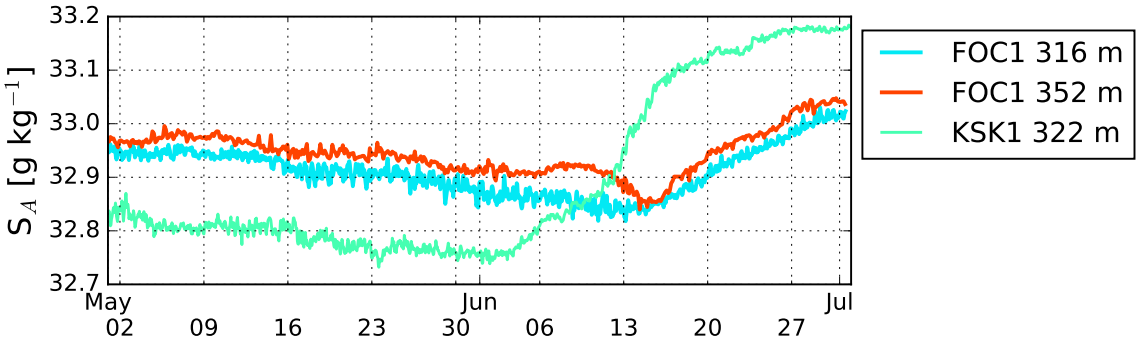

Figure A.2: Absolute Salinity (raw) at the bottom of the three stations during the renewal in 2014.

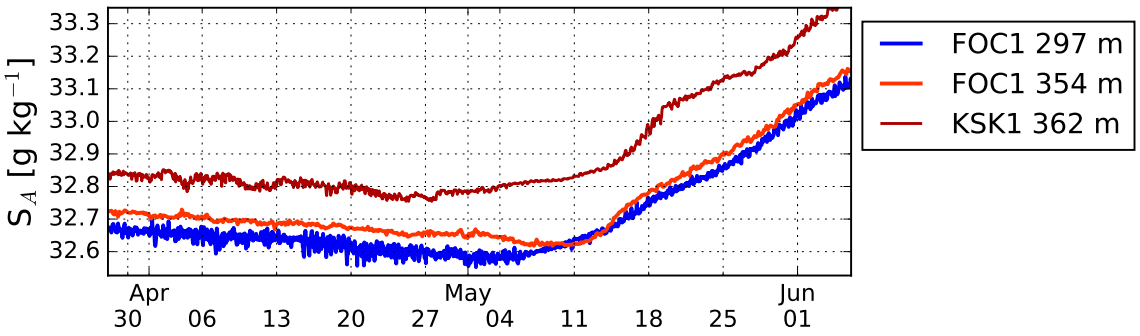

Figure A.3: Absolute Salinity (raw) at the bottom of the three stations during the renewal in 2015. Note that there is an interannual variability between 2014 and 2015 renewal events.

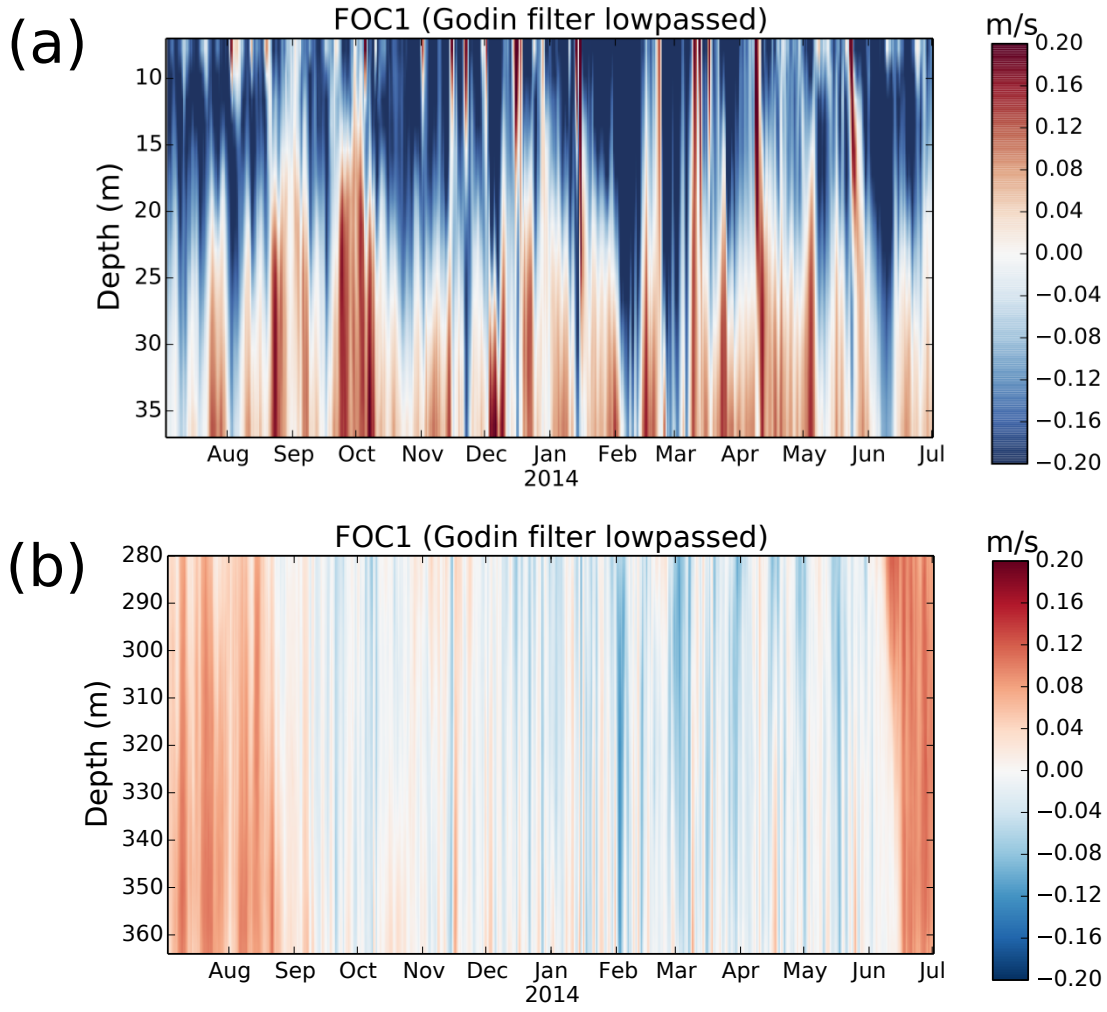

Figure A.4: ADCP profiles at FOC1 2013–2014.

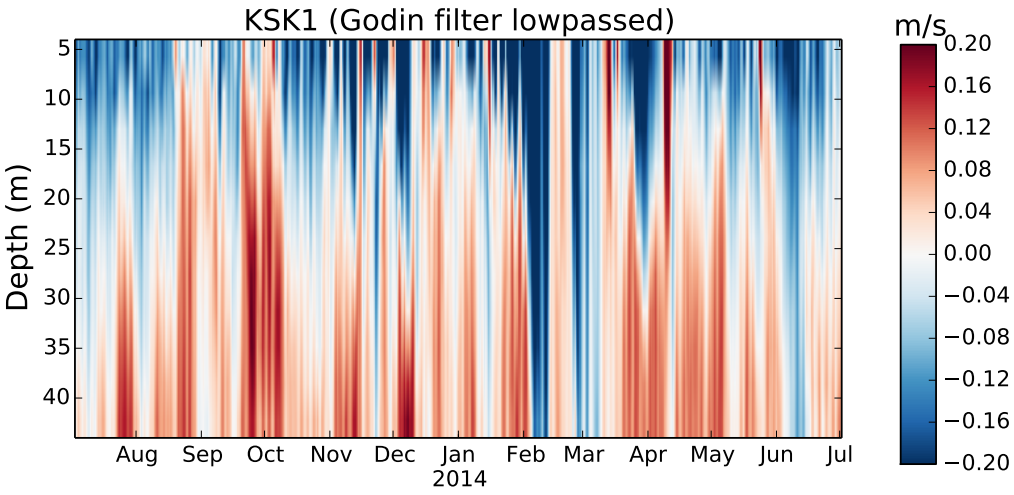

Figure A.5: ADCP profiles at KSK1 2013–2014.

Table A.1: Wind and current velocity correlations. u_F denotes the current velocity at FOC1, and u_K denotes the current velocity at KSK1. Both the wind velocities and the current velocities are Godin low-passed, and the effective degrees of freedom (N_e) is calculated by $N/67$, where the energy amplitude drops to half at T = 67 h for the Godin filter. The peak correlations occur when the surface current velocity term lags the wind velocity term by the hours listed in the 'lag' column. Using the wind velocity (x) as the predictor variable, a linear regression model can be set up as $y \sim mx + b$, where y is the surface current velocity. The root-mean-square deviation (rmsd) is used to measure the difference between the estimated and the observed current velocities. All uncertainties are calculated at the 95% significance level.

Time Period	$y \sim mx + b$	N	N_e	$r \pm \Delta r$	$(m \pm \Delta m) \times 100$	$b \pm \Delta b$	lag [h]	rms_y [m s^{-1}]	rmsd [m s^{-1}]
2013-07-03 to 2014-02-12	u_F@5.0 m	5370	80	0.87 ± 0.05	3.7 ± 0.0	-0.14 ± 0.02	5 ± 11	0.24	0.10
2014-05-30 to 2014-07-01	u_F@5.0 m	754	11	0.53 ± 0.33	2.3 ± 1.6	-0.16 ± 0.08	5 ± 11	0.12	0.08
2014-07-04 to 2014-12-16	u_F@5.2 m	3979	59	0.80 ± 0.08	2.5 ± 0.0	-0.13 ± 0.02	5 ± 20	0.21	0.09
2015-01-13 to 2015-07-25	u_F@5.2 m	4624	69	0.79 ± 0.08	2.7 ± 0.0	-0.14 ± 0.02	5 ± 20	0.18	0.09
2013-07-03 to 2014-02-12	u_K@4.0 m	5370	80	0.66 ± 0.11	2.2 ± 0.0	-0.13 ± 0.03	4 ± 20	0.20	0.11
2014-05-30 to 2014-07-01	u_K@4.0 m	754	11	< 0.1					
2014-07-04 to 2014-12-16	u_K@4.8 m	3979	59	0.74 ± 0.10	2.5 ± 0.0	-0.14 ± 0.02	5 ± 20	0.23	0.11
2015-01-13 to 2015-07-25	u_K@4.8 m	4624	69	0.71 ± 0.10	2.7 ± 0.0	-0.16 ± 0.03	4 ± 16	0.21	0.11

Table A.2: Regression results between the wind stress and the barotropic pressure gradients derived from $\tilde{\tau}_w = h_1\rho_1 g\frac{\partial\tilde{\eta}_1}{\partial x}$ and $h_1\rho_1 g\frac{\partial\overline{\eta}_1}{\partial x} - \overline{\tau}_w + \overline{\tau}_{h_1} = 0$. So $\overline{\tau}_{h_1}$ can be estimated from the intercept (b) of the regression fit: $\overline{\tau}_{h_1} = \overline{\tau}_w - h_1\rho_1 g\frac{\partial\overline{\eta}_1}{\partial x}$. r is the correlation coefficient between the wind stress anomaly $\tilde{\tau}_w$ and the barotropic pressure gradient anomaly $\rho_1 g\frac{\partial\tilde{\eta}_1}{\partial x}$. The peak correlations occur when the surface elevation gradient anomaly term lags the wind stress term by the hours listed in the 'lag' column. All uncertainties are calculated at the 95% significance level.

Time Period	N	N_e	$h_1 \pm \Delta h_1$	$r \pm \Delta r$	lag (h)	$h_1\rho_1 g\frac{\partial\overline{\eta}_1}{\partial x}$	$\overline{\tau}_w$	$\overline{\tau}_{h_1}$
2013-07-03 to 2014-02-12	5370	80	10.0 ± 1.7	0.85 ± 0.05	6 ± 16	0.064	-0.007	-0.057
2014-05-30 to 2014-12-16	3502	52	11.8 ± 1.7	0.88 ± 0.05	6 ± 17	-0.066	-0.008	0.058
2015-01-13 to 2015-07-25	4624	69	8.0 ± 1.1	0.86 ± 0.05	5 ± 9	-0.010	0.005	-0.005

Table A.3: Correlations between the wind velocity and the surface potential density anomalies. The potential density anomalies are calculated from the surface observations obtained at FOC1 and KSK1 (Table 1). In all periods listed here, the density anomalies lag the wind velocity. The peak correlations occur when the density anomaly term lags the wind velocity term by the hours listed in the 'lag' column. All uncertainties are calculated at the 95% significance level.

Time Period	N	N_e	y (F-K)	x	$r \pm \Delta r$	lag (h)
2013-07-03 to 2014-02-12	5350	80	$\Delta\sigma_\theta$	wind	0.73 ± 0.09	20 ± 23
2014-07-03 to 2014-12-16	3978	59	$\Delta\sigma_\theta$	wind	0.70 ± 0.11	20 ± 40
2015-01-13 to 2015-07-25	4624	69	$\Delta\sigma_\theta$	wind	0.67 ± 0.11	16 ± 20

Table A.4: Regression results between the barotropic and baroclinic pressure gradients. The barotropic pressure gradient is the surface pressure gradient anomalies ($\frac{\partial \tilde{\eta}_1}{\partial x}$) between Stations Kitimat and Hartley Bay (Figure 1). The baroclinic pressure gradient is calculated from the surface potential density anomalies ($-\frac{g}{\rho_0}\frac{\partial \tilde{\sigma}_\theta}{\partial x}$) between FOC1 and KSK1 (Figure 1). As explained in Section 4.3, the slope estimation h_1 is the averaged balancing depth where barotropic and baroclinic pressure gradients balance each other. The peak correlations occur when the baroclinic term lags the barotropic term by the hours listed in the 'lag' column. All uncertainties are calculated at the 95% significance level.

Time Period	N	N_e	σ_θ dep [m] at FOC1	σ_θ dep [m] at KSK1	$r \pm \Delta r$	lag (h)	$h_1 \pm \Delta h_1$
2013-07-20 to 2014-05-28	7487	112	16	19	0.75 ± 0.07	11 ± 17	44 ± 7
2014-07-24 to 2015-07-25	8790	131	12	15	0.73 ± 0.07	10 ± 18	34 ± 6

Appendix B

Supplementary Information for Chapter 3

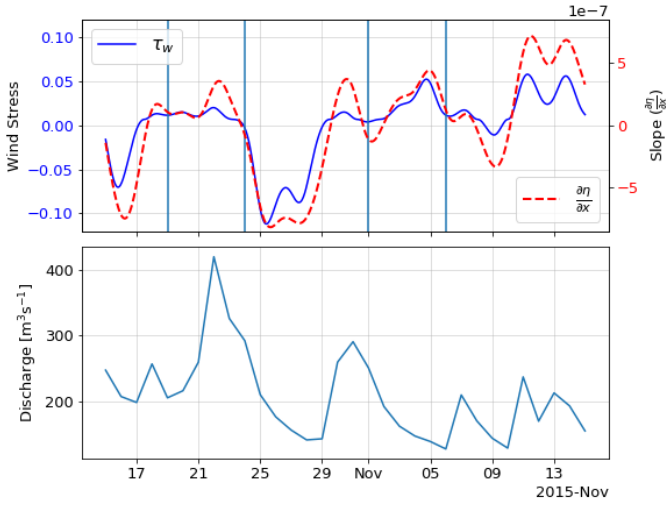

Figure B.1: Upper: The lowpassed along-channel surface slope anomalies and the wind stress between Oct 15 to Nov 15, 2015. The vertical blue lines represent the time when the CTD profiles were taken. Lower: Daily Kitimat River discharge.

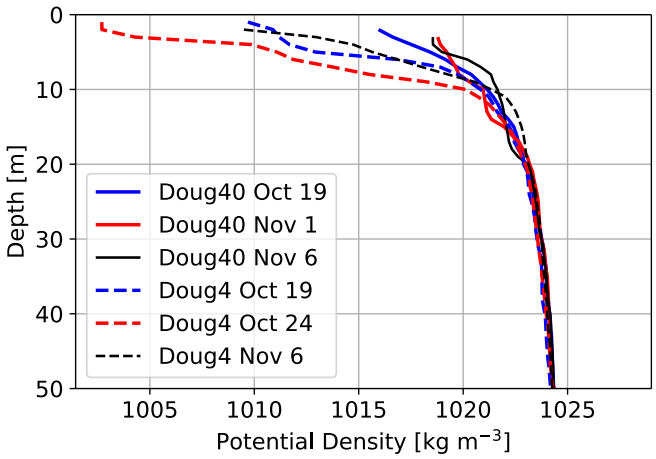

Figure B.2: Potential density profiles at Station Doug4 and Doug40 during 2015-54 in the top 50 m. The solid profiles are from Doug 40, where it is close to Hartley Bay. The dashed lines are from Doug 4, which is close to the head of the channel.

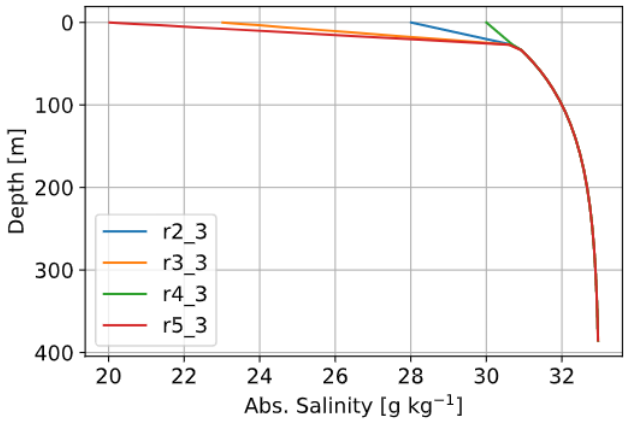

Figure B.3: Initial salinity in four stratified runs.

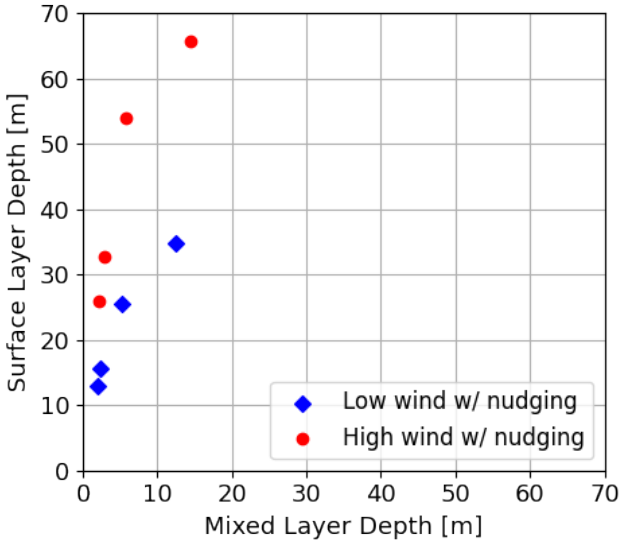

Figure B.4: Mixed layer depth versus the first layer thickness. The mixed layer depth is defined as the depth where the density is 0.125 kg/m^3 larger than the surface density.

Bibliography

Anup, N., Vijith, V., Jithin, A. K., Rohith, B., Amol, P., and Francis, P. A. (2021). Quasi-biweekly oscillation in sea level along the western Bay of Bengal. *Continental Shelf Research*, 231(October):104594.

Arneborg, L. and Erlandsson, C. (2004). The rate of inflow and mixing during deep-water renewal in a sill fjord. *Limnology and Oceanography*, 49(3):768–777.

Aydln, M. and Beşiktepe, S. T. (2022). Mechanism of generation and propagation characteristics of coastal trapped waves in the Black Sea. *Ocean Science*, 18(4):1081–1091.

Baker, P. D. and Pond, S. (1995). The low-frequency residual circulation in Knight Inlet, British Columbia. *Journal of Physical Oceanography*, 25:747–763.

Bakun, A. (1973). Coastal Upwelling Indices, West Coast of North America, 1946-71. NOAA Technical Report NMF SSRF-671. Technical report, NOAA.

Bakun, A. (1975). Daily and Weekly Upwelling Indices, West Coast of North America, 1967-1973. *NOAA Technical Reports*, (August):124.

Battisti, D. S. and Hickey, B. M. (1984). Application of Remote Wind-Forced Coastal Trapped Wave Theory to the Oregon and Washington Coasts.

Benjamin, T. B. (1968). Gravity currents and related phenomena. *Journal of Fluid Mechanics*, 31:209–248.

Boening, C., Willis, J. K., Landerer, F. W., Nerem, R. S., and Fasullo, J. (2012). The 2011 la Nia: So strong, the oceans fell. *Geophysical Research Letters*, 39(19):1–5.

Bretschneider, D., Cannon, G., Holbrook, J., and Pashinski, D. (1985). Variability of Subtidal Current Structure in a Fjord Estuary: Puget Sound, Washington. *Journal of Geophysical Research*, 90(5):1949–1958.

Brink, K. H. (1991). Coastal-Trapped Waves and wind-driven currents over the continental shelf. *Annual Review of Fluid Mechanics*, 23:389–412.

Brink, K. H., Bane, J., Church, T., Fairall, C., Geemaert, G., Hammond, D., Henrichs, S., Martens, C., Nittrouer, C., Rogers, D., Roman, M., Roughgarden, J., Smith, R., Wright, L., and Yoder, J. (1992). Coastal ocean processes: a science prospectus. Technical report, The Woods Hole Oceanographic Institution, Woods Hole.

Castillo, M. I., Pizarro, O., Cifuentes, U., Ramirez, N., and Djurfeldt, L. (2012). Subtidal dynamics in a deep fjord of southern Chile. *Continental Shelf Research*, 49:73–89.

Connolly, T. P., Hickey, B. M., Shulman, I., and Thomson, R. E. (2014). Coastal Trapped Waves, Alongshore Pressure Gradients, and the California Undercurrent*. *Journal of Physical Oceanography*, 44(1):319–342.

Cravatte, S., Picaut, J., and Eldin, G. (2003). Second and first baroclinic Kelvin modes in the equatorial Pacific at intraseasonal timescales. *Journal of Geophysical Research*, 108:1–20.

Crawford, W. R. (2001). Oceans of the Queen Charlotte Islands. Technical report, Institute of Ocean Sciences, Sidney, BC.

Crawford, W. R. and Dewey, R. K. (1989). Turbulence and mixing: Sources of nutrients on the Vancouver Island continental shelf. *Atmosphere - Ocean*, 27(2):428–442.

Crawford, W. R., Johannessen, D., Whitney, F., Birch, R., Borg, K., Fissel, D., and Vagle, S. (2007). PNCIMA App C: Physical and Chemical Oceanography. Technical report, Institute of Ocean Sciences, Sidney, BC.

Crawford, W. R. and Thomson, R. E. (1984). Diurnal-period continental shelf waves along Vancouver Island: a comparison of observations with theoretical models. *Journal of Physical Oceanography*, 14:1629–1646.

Crawford, W. R. and Thomson, R. E. (1991). Physical oceanography of the western Canadian continental shelf. *Continental Shelf Research*, 11:669–683.

Cummins, P. F., Masson, D., and Foreman, M. G. G. (2000). Stratification and Mean Flow Effects on Diurnal Tidal Currents off Vancouver Island. *Journal of Physical Oceanography*, 30(1):15–30.

Cushman-Roisin, B., Asplin, L., and Svendsen, H. (1994). Upwelling in broad fjords. *Continental Shelf Research*, 14(15):1701–1721.

Davis, K. A., Banas, N. S., Giddings, S. N., Siedlecki, S. A., MacCready, P., Lessard, E. J., Kudela, R. M., and Hickey, B. M. (2014). Estuary-enhanced upwelling of marine nutrients fuels coastal productivity in the U.S. Pacific Northwest. *Journal of Geophysical Research: Oceans*, 119:8778–8799.

de Freitas, P. P., Paiva, A. d. M., Cirano, M., Mill, G. N., da Costa, V. S., Gabioux, M., and França, B. R. L. (2021). Coastal trapped waves propagation along the Southwestern Atlantic Continental Shelf. *Continental Shelf Research*, 226(July):104496.

de Young, B. and Pond, S. (1988). The Deepwater Exchange Cycle in Indian Arm , British Columbia. *Estuarine, Coastal and Shelf Science*, 26:285–308.

Di Lorenzo, E. and Ohman, M. D. (2013). A double-integration hypothesis to explain ocean ecosystem response to climate forcing. *Proceedings of the National Academy of Sciences of the United States of America*, 110(7):2496–2499.

Enfield, D. B. and Allen, J. S. (1980). On the structure of dynamics of monthly mean sea level anomalies along the Pacific Coast of North and South America. *Journal of Physical Oceanography*, 10:557–578.

Enfield, D. B., Cornejo-rodriguez, M. D. E. L. P., Smith, L., and Newberger, P. A. (1987). The equatorial source of propagating variability along the Peru Coast During the 1982-1983 E1 Ni∼no. *Journal of Geophysical Research*, 92(No. C13):14335–14346.

Engida, Z., Monahan, A., Ianson, D., and Thomson, R. E. (2016). Remote forcing of subsurface currents and temperatures near the northern limit of the California Current System. *Journal of Geophysical Research: Oceans*, (121):7244–7262.

Farmer, D. M. (1976). The Influence of Wind on the Surface Layer of a Stratified Inlet: Part II. Analysis.

Farmer, D. M. and Freeland, H. J. (1983). The Physical Oceanography of Fjords. *Progress in Oceanography*, 12:147–220.

Farmer, D. M. and Osborn, T. R. (1976). The Influence of Wind on the Surface Layer of a Stratified Inlet: Part I. Observations. *Journal of Physical Oceanography*, 6(6):932–940.

Farmer, D. M. and Smith, D. J. (1980). Tidal interaction of stratified flow with a sill in Knight Inlet. *Deep-Sea Research*, 27A.

Freeland, H. J. and Farmer, D. M. (1980). Circulation and Energetics of a Deep, Strongly Stratified Inlet. *Can. J. Fish. Aquat. Sci.*, 37:1398–1410.

Gardner, G. A. (1982). Patterns in the distribution and abundance of selected zooplankton species from the coast British Columbia. *Biological Oceanography*, 1(3):255–270.

Geyer, W. R. (1997). Influence of Wind on Dynamics and Flushing of Shallow Estuaries. *Estuarine, Coastal and Shelf Science*, 44(6):713–722.

Geyer, W. R. and Cannon, G. A. (1982). Sill processes related to deep water renewal in a fjord. *Journal of Geophysical Research*, 87(C10):7985–7996.

Gill, A. E. (1982). *Atmosphere-Ocean Dynamics*. Academic Press, Inc., New York.

Godin, G. (1972). *The Analysis of Tides*. University of Toronto Press, Toronto.

Government of British Columbia (2016). Great bear rainforest (forest management) act.

Haidvogel, D. B., Arango, H., Budgell, W. P., Cornuelle, B. D., Curchitser, E., Di Lorenzo, E., Fennel, K., Geyer, W. R., Hermann, A. J., Lanerolle, L., Levin, J., McWilliams, J. C., Miller, A. J., Moore, A. M., Powell, T. M., Shchepetkin, A. F., Sherwood, C. R., Signell, R. P., Warner, J. C., and Wilkin, J. (2008). Ocean forecasting in terrain-following coordinates: Formulation and skill assessment of the Regional Ocean Modeling System. *Journal of Computational Physics*, 227(7):3595–3624.

Haidvogel, D. B., Arango, H. G., Hedstrom, K., Beckmann, A., Malanotte-Rizzoli, P., and Shchepetkin, A. F. (2000). Model evaluation experiments in the North

Atlantic Basin: Simulations in nonlinear terrain-following coordinates. *Dynamics of Atmospheres and Oceans*, 32(3-4):239–281.

Halliwell, G. R. and Allen, J. (1984). Large-Scale Sea Level Response to Atmospheric Forcing along the West Coast of North America, Summer 1973. *Journal of Physical Oceanography*, 14:864–886.

Halverson, M. J., Bélanger, C., and Gay, S. M. (2013). Seasonal transport variations in the straits connecting Prince William Sound to the Gulf of Alaska. *Continental Shelf Research*, 63:63–78.

Hansen, D. V. and Rattray, M. (1966). New dimensions in estuary classification. *Limnology and Oceanography*, XI(July):319–326.

Hickey, B. M. and Banas, N. S. (2008). Why is the northern end of the California Current System so productive? *Oceanography*, 21(SPL.ISS. 4):90–107.

Hickey, B. M., Geier, S., Kachel, N., Ramp, S., Kosro, P., and Connolly, T. P. (2016). Alongcoast structure and interannual variability of seasonal midshelf water properties and velocity in the Northern California Current System. *Journal of Geophysical Research: Oceans*, pages 7408–7430.

Inall, M. E., Nilsen, F., Cottier, F. R., and Daae, R. (2015). Shelf/fjord exchange driven by coastal-trapped waves in the Arctic. *Journal of Geophysical Research: Oceans*, 120(12):8283–8303.

Jackson, J. M., Bianucci, L., Hannah, C. G., Carmack, E. C., and Barrette, J. (2021). Deep Waters in British Columbia Mainland Fjords Show Rapid Warming and Deoxygenation From 1951 to 2020. *Geophysical Research Letters*, 48(3):1–9.

Janzen, C. D., Simpson, J. H., Inall, M. E., and Cottier, F. (2005). Across-sill circulation near a tidal mixing front in a broad fjord. *Continental Shelf Research*, 25(15):1805–1824.

Keshavamurty, R. N. (1972). On the vertical tilt of Monsoon disturbances. *Journal of the atmospheric sciences*, (July):993–995.

Kikuchi, K. and Wang, B. (2009). Global perspective of the quasi-biweekly oscillation. *Journal of Climate*, 22(6):1340–1359.

Klinck, J. M., O'Brien, J. J., and Svendsen, H. (1981). A Simple Model of Fjord and Coastal Circulation Interaction. *Journal of Physical Oceanography*, 11(12):1612–1626.

Knudsen, M. (1900). Ein hydrographischer Lehrsatz. *Annualen der Hydrographie und maritimen Meteorologie*, 28(7):316–320.

Kundu, P. K. and Cohen, I. M. (2008). *Fluid Mechanics*. Academic Press, Amsterdam, 4 edition.

Large, W. G. and Pond, S. (1981). Open Ocean Momentum Flux Measurements in Moderate to Strong Winds.

LeBlond, P. H., Ma, H., Doherty, F., and Pond, S. (1991). Deep and intermediate water replacement in the Strait of Georgia. *Atmosphere-Ocean*, 29(2):288–312.

Macdonald, R. (1983). Proceedings of a workshop on the Kitimat Marine Environment. In Macdonald, R., editor, *Technical Report of Hydrography and Ocean Sciences No. 18*, number 18, pages 1–218, Sidney, BC. Institute of Ocean Sciences, Patricia Bay; Canada. Dept. of Fisheries and Oceans.

Macdonald, R., Cretney, W. J., and Wong, C. S. (1983). Chemical characteristics of water in the Kitimat fjord system. In Macdonald, R., editor, *Proceedings of a workshop on the Kitimat Marine Environment Canadian No. 18*, pages 67–88, Sidney, BC. Can. Tech. Rep. Hydrogr. Ocean Sci.

MacKas, A. L., Denman, K. L., and Bennett, A. F. (1987). Least squares multiple tracer analysis of water mass composition. *Journal of Geophysical Research: Oceans*, 92(C3):2907–2918.

Masson, D. (2002). Deep Water Renewal in the Strait of Georgia. *Estuarine, Coastal and Shelf Science*, 54(1):115–126.

Masson, D. and Cummins, P. F. (2007). Temperature trends and interannual variability in the Strait of Georgia, British Columbia. *Continental Shelf Research*, 27(5):634–649.

Masson, D. and Fine, I. (2012). Modeling seasonal to interannual ocean variability of coastal British Columbia. *Journal of Geophysical Research*, 117(C10):1–14.

Matsuura, H. and Cannon, G. A. (1997). Wind effects on sub-tidal currents in Puget Sound. *Journal of Oceanography*, 53(1):53–66.

Miyama, T., McCreary, J. P., Sengupta, D., and Senan, R. (2006). Dynamics of biweekly oscillations in the equatorial Indian Ocean. *Journal of Physical Oceanography*, 36(5):827–846.

Moore, D. W. (1968). *Planetary-gravity Waves in an Equatorial Ocean*. PhD thesis, Harvard University.

Morrison, J., Foreman, M. G. G., and Masson, D. (2012). A Method for Estimating Monthly Freshwater Discharge Affecting British Columbia Coastal Waters. *Atmosphere-Ocean*, 50(1):1–8.

Mosquera-Vasquez, K., Dewitte, B., and Illig, S. (2014). The central Pacific El Ni∼no intraseasonal Kelvin wave. *Journal of Geophysical Research : Oceans*, pages 6605–6621.

Myksvoll, M. S., Sandvik, A. D., Skardhamar, J., and Sundby, S. (2012). Importance of high resolution wind forcing on eddy activity and particle dispersion in a Norwegian fjord. *Estuarine, Coastal and Shelf Science*, 113:293–304.

Mysak, L. A. (1980). Topographicall trapped waves. *Annual Review of Fluid Mechanics*, (12):45–76.

Pawlowicz, R. (2017). Seasonal Cycles, Hypoxia, and Renewal in a Coastal Fjord (Barkley Sound, British Columbia). *Atmosphere-Ocean*, 0(0):1–20.

Pedlosky, J. (1987). *Geophysical Fluid Dynamics*. Springer-Verlag, New York, 2nd edition.

Peña, M. A., Fine, I., and Callendar, W. (2019). Interannual variability in primary production and shelf-offshore transport of nutrients along the northeast Pacific Ocean margin. *Deep-Sea Research Part II: Topical Studies in Oceanography*, 169-170(January):104637.

Pickard, G. (1961). Oceanographic Features of Inlets in the British Columbia Mainland Coast. *J. Fish. Res. Bd. Canada*, 18(6):907–999.

Pickard, G. L. (1963). Oceanographic Characteristics of Inlets of Vancouver Island, British Columbia. *J. Fish. Res. Bd. Canada*, 20(5):1109–1144.

Pietri, A., Echevin, V., Testor, P., Chaigneau, A., Mortier, L., Grados, C., and Albert, A. (2014). Impact of a coastal-trapped wave on the near-coastal circulation of the Peru upwelling system from glider data. *Journal of Geophysical Research: Oceans*, (May):2109–2120.

Pringle, J. M. and Riser, K. (2003). Remotely forced nearshore upwelling in Southern California. *Journal of Geophysical Research: Oceans*, 108(4):1–11.

Saarikoski, H., Raitio, K., and Barry, J. (2013). Understanding successfulconflict resolution: Policy regime changes and new interactive arenas in the Great Bear Rainforest. *Land Use Policy*, 32:271–280.

Shan, S., Hannah, C. G., and Wu, Y. (2019). Coupling of Estuarine Circulations in a Network of Fjords. *Journal of Geophysical Research: Oceans*, 124(10):6809–6830.

Shchepetkin, A. F. and McWilliams, J. C. (2005). The regional oceanic modeling system (ROMS): A split-explicit, free-surface, topography-following-coordinate oceanic model. *Ocean Modelling*, 9(4):347–404.

Shchepetkin, A. F. and McWilliams, J. C. (2009). Correction and commentary for "Ocean forecasting in terrain-following coordinates: Formulation and skill assessment of the regional ocean modeling system" by Haidvogel et al., J. Comp. Phys. 227, pp. 3595-3624. *Journal of Computational Physics*, 228(24):8985–9000.

Spall, M. A., Jackson, R. H., and Straneo, F. (2017). Journal of Geophysical Research : Oceans Katabatic Wind-Driven Exchange in Fjords. *Journal of Geophysical Research : Oceans*, 122:8246–8262.

Stigebrandt, A. (1981). A mechanism governing the estuarine circulation in deep, strongly stratified fjords. *Estuarine, Coastal and Shelf Science*, 13(2):197–211.

Stigebrandt, A. (2012). Hydrodynamics and circulation of fjords. In Lars Bengtsson, Reginald W. Herschy, R. W. F., editor, *Encyclopedia of Lakes and Reservoirs*, number c, pages 327–344. Springer.

Syvitski, J. P., Burrell, D. C., and Skei, J. M. (1987). *Fjords: processes and products*. Springer-Verlag, New York, 1 edition.

Thomson, R. E. (1981). *Oceanography of the British Columbia Coast*. Can. Spec. Publ. Fish. Aquat. Sci. 56, Ottawa.

Thomson, R. E. and Davis, E. E. (2017). Equatorial Kelvin waves generated in the western tropical Pacific Ocean trigger mass and heat transport within the Middle America Trench off Coasta Rica. *Journal of Geophysical Research: Oceans*, 122(5423):1–22.

Thomson, R. E. and Emery, W. J. (2014). *Data analysis methods in physical oceanography*. Newnes, 3 edition.

Thomson, R. E. and Fine, I. (2021). Revisiting the Ocean' s Nonisostatic Response to 5-Day Atmospheric Loading: New Results Based on Global Bottom Pressure Records and Numerical Modeling. *Journal of Physical Oceanography*, 51(1982):2845–2859.

Thomson, R. E., Hickey, B. M., and LeBlond, P. H. (1986). Water property observations from the Vancouver Island Coastal Current experiment: June, July and October, 1984. Technical Report 46, Institute of Ocean Sciences, Sidney, BC.

Thomson, R. E. and Krassovski, M. V. (2010). Poleward reach of the California Undercurrent extension. *Journal of Geophysical Research: Oceans*, 115(9):1–9.

Thomson, R. E. and Krassovski, M. V. (2015). Remote alongshore winds drive variability of the California Undercurrent off the British Columbia-Washington coast. *Journal of Geophysical Research: Oceans*, 120:8151–8176.

Thomson, R. E., Mihály, S. F., and Kulikov, E. a. (2007). Estuarine versus transient flow regimes in Juan de Fuca Strait. *Journal of Geophysical Research: Oceans*, 112(9):1–25.

Thomson, R. E., Spear, D. J., Krassovski, M. V., Hourston, R. A., Juhász, T. A., and Mihaly, S. F. (2017). Buoyancy-driven coastal currents blocks ventilation of an anoxic fjord on the Pacific coast of Canada. *Journal of Geophysical Research: Oceans*, 122(5423):1–22.

Thomson, R. E. and Ware, D. M. (1996). A Current Velocity Index of Ocean Variability. *Journal of Geophysical Research*, 101:14297–14310.

Valle-Levinson, A., Sarkar, N., Sanay, R., Soto, D., and León, J. (2007). Spatial structure of hydrography and flow in a Chilean fjord, Estuario Reloncav. *Estuaries and coasts*, 30(1):113–126.

Vangriesheim, A., Treguier, A. M., and Andre, G. (2005). Biweekly current oscillations on the continental slope of the Gulf of Guinea. *Deep-Sea Research Part I: Oceanographic Research Papers*, 52(11):2168–2183.

Wan, D., Hannah, C. G., Cummins, P. F., Foreman, M. G., and Dosso, S. E. (2022). Wind-Driven Currents in a "Wide" Narrow Channel, With Application to Douglas Channel, BC. *Journal of Geophysical Research: Oceans*, 127(8).

Wan, D., Hannah, C. G., Foreman, M. G. G., and Dosso, S. (2017). Sub-tidal circulation in a deep-silled fjord: Douglas Channel, British Columbia. *Journal of Geophysical Research: Oceans*, 122:1–17.

Wang, D.-P. and Mooers, C. N. K. (1976). coastal-trapped waves in a continuously stratified ocean. *Journal of Physical Oceanography*, 6:853–863.

Ware, D. M. and Thomson, R. E. (2005). Bottom-Up Ecosystem Trophic Dynamics Determine Fish Production in the Northeast Pacific. *Science*, 308(May):1280.

Warner, J. C., Geyer, W. R., and Lerczak, J. A. (2005a). Numerical modeling of an estuary: A comprehensive skill assessment. *Journal of Geophysical Research C: Oceans*, 110(5):1–13.

Warner, J. C., Sherwood, C. R., Arango, H. G., and Signell, R. P. (2005b). Performance of four turbulence closure models implemented using a generic length scale method. *Ocean Modelling*, 8(1-2):81–113.

Weber, J. E. (1983). Steady wind-and wave-induced currents in the open ocean. *J. Phys. Oceanogr.*, 13:524–530.

Webster, I. (1980a). Kitimat Physical Oceanographic Study 1977-1978 Part 1: Data Collection and Analyses. Technical report, Institute of Ocean Sciences, Sidney, BC.

Webster, I. (1980b). Kitimat Physical Oceanographic Study 1977-1978 Part 3: Estuarine Circulation. Technical report, Institute of Ocean Sciences, Sidney, BC.

Wright, C., Vagle, S., Hannah, C. G., and Johannessen, S. (2015). Physical , Chemical and Biological Oceanographic Data Collected in Douglas Channel and the Approaches to Kitimat, June 2013-July 2014. Technical Report July 2014, Institute of Ocean Sciences, Sidney, BC; Can. Data. Report. Hydrog. Ocean.Sci. 196.

Wright, C., Vagle, S., Hannah, C. G., Johannessen, S., Spear, D. J., and Wan, D. (2016). Physical, chemical and biological oceanographic data collected in Douglas Channel and the approaches to Kitimat, October 2014-July 2015. Technical report, Institute of Ocean Sciences, Sidney, BC; Can. Data. Report. Hydrog. Ocean.Sci. 200.

Young, C., McAllister, I., and McAllister, K. (1997). *The great bear rainforest: Canada's forgotten coast.* Madeira Park, BC: Harbour Pub.